UNIVERSITÀ DEGLI STUDI DI PADOVA

Dipartimento di Fisica e Astronomia "Galileo Galilei"

Corso di Laurea Magistrale in Fisica

Tesi di Laurea

Primordial power spectrum constraints from astrophysical observations

Relatore

Prof. Alvise Raccanelli

Correlatore

Prof. Sabino Matarrese

Laureando

Alessandro Rubin

Mat. 1114302

Anno Accademico 2021/2022

Abstract: This thesis will investigate constraints on the primordial power spectrum coming from a variety of current and future astrophysical experiments. In particular, we will focus on the limits that can be obtained on the running parameters of the primordial power spectrum from 21 cm Intensity Mapping experiments targeted towards the Dark Ages. We will also investigate the possibility of Primordial Black Holes formation from curvature perturbations in the early Universe and determine whether Intensity Mapping experiments will be able to detect the departure from scale invariance that lead to their formation.

Contents

Chapter 1

Introduction

In the last decades we witnessed astounding progress in the field of cosmology. The Planck mission measurements of the Cosmic Microwave Background (CMB) radiation [1] has given us incredibly tight constraints on parameters of the ΛCDM cosmological model, while galaxy surveys are increasing their precision and volume probed, giving us information in the low redshift range.

On top of that, gravitational wave astronomy opened up a new way to see the cosmos, allowing us to cross correlate completely different kind of signals.

A large portion of the Universe remains however unexplored, as no observations have been made between recombination at redshift 1100 and galaxy surveys that probe redshifts of $\mathcal{O}(1)$. This is going to change with the advent of Intensity Mapping (IM) experiments, that will be able to probe that enormous wealth of information, greatly enriching our understanding in cosmology.

IM is a novel technique aimed at mapping the intensity in emission of the redshifted spectral lines produced by atomic and molecular species in galaxies and in the intergalactic medium. With the angular information and the measured redshifted frequency of the spectral line is then possible to model the 3-dimensional distribution of the source emitting it.

Unlike galaxy surveys, which can target only objects above a certain flux threshold, IM experiments collect the integrated emission of unresolved sources, and is therefore sensitive to all sources of emission, even the faintest, as shown in fig 1.1.

Perhaps the most intriguing application of IM is the mapping of the 21 cm spectral line emitted in the hyperfine transition of spectral hydrogen. This atomic element has been present throughout

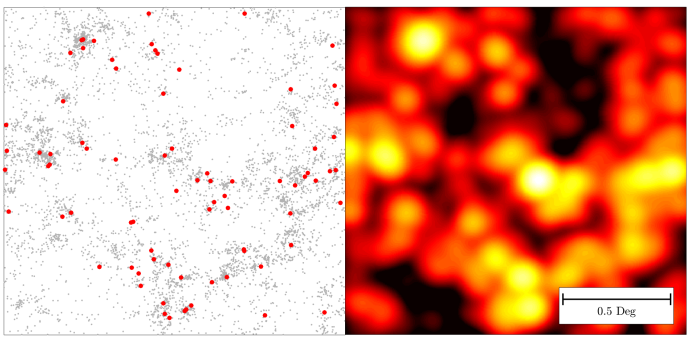

Figure 1.1: A simulated 2.5 deg^2 field with galaxy positions (*Left*) and the corresponding CO intensity map (*Right*). Luminosities were drawn from a Schechter function model (Breysse et al. 2016). Sources bright enough to detect with 1hr of VLA time are marked in red (see Li et al. 2016). (*Figure: Patrick Breysse*). Taken from [2]

most of the history of the Universe and it's theoretically possible to trace its spectral emission from $z \sim 200$ until $z \sim 6$, when virtually all the hydrogen has been reionized by bright sources.

21 cm IM will allow us to peek for the first time at those vast cosmological regions, and to map the density fluctuations in the hydrogen density field at higher redshift $30 \lesssim z \lesssim 200$, before stars ionized the neutral hydrogen. This has the potential to enormously increase our cosmological understanding, providing us information regarding many different observables, such as ΛCDM parameters [3], primordial non gaussianity [4], statistical isotropy violations [5], dark matter annihilation [6], the origin of super massive black holes [7] and more.

At smaller redshift, instead, it will be possible to study for the first time the formation of the first stars and galaxies by measuring the dark patches in the 21 cm emission caused by the ionization of hydrogen.

We will therefore focus our work in particular on the 21 cm spectral line, but we note that many other spectral lines are available, albeit they are restricted to smaller z, such as the rotational CO lines, the Lyman-α, the [CII] fine structure line. For a comprehensive review on those spectral lines and the experiments in the works in order to map them see for example [2].

In this thesis we will explore how the rapidly growing field of IM will be able to provide constraints on cosmological observables, especially with regards to the physics of the primordial Universe, and which models we will be able to discriminate with the upcoming 21 cm IM experiments, ranging from the soon to be completed SKAO[1] to a more futuristic proposed radio array on the far side of the Moon.

We will first review some introductory cosmological topics in order to set the playing field, and the physics of the early Universe that produced the promordial perturbations. Then we will treat the physics of the 21cm hydrogen line, how the primordial perturbations would affect it and which observables can be studied from it. Finally we will introduce the experimental apparatus in order to observe those perturbations.

With all this information we will then be able to forecast the ability of future experiments to constrain early Universe models.

[1] `https://www.skaobservatory.org/`

Chapter 2

Introductory cosmology topics

In this chapter we will review some basic topics in modern cosmology, introducing the basics and notation used throughout this work.

2.1 Cosmological principle and background metric

At the basis of cosmology lies the cosmological principle, stating that while on small scale it exhibit clumpyness, with matter clumped into stars, galaxies and clusters, on large scales[1] the Universe is in first approximation homogeneous and isotropic. This means that it can be treated like a fluid that evolves according only to the spatially averaged quantities that describe it.

This principle finds its experimental validation in observations such as the Large Scale Structures (LSS) studies and Cosmic Microwave Background probes, the latter measuring anisotropy in temperature $\delta T/T$ only as big as $\sim 10^{-5}$.

The geometric properties of the Universe are described in General Relativity by the metric, a symmetric rank 2 tensor thus having in principle 10 degrees of freedom

$$ds^2 = g_{\mu\nu} dx^\mu dx^\nu. \tag{2.1}$$

The symmetries enforced by the cosmological principle restrict the degrees of freedom of the spacetime metric, therefore it can be shown that the most general form it can take is given by the Friedmann-Robertson-Walker metric:

$$ds^2 = c^2 dt^2 - a(t)^2 \left[\frac{dr^2}{1 - kr^2} + r^2 d\Omega^2 \right] \tag{2.2}$$

with $a(t)$, the scale factor, describing the "size" of the Universe as a function of the cosmological time and k encoding the spatial curvature of the Universe. While k can in principle take any real value, with a coordinate rescaling all values of k can be mapped to the set $\{-1, 0, 1\}$, meaning respectively an open, flat, and closed Universe.

It's important to point out that the spatial coordinates in equation (2.2) are not the physical coordinates, but are comoving coordinates, meaning that they expand with the Universe. This means that two points that are a fixed comoving distance will get recede from each other. With this in mind, recovering the relation between physical and comoving distances is easy

$$d_{\text{phys}} = a(t) d_{\text{comoving}} \tag{2.3}$$

[1] that is about hundreds of megaparsecs (Mpcs)

Another useful way to write equation (2.2) is by introducing the conformal time τ defined as

$$d\tau \equiv \frac{dt}{a(t)} \quad \Rightarrow \quad ds^2 = a(\tau)^2 \left[c^2 d\tau^2 - \left(\frac{dr^2}{1-kr^2} + r^2 d\Omega^2 \right) \right]$$

this way the the metric factorizes in a Minkowski metric multiplied by the scale factor.

2.2 Friedmann equations

The dynamical evolution of the Universe is determined by applying the least action principle on the general relativistic Einstein-Hilbert action

$$\mathcal{S} = \mathcal{S}_{HE} + \mathcal{S}_m = \int \mathrm{d}^4\mathrm{x}\sqrt{-g} \left[\frac{R}{16\pi G} + \mathcal{L}_m \right]. \tag{2.4}$$

$\mathcal{S}_m$ denotes the action of the "matter" content of the Universe. The variational principle demands $\frac{\delta \mathcal{S}}{\delta g^{\mu\nu}} = 0$, leading to

$$\frac{\delta R}{\delta g^{\mu\nu}} + \frac{R}{\sqrt{-g}} \frac{\delta \sqrt{-g}}{\delta g^{\mu\nu}} = -16\pi G \frac{1}{\sqrt{-g}} \frac{\delta(\sqrt{-g}\mathcal{L}_m)}{\delta g^{\mu\nu}} \tag{2.5}$$

By computing the functional derivatives with respect to the inverse metric $g^{\mu\nu}$ we obtain the Einstein field equations

$$R_{\mu\nu} - \frac{1}{2} g_{\mu\nu} R = 8\pi G T_{\mu\nu} \tag{2.6}$$

where G is the gravitational constant, $R_{\mu\nu}$ is the Ricci tensor, a function of the second order derivatives of the metric representing the curvature of the spacetime manifold, and R its contraction, the Ricci scalar. The stress energy tensor $T^{\mu\nu}$ instead encodes the matter-energy content of the Universe and is defined as

$$T_{\mu\nu} \equiv -\frac{2}{\sqrt{-g}} \frac{\delta \left(\sqrt{-g}\mathcal{L}_m\right)}{\delta g^{\mu\nu}}. \tag{2.7}$$

Now we can find a very simple solution of the field equations, that is, the solution in a maximally symmetric spacetime characterized by the metric (2.2). By plugging the FRW metric from equation (2.2) into the field equations and assuming that the matter content of the Universe can be described as a perfect fluid with stress energy tensor

$$T_{\mu\nu} = (p + \rho) u_\mu u_\nu + p g_{\mu\nu}, \tag{2.8}$$

where ρ represents the matter-energy density of the fluit and p its pressure, we obtain the Friedmann equations

$$H^2 = \left(\frac{\dot{a}}{a} \right)^2 = \frac{8}{3}\pi G\rho - \frac{kc^2}{a^2} \tag{2.9}$$

$$\frac{\ddot{a}}{a} = -\frac{4}{3}\pi G \left(\rho + \frac{3p}{c^2} \right) \tag{2.10}$$

describing the background dynamics of our Universe encoded in the time evolution of the scale factor, where we defined the Hubble parameter $H \equiv \frac{\dot{a}}{a}$. The Hubble parameter is the measure

of the expansion rate of the Universe, i.e. how fast the object at a certain distance recede from us and it's usually measured in $km \cdot s^{-1} \cdot Mpc^{-1}$. It has physical dimensions of an inverse time and it is the parameter that sets the scale of the cosmological evolution.

Those equations arise from the "space" and "time" components of the Einstein equations, respectively. Note that the off diagonal terms of the Einstein equations do not contribute as the metric and the stress energy tensor are diagonal.

There is also a third equation, that is functionally dependent on the other two, which we can obtain from the continuity equation of the stress-energy tensor

$$D_\mu T^{\mu\nu} = 0 \Rightarrow \dot{\rho} = -3H(\rho + p) \tag{2.11}$$

the three Friedmann equations can be solved provided an equation of state that relates ρ with p. Such equation is usually assumed to be of the form

$$p = w\rho \tag{2.12}$$

with this we can solve the Friedmann equations and finding the time evolution of the scale factor in the case of a flat ($k = 0$) Universe dominated by a single kind of fluid with a specific value of w. Plugging it in the continuity equation (2.11) we get:

$$\frac{d\log\rho}{d\log a} = -3(1+w) \quad \Rightarrow \quad \rho \propto a^{-3(1+w)} \tag{2.13}$$

which, combined with the first Friedmann equation (2.9) leads to

$$a(t) \propto \begin{cases} t^{\frac{2}{3(1+w)}} & w \neq -1 \\ \mathrm{e}^{Ht} & w = -1 \end{cases} \tag{2.14}$$

some notable cases are $w = 0$, corresponding to an Universe dominated by non relativistic matter, in which case we get $a(t) \propto t^{2/3}$, $w = 1/3$, corresponding to relativistic particles (radiation), leading to $a(t) \propto t^{1/2}$. A last and less intuitive, but still very relevant, case is $w = -1$, corresponding to a fluid exerting negative pressure, which leads to the second solution in equation (2.14), i.e. an exponential expansion. As we will see this will be the equation of state describing Dark Energy.

Another important remark about equation (2.13) is the power law scaling of the density:

$$\rho(a) \propto \begin{cases} a^{-4} & w = 1/3 \quad \text{(radiation)} \\ a^{-3} & w = 0 \quad \text{(matter)} \\ \text{constant} & w = -1 \quad \text{(dark energy)} \end{cases} \tag{2.15}$$

Intuitively, the energy density of relativistic particles decreases not only due to the average number per unit volume dropping as the Universe expands, like non relativistic matter, but also due to relativistic Doppler shift, which adds one more negative power of the scale factor in the scaling. Dark energy, instead, has the same energy density at all time. We can guess that if the Universe is composed by those three kind of fluids, each one has dominated its energy budget, and thus its evolution, at different times, first radiation, then matter, and eventually Dark Energy.

2.3 The matter and energy content of the Universe

Now that we have the Friedmann equations and some basic solutions we can ask ourselves what are the ingredients that make it. It turns out that the matter that we can "see", namely the baryonic matter that makes up stars, amounts only a small fraction of the total balance that participate in the evolution of the Universe.

We first define the critical density ρ_c and the density parameter Ω, in this way.

The critical density is defined as the density required to have a flat Universe. By setting $k = 0$ in the first equation of (2.9) we obtain

$$\rho_c(t) = \frac{3H(t)^2}{8\pi G} \tag{2.16}$$

the Ω parameter is defined as the ratio between the observed density $\rho(t)$ and the critical density

$$\Omega(t) = \frac{\rho(t)}{\rho_c(t)}. \tag{2.17}$$

We can then rewrite the first Friedmann equation as

$$\Omega(t) - 1 = \frac{k}{(a(t)H(t))^2} \tag{2.18}$$

We can thus see that the Ω parameter is related to the spatial curvature of the Universe k. Not only that, but since k is constant if $\Omega(t)$ were to be larger than one at one time it would imply a positive (negative) curvature i.e. a closed (open) Universe at all times. According to observations the Universe is composed by dark energy, accelerating the Universe expansion, dark matter and baryonic matter. Only the last one is directly observed, the other only produce gravitational effects. We will explore each one of those more in detail in the following sections.

While we treated the simplified case of only one type of fluid characterized by a single w parameter, there can be may different fluids, each one contributing to the total energy density[2]

$$\Omega_{tot} = \Omega_\Lambda + \Omega_b + \Omega_{\text{CDM}} + \Omega_r. \tag{2.19}$$

In words, the density parameters represent the budget top the total mass-energy content of the Universe from each source. Measurements of the density parameters at the current time give

$$\Omega_{0,\Lambda} + \Omega_{0,b} + \Omega_{0,\text{CDM}} + \Omega_{0,r} = 1.00 \pm 0.02 \tag{2.20}$$

giving a value of the curvature parameter Ω_k compatible with 0, which would imply a flat Universe.

Another useful way to rewrite the Friedmann equation in terms of the present day Hubble constant H_0 and $\Omega_{0,i}$ parameters is [8]

$$H(a) = H_0\sqrt{\Omega_{0,m}a^{-3} + \Omega_{0,r}a^{-4} + \Omega_{0,\Lambda}}. \tag{2.21}$$

[2]Another commonly used parameter in cosmology related to Ω_i, where i labels a certain fluid is $\omega_i \equiv \Omega_i h^2$, where h is the reduced Hubble constant $h \equiv H_0/(100\,\text{km}\,\text{s}^{-1}\,\text{Mpc}^{-1})$. Not to be mistaken with the proportionality constant in the equation of state w.

2.3.1 The cosmological constant

The symmetries in General Relativity strictly constrain the kinds of terms that appear in the field equations (2.6), but we still omitted one term. A more general version would also include a term proportional to the metric

$$R_{\mu\nu} - \frac{1}{2}g_{\mu\nu}R = 8\pi G T_{\mu\nu} - \Lambda g_{\mu\nu} \tag{2.22}$$

Where the Greek letter Λ denotes the cosmological constant[3]. Einstein first introduced this term because it was the only way to obtain a static solution of the Friedmann equations, i.e. $\dot{a} = \ddot{a} = 0$, but deemed this an error when Hubble showed without doubt that the Universe is expanding. The discovery that the expansion of the Universe is accelerating from the observation of Type Ia supernovae led physicists to introduce this term again, despite not with its first intended use of enforcing a static Universe[4], but in order to explain its accelerating expansion.

We can see the effect of the cosmological constant by introducing the Λ-shifted the stress-energy tensor $\widetilde{T}_{\mu\nu} \equiv T_{\mu\nu} - \frac{\Lambda}{8\pi G}g_{\mu\nu}$, so that we re-obtain the Einstein equations (2.6) with $\widetilde{T}_{\mu\nu}$ instead of $T_{\mu\nu}$. The "effective" pressure $\widetilde{p}$ and density $\widetilde{\rho}$ of the shifted stress-energy tensor are related to the standard p and ρ by

$$\begin{cases} \widetilde{p} = p - \frac{\Lambda}{8\pi G} \\ \widetilde{\rho} = \rho + \frac{\Lambda}{8\pi G} \end{cases} \tag{2.23}$$

We can now solve the equations for the case of an empty and flat Universe, $T_{\mu\nu} = 0$ and $k = 0$, i.e. when the only relevant physical quantity in the evolution of the Universe is the cosmological constant. In this case

$$\widetilde{\rho} = -\widetilde{p} = \frac{\Lambda}{8\pi G} \tag{2.24}$$

note that this is exactly the $w = -1$ condition for the equation of state and indeed this empty universe with only a cosmological constant leads to an exponential expansion

$$H^2 = \frac{\Lambda}{3} = const \Rightarrow a(t) \propto \exp\left(\sqrt{\frac{\Lambda}{3}}t\right). \tag{2.25}$$

A period in the Universe evolution where $p = -\rho$, and consequently equation (2.25) holds, is called a *de Sitter* phase.

As we said, observations led to estimate a positive value of Λ to explain the accelerating expansion. Not only that, but it turns out that the cosmological constant accounts for the most of the energetic budget of the Universe with a $\Omega_\Lambda \simeq 0.7$.

In the modern paradigm the cosmological constant is related with the energy density of the vacuum due to the quantum fluctuations of the fields that permeate space. It should be noted, however, that QFT calculations based on the Standard Model of particle physics fail to estimate the correct value of Λ, with a discrepancy of about 120 orders of magnitude.

[3] Λ really has to be *constant*, it cannot depend on any spacetime variable due to the symmetries in the Einstein equations.

[4] Besides, the static solution was found to be unstable under small perturbations, thus not physically viable as the universe is not *perfectly* uniform.

2.3.2 Dark matter

Both cosmological and astrophysical observations have provided strong evidence that the luminous baryonic matter that we are used to, and that we can easily see with our telescopes only accounts to a fraction of the matter content of the Universe. Indeed, while baryonic matter amounts to about 5% of the total matter-energy budget, the Universe appears to be composed of about 26% of a kind of matter that eludes direct detection, but exerts gravitational force on galactic scales and above.

The evidence of the presence of dark matter is abundant, here we will summarize some of the observations that led to its introduction:

Galaxy rotation curves: a simple consideration of the Newtonian dynamics of stars orbiting a galactic center would lead to the scaling law $v \sim R^{-1/2}$ at large radii, i.e. ad distances from the galactic center encompassing most of the matter content of the galaxy itself. The observed data instead shows, after the expected linear increase, an almost constant profile, as if there was a halo of invisible matter encompassing the whole galaxy, and extending a sizeable amount beyond its visible boundaries. Similar considerations hold for the velocity dispersion of stars in elliptical galaxies, which is different from the one predicted by the virial theorem.

CMB anisotropies: the power spectrum of the cosmic microwave background (CMB) cannot be explained with the sole presence of baryonic matter. While dark matter does not interact nor strongly nor electromagnetically it still affects baryonic matter through its gravitational potential, leaving an imprint on the perturbations measured by CMB probes such as Planck[5][1]

Structure formation: another evidence comes from the observation of Large Scale Structures. During the era of radiation domination perturbations should have been washed away by the radiation pressure, smoothing out inhomogeneities and preventing structure formation. Instead, dark matter was not affected by this process and remained clumped, seeding the formation of the Large Scale Structure we observe today.

Galaxy clusters: the presence of a huge amount of non luminous matter in galaxy clusters can be inferred in three different ways: from the measurement of velocity dispersion of galaxies, analogously to the observations of stars in elliptical galaxies, from the study of the X-ray flux emitted by hot gas in the cluster, and by the observation of gravitational lensing.

this is not an exhaustive list, there are far more astrophysical and cosmological studies that all lead to estimate the same Ω_{CDM} parameter of about 0.26, compared to a baryon density parameter $\Omega_b \simeq 0.05$.

In addition to an agreement on the amount of dark matter, we also know some general properties that it must have:

- it's collisionless, particles do not interact with each other much, if at all
- it's non baryonic, i.e. not composed of protons and neutrons
- it's cold, meaning that it's kinetic energy is currently much smaller than its mass.

Despite all the evidence of the existence of dark matter its nature is still unknown. Two popular possibilities that can be fitted in extensions of the Standard Model of particle physics are Weakly Interacting Massive Particles (WIMPs), for example massive sterile neutrinos, and axions. However at this time there still has not been any detection of dark matter particles from a particle physics experiment.

[5] `https://www.cosmos.esa.int/web/planck`

Another possible dark matter candidate are Primordial Black Holes (PBHs), which are black holes that could have been produced in the early Universe during radiation domination from the collapse of density fluctuation produced by inflation. They have been first hypothesized by Zel'dovich [9] and Hawking [10], and recently came back in the spotlight after LIGO's[6] begun detecting mergers of black holes [11], some of which having an anomalously large mass that could be explained by their primordial origin [12]. For reviews about PBHs see for example [13, 14].

2.3.3 The ΛCDM model

All the information we discussed in the previous chapter is summarized in what is called the "standard model" of cosmology: the ΛCDM model.

The model explains the general properties of the Universe we observe, such as the CMB power spectrum, the large scale structures, the observed abundances of elements and the accelerating expansion of the Universe.

It should be noted however that some discrepancies still exist, such as the cosmological lithium problem and the H_0 tension, consisting in the fact that local measurements of the Hubble constant based on the distance ladder and CMB estimations do not agree [15].

As the name suggests the ΛCDM includes, in addition to ordinary matter, also cold dark matter and dark energy. It assumes the Universe begun its history in an extremely hot and dens state and quickly expanded, this process is known as the (hot) Big Bang.

At its core the parameterization of the model requires only six parameters, however there are many possible extensions.

One possible parameterization of the base ΛCDM model is

$$\text{Parameter} \;\Big|\; \Omega_c h^2 \quad \Omega_b h^2 \quad 100\theta_{\text{MC}} \quad \tau \quad \ln(10^{10} A_s) \quad n_s$$

which is the one used by the Planck collaboration [1]. We already encountered the first two parameters. θ_{MC} is the sound horizon at recombination, τ is the reionization optical depth and A_s and n_s are parameters describing the primordial Universe, respectively the amplitude of the primordial power spectrum and its spectral index.

From that parameterization many other quantities can be derived, for example the age of the Universe can be estimated to be about 13.8 billion years and the current Hubble constant is found to be about $67\, km\, s^{-1}\, Mpc^{-1}$.

2.4 Distances and horizons in cosmology

In this sections we introduce some useful quantities that are commonly used in cosmology.

As we said the Universe is observed to be expanding, the scale factor $a(t)$ is increasing with time. This expansion also affects the photons that have been emitted a long time ago far away and reach us today, which become redshifted. Therefore it is convenient to define a quantity which describes the distance - and time - of a patch of the Universe we are observing based on this physical effect. Thus we define the redshift z as

$$z + 1 \equiv \frac{a(t_0)}{a(t)} \tag{2.26}$$

where t is the time when the signal was emitted and t_0 is today. The scale factor is defined up to a multiplicative constant, and it's usually assumed $a(t_0) = 1$, so $z + 1 = a(t)^{-1}$.

[6] https://www.ligo.org/

As we know the casual connection of points in spacetime is determined by them being inside or outside each other's lightcone. Lightcones are the solutions of the equation

$$ds^2 = 0 \tag{2.27}$$

with ds^2 a suitable metric, in our case the FRW metric (2.2), which can be recast as

$$ds^2 = c^2dt^2 - a(t)^2\left[d\chi^2 + f(\chi)^2 d\Omega^2\right] \tag{2.28}$$

with $f(\chi)$ a different function of χ based on the spatial curvature k. The comoving particle horizon is then, assuming an homogeneous and isotropic Universe and taking $d\Omega = 0$

$$r_p(t) \equiv \chi(t) = \int_0^t \frac{cdt'}{a(t')} = c\int_0^a \mathrm{d}\ln a \left(\frac{1}{aH}\right) = c\tau \tag{2.29}$$

where in the last equality we exploited the relation we found earlier for the conformal time. The comoving horizon is therefore the logarithmic integral of the comoving Hubble radius c/aH, which we will define below. The related physical particle horizon is

$$d_p(t) = a(t)r_p(t) = a(t)\int_0^t \frac{cdt'}{a(t')} \tag{2.30}$$

due to the scale factor in the denominator and the fact that $a(t) \to 0$ as t goes to 0 the particle horizon could become infinite, meaning that an observer would be in casual connection with the whole Universe.

Using (2.14) we can find an approximate expression for $d_p(t)$, for $w > -1/3$, otherwise the integral would diverge

$$d_p(t) \simeq \frac{3(1+w)}{1+3w}ct = \frac{2}{1+3w}\frac{c}{H}. \tag{2.31}$$

Note that $w > -1/3$ implies $\ddot{a} < 0$, a decelerating expansion. Therefore we have a finite particle horizon only in the case of a primordial universe characterized by a decelerating expansion.

Another useful time and distance scale can be derived from the Hubble constant: the Hubble time and the physical and comoving Hubble radii

$$t_H = \frac{a}{\dot{a}} = \frac{1}{H} \qquad R_H = ct_H \qquad r_H = \frac{R_H}{a} = \frac{c}{\dot{a}} = \frac{c}{aH} \tag{2.32}$$

we end this section noting that R_H and d_p, despite having a different physical meaning, have the same order of magnitude in matter or radiation dominated Universes. This is however not true in general. The crucial difference is that, while particles separated by a particle horizon could have never been in communication, if they are separated by a Hubble radius at a given time t only means they they cannot communicate at t. In other words, the particle horizon could be much greater than the Hubble radius if at some point during the evolution of the Universe the latter shrunk. This is not possible during radiation or matter domination, but as we will see that is what happens during inflation [16].

2.5 Perturbations in cosmology

In this section we will review some notions and formalism pertaining the study of perturbations in cosmology, without delving too much into the physics that imprinted them, that will be the topic of the next chapter.

Given the cosmological principle we are not interested on the evolution of a specific element of the Universe, but rather on the statistical properties of the observable that we can measure, usually represented as a random field.

For example we could be interested in the density fluctuations, for which could be convenient to define a dimensionless, zero-mean density contrast $\delta(\boldsymbol{x})$

$$\delta(\boldsymbol{x}) \equiv \frac{\rho(\boldsymbol{x}) - \overline{\rho}}{\overline{\rho}} \tag{2.33}$$

and study the statistical observable that we can measure. While the field itself is not isotropic nor homogeneous, we expect the statistical observables that we can extract to respect those symmetries.

2.5.1 Correlation function and power spectrum

Given a generic random field $\delta(\boldsymbol{x}, t)$ we can define the set of n-points correlation functions $\xi^{(n)}(\boldsymbol{x}_1, ..., \boldsymbol{x}_n)$

$$\begin{aligned}
&\xi_t^{(2)}(\boldsymbol{x}_1, \boldsymbol{x}_2) \equiv \langle \delta(\boldsymbol{x}_1, t)\delta(\boldsymbol{x}_2, t)\rangle \\
&\xi_t^{(3)}(\boldsymbol{x}_1, \boldsymbol{x}_2, \boldsymbol{x}_3) \equiv \langle \delta(\boldsymbol{x}_1, t)\delta(\boldsymbol{x}_2, t)\delta(\boldsymbol{x}_3, t)\rangle \\
&\vdots \\
&\xi_t^{(n)}(\boldsymbol{x}_1, ..., \boldsymbol{x}_n) \equiv \langle \delta(\boldsymbol{x}_1, t), ..., \delta(\boldsymbol{x}_n, t)\rangle
\end{aligned} \tag{2.34}$$

with $\langle\cdot\rangle$ denoting the ensemble average. If the random field is gaussian then the only meaningful correlation function is $\xi^{(2)}$, all the others are either 0, in the case of odd n, or can be written in terms of $\xi^{(2)}$.

The homogeneity condition applied to the 2-points correlation function makes it so it's only dependant on the difference of the coordinates, while the isotropy further simplifies it, reducing the dependence only on the distance between the two points

$$\xi_t^{(2)}(\boldsymbol{x}_1, \boldsymbol{x}_2) \xrightarrow{homogeneity} \xi_t^{(2)}(\boldsymbol{x}_1 - \boldsymbol{x}_2) \xrightarrow{isotropy} \xi_t^{(2)}(|\boldsymbol{x}_1 - \boldsymbol{x}_2|) = \xi_t^{(2)}(r) \tag{2.35}$$

In order to better exploit the translational invariance it's useful to switch to Fourier space

$$\delta(\boldsymbol{x}, t) = \frac{1}{(2\pi)^3}\int d^3k e^{i\boldsymbol{k}\cdot\boldsymbol{x}}\delta(\boldsymbol{k}, t) \tag{2.36}$$

the ensemble variance of the Fourier modes of the field is called the power spectrum $P(k)$

$$\left\langle \delta(k)\delta(k')\right\rangle = (2\pi)^3 P(k)\delta^{(3)}(k - k') \tag{2.37}$$

where the Dirac delta function is due to the homogeneity. As with the correlation functions, one can define also higher order correlators, such as the bispectrum, but if the random field is gaussian the only meaningful one is the power spectrum. In fact the two quantities are related by a Fourier transform:

$$\begin{aligned}\xi(r) = \langle\delta(x+r)\delta(x)\rangle &= \left\langle \frac{1}{(2\pi)^3}\int \mathrm{d}^3k e^{i\mathbf{k}\cdot(\mathbf{x}+\mathbf{r})}\delta(\boldsymbol{k})\frac{1}{(2\pi)^3}\int \mathrm{d}^3k' e^{i\mathbf{k}'\cdot\mathbf{x}}\delta(\boldsymbol{k'})\right\rangle \\ &= \frac{1}{(2\pi)^3}\int \mathrm{d}^3k \int \mathrm{d}^3k' e^{i\mathbf{k}\cdot(\mathbf{x}+\mathbf{r})}e^{i\mathbf{k}'\cdot\mathbf{x}}\delta^{(3)}(\boldsymbol{k}+\boldsymbol{k'})P(k) \\ &= \frac{1}{(2\pi)^3}\int \mathrm{d}^3k e^{i\mathbf{k}\cdot\mathbf{r}}P(k)\end{aligned} \tag{2.38}$$

The power spectrum $P(k)$ has the dimension of a length cubed. It is convenient to define the dimensionless power spectrum $\mathcal{P}(k)$

$$\mathcal{P}(k) \equiv \frac{k^3}{2\pi^2}P(k) \tag{2.39}$$

that will simplify the notation in certain situations, in particular when dealing with the primordial power spectrum.

2.5.2 Angular power spectrum

In this section we derive the relation between the three dimensional power spectrum of a random field and its angular power spectrum at a certain distance r, corresponding to an observed frequency $\nu = \nu_0/(1+z)$. This will be useful because IM experiments will measure the angular power spectrum at a certain redshift z at which corresponds a comoving radius r_0, but physical computations are much more convenient in three dimensional coordinates.

We neglect redshift space distortions in this derivation. Their effect would be to shift a patch of the IGM inside or outside the redshift slice we selected, depending on its peculiar velocity. Equivalently, we assume the power spectrum to be isotropic [17].

$$\delta(\hat{\mathbf{n}},\nu) = \int \mathrm{d}r W(r,r_0)\delta(\hat{\mathbf{n}},r) \tag{2.40}$$

where $\hat{\mathbf{n}}$ is the direction of observation, $W(r,r_0)$ is a window function centered at r_0, corresponding to the observed frequency ν, and has a width in comoving radial coordinates δr.

The field $\delta(\hat{\mathbf{n}},r) = \delta(\mathbf{x})$ can be expanded in Fourier space

$$\delta(\mathbf{x}) = \frac{1}{(2\pi)^3}\int \mathrm{d}^3\mathrm{k}\delta(\mathbf{k})e^{i\mathbf{k}\cdot\mathbf{x}} \tag{2.41}$$

then, by using the spherical wave expansion of a plane wave

$$e^{i\mathbf{k}\cdot\mathbf{x}} = \sum_{\ell m} 4\pi i^\ell j_\ell(kr)Y^*_{\ell m}(\hat{\mathbf{k}})Y_{\ell m}(\hat{\mathbf{n}}), \tag{2.42}$$

where $j_\ell(kr)$ are the spherical Bessel functions, we obtain the expression

$$\delta(\mathbf{x}) = \frac{1}{(2\pi)^3}\int \mathrm{d}^3\mathrm{k}\delta(\mathbf{k})\sum_{\ell m} 4\pi i^\ell j_\ell(kr)Y^*_{\ell m}(\hat{\mathbf{k}})Y_{\ell m}(\hat{\mathbf{n}}). \tag{2.43}$$

The field $\delta(\hat{\mathbf{n}},\nu)$ can also be expanded in spherical harmonics

$$\delta(\hat{\mathbf{n}},\nu) = \sum_{\ell=0}^{\infty}\sum_{m=-\ell}^{\ell} a_{\ell m}(\nu)Y_{\ell m}(\hat{\mathbf{n}}). \tag{2.44}$$

By relating equations (2.43), (2.40) and (2.44) we can obtain an expression for the spherical harmonics coefficients

$$a_{\ell m}(\nu) = 4\pi i^{\ell} \int \frac{\mathrm{d}^3 k}{(2\pi)^3} \mathcal{T}_{\ell}(k,\nu) Y^*_{\ell m}(\hat{\mathbf{k}}) \delta(k,\nu) \tag{2.45}$$

with the functions $\mathcal{T}_{\ell}(k,\nu)$ defined as

$$\mathcal{T}_{\ell}(k,\nu) = \int \mathrm{d}r W(r,r_0) j_{\ell}(kr). \tag{2.46}$$

The angular power spectrum of a field is given by the expectation value of the variance of the spherical harmonics coefficients $a_{\ell m}$

$$\langle a_{\ell m}(\nu_1) a^*_{\ell' m'}(\nu_2) \rangle = \delta_{\ell\ell'} \delta_{mm'} C_{\ell}(\nu_1,\nu_2). \tag{2.47}$$

By plugging equation (2.45) into (2.47), and using the relation for the 3D power spectrum (2.37) we obtain the final result

$$C_{\ell}\left(\nu_1,\nu_2\right) = 4\pi \int \frac{d^3 k}{(2\pi)^3} P(k) \mathcal{T}_{\ell}\left(k,\nu_1\right) \mathcal{T}_{\ell}\left(k,\nu_2\right) = \frac{2}{\pi} \int \mathrm{d}k k^2 P(k) \mathcal{T}_{\ell}\left(k,\nu_1\right) \mathcal{T}_{\ell}\left(k,\nu_2\right). \tag{2.48}$$

with $\nu_i(z) = \nu_0/(1+z)$. We note that in this work we are interested in the case where $\nu_1 = \nu_2 = \nu$, but the cross frequency power spectrum can also be useful, for example it can be utilized for foreground removal techniques [17].

Chapter 3

Early Universe

3.1 Inflation

Despite doing a good job explaining the observable Universe, the ΛCDM model still has flaws. First and foremost, it fails to explain what is the origin of the cosmological constant and of the dark matter, as well as their makeup, these components are only introduced as free parameters with no physical interpretation. Additionally, with the increase in precision of cosmological measurements, some inconsistencies are emerging, such as the already mentioned Hubble tension.

Quantum perturbations in the fields that drove inflation are also responsible of the inhomogeneities that we observe today, as summarized in figure 3.1. In the inflationary paradigm those microscopic perturbations were magnified to cosmological scales, and those fluctuations appear at every stage of the evolution of the Universe. They are imprinted on the CMB famously captured by the Planck collaboration, they affect the clumping on matter in the late Universe and the formation of the cosmic web, observed in galaxy surveys, and last but not least they cause hydrogen density perturbations in the intermediate redshift range, which Intensity Mapping experiments can capture.

In the following we will focus on two glaring issues of this model that led cosmologists to introduce an inflationary phase shortly after the Big Bang: the horizon problem and the flatness problem.

3.1.1 Motivation: the hot Big Bang problems

The horizon problem

We already computed the particle horizon in the previous section and we found it to be finite for $w > -1/3$. However our observations, on which the Cosmological principle is based, clearly show that even regions that should have not been in casual contact with each other according to the Big Bang model appear to have the same physical properties.

The most glaring example is the CMB: as shown in figure 3.2 we measure the same temperature looking everywhere in the sky, with fluctuations on the order of one part per 10^5, but the horizon at the time of the emission of the CMB, at $t_{\mathrm{CMB}} = 300\,000$ yr, is about 205 Mpc, corresponding to a subtended angle of about one degree in a CMB sky map. Regions separated by more than this angle should not have exchanged any information and therefore we wouldn't expect them to be in thermal equilibrium. The CMB then consists of approximately 10^5 casually disconnected patches that somehow all appear to us at the same temperature.

For simplicity we work with the Hubble radius. From the expression for the comoving Hubble radius we have

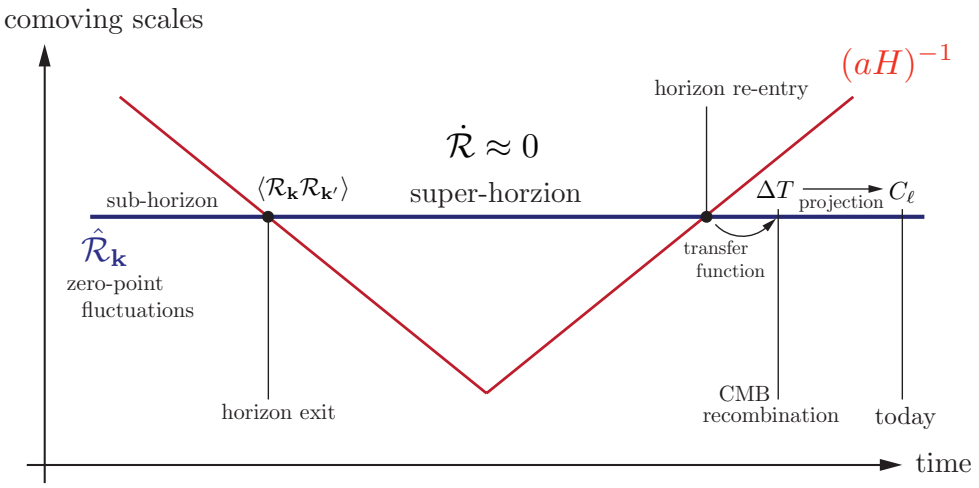

Figure 3.1: Schematic representation of the creation and evolution of perturbation in inflationary cosmology. Perturbations are created as quantum fluctuations, as their comoving scale (blue) exits the Hubble horizon (red) during inflation, they remain frozen until they eventually re-enter the horizon after inflation ends. They then evolve to become the perturbations we observe today, such as the CMB temperature fluctuations. Taken from [18].

$$\dot{r}_H = -\frac{\ddot{a}}{\dot{a}^2} > 0 \quad \text{for} \quad w > -1/3, \tag{3.1}$$

In order to solve this the horizon problem we can assume that there has been a brief moment of accelerated expansion in the very early Universe that shrunk the horizon size, $\dot{r}_H < 0$ separating regions that were previously casually connected at an earlier time, as shown in figure 3.3.

If the horizon size at the moment of the beginning of this accelerated expansion at time t_{in}, called *inflation*, was greater than the horizon size today t_0 then our observations of an isotropic CMB make sense.

The quantity of interest to us is then how much the Universe between t_{in} and t_{fin}, setting the beginning and end of inflation. This is measured in e-foldings, defined as

$$\mathcal{N} = \ln\left(\frac{a(t_{fin})}{a(t_{in})}\right). \tag{3.2}$$

In order to explain the current observations we have $\mathcal{N}_{min} \approx 60$. If we assume an exponential expansion

$$\frac{a(t_{fin})}{a(t_{in})} = e^{H(t_{fin}-t_{in})} \tag{3.3}$$

then $\mathcal{N}$ is also a measure of the time passing in the inflationary phase.

The flatness problem

As we already hinted in section 2.3, current measurements of the density parameter are compatible with a flat Universe, $\Omega_{0,tot} \simeq 1$.

But how does Ω evolves with time? Let's recall the Friedmann equation

$$\Omega(t) - 1 = \frac{k}{H(t)^2 a(t)^2} \propto \frac{k}{a^{2-3(1+w)}} = k a^{3w+1} \tag{3.4}$$

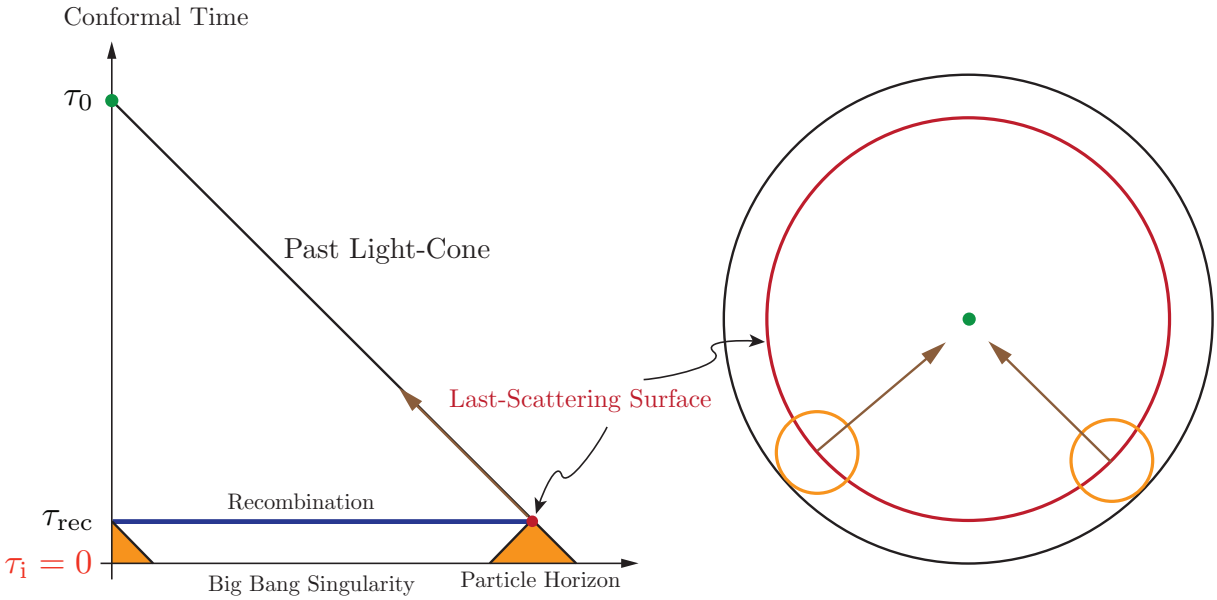

Figure 3.2: Conformal diagram of the horizon problem in the case of the CMB. The radiation from the two circles appears to us at the same temperature, but they were not casually connected at the time of emission. Taken from [18]

for both radiation ($w = 1/3$) and matter ($w = 0$) we get that if $\Omega - 1$ is not exactly 0 at a certain early time then it will grow as a^2 or a^4, respectively. But by how much will it grow? The earliest time we expect the Friedmann equation to hold is the Planck time $t_P \approx 10^{-43}\,s$. The temperature at that time was $T_P = m_P \approx 10^{19}$ GeV or 10^{32} K.

Manipulating the previous equation we obtain

$$\Omega^{-1}(t_P) - 1 = (\Omega_0^{-1} - 1)\left(\frac{T_0}{T_P}\right)^2 = (\Omega_0^{-1} - 1)10^{-64}, \tag{3.5}$$

where T_0 is the CMB temperature today. The Universe in its initial conditions should have to be amazingly fine tuned to reproduce the flatness we observe today.

As with the horizon problem, the inflationary phase can solve this inconsistency. Let's recall the the expression for the comoving Hubble radius $r_H = c/aH$, plug it in equation (3.4):

$$\Omega(t) - 1 = k r_H^2 \tag{3.6}$$

then, if the Universe endures a phase where the Hubble radius shrinks this would bring $\Omega(t)$ close to 1. It can be shown that the Universe must expands by 60 e-foldings in order to obtain the flatness we observe today, as in the case of the horizon problem.

3.1.2 Inflation dynamics

As we anticipated, a phase of accelerated expansion, with $\dot{r}_H < 0$ would potentially solves the inconsistencies in the Hot Big Bang, additionally it would provide us a way to physically motivate the fluctuation we observe today.

In order to achieve this accelerating phase an equation of state parameter $w < -1/3$ is required, meaning $P < -\rho/3$. This condition might seem physically unlikely but it's possible to realize by simply adding a scalar field ϕ, called inflaton, with action

$$\mathcal{S}_\phi = \int d^4x\sqrt{-g}\mathcal{L}_\phi \tag{3.7}$$

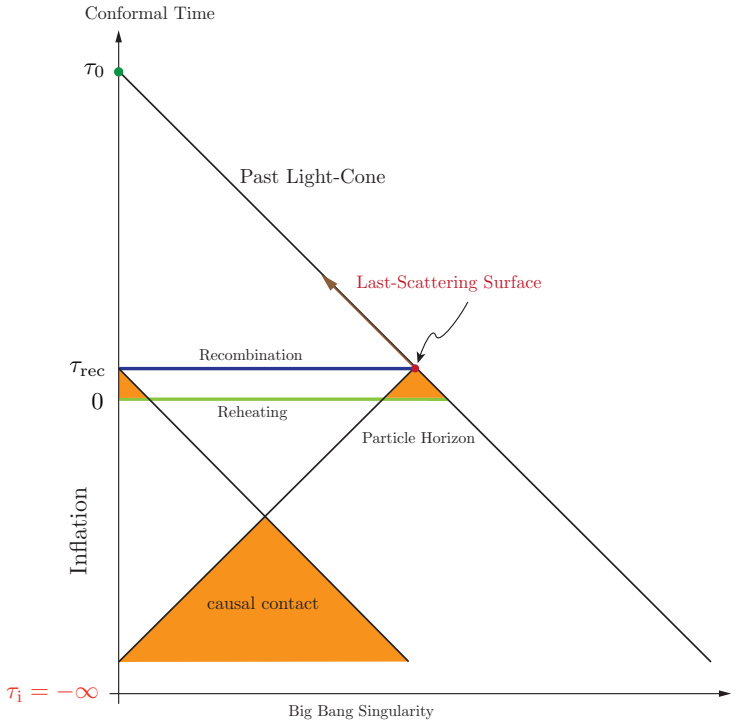

Figure 3.3: Conformal diagram of inflationary cosmology, showing the solution to the horizon problem. Taken from [18].

such that the total action reads as $\mathcal{S} = \mathcal{S}_{\mathcal{HE}} + \mathcal{S}_\phi$, with the matter Lagrangian in equation (2.4) negligible by virtue of the no hair theorem. The scalar field Lagrangian is

$$\mathcal{L}_\phi = -\frac{1}{2} g^{\mu\nu} \partial_\mu \phi \partial_\nu \phi - V(\phi) \tag{3.8}$$

by applying the least action principle we can obtain the equation of motion for ϕ, that read

$$\ddot{\phi} + 3H\dot{\phi} - \frac{\nabla^2 \phi}{a^2} = -\partial_\phi V. \tag{3.9}$$

This is the standard equation for a scalar field rolling down a potential, with the additional $3H\dot{\phi}$ due to the friction caused by the expansion of the Universe.

The stress-energy tensor $T^\phi_{\mu\nu}$ can be derived from (2.7) and reads

$$T^\phi_{\mu\nu} = \partial_\mu \phi \partial_\nu \phi + g_{\mu\nu} \mathcal{L}_\phi \tag{3.10}$$

from which we can find the energy density ρ_ϕ and the pressure P_ϕ

$$\rho_\phi = \frac{1}{2}\dot{\phi}^2 + V(\phi) + \frac{(\nabla\phi)^2}{2a^2} \tag{3.11}$$

$$p_\phi = \frac{1}{2}\dot{\phi}^2 - V(\phi) - \frac{(\nabla\phi)^2}{6a^2} \tag{3.12}$$

To continue the analysis it's convenient to split the field ϕ in a homogeneous background term representing the classical solution, and a spatially dependant term, representing quantum fluctuations

$$\phi(\mathbf{x},t) \equiv \phi(t) + \delta\phi(\mathbf{x},t) \tag{3.13}$$

where the homogeneous term is the expectation value of the inflaton $\phi(t) = \langle\phi(\mathbf{x},t)\rangle$. We can do this under the reasonable assumption that the quantum fluctuations are small compared to the classical term and do not affect its evolution.

The homogeneous term and the fluctuation obey the equations

$$\ddot{\phi} + 3H\dot{\phi} + \partial_\phi V = 0. \tag{3.14}$$

$$\ddot{\delta\phi} + 3H\dot{\delta\phi} - \frac{\nabla^2\delta\phi}{a^2} = -\partial_\phi^2 V(\phi)\delta\phi \tag{3.15}$$

Background solution

The background solution is not dependent on spatial coordinates. Then $\nabla\phi(t) = 0$. The equation of state parameter w_ϕ for the background field $\phi(t)$ is

$$w_\phi = \frac{p_\phi}{\rho_\phi} = \frac{\frac{1}{2}\dot{\phi}^2 - V(\phi)}{\frac{1}{2}\dot{\phi}^2 + V(\phi)}. \tag{3.16}$$

Then, we can have a negative w_ϕ, implying an accelerating expansion and thus the necessary conditions for solving the horizon problem and the flatness problem if

$$\dot{\phi}^2 \ll V(\phi), \tag{3.17}$$

equation (3.17) is called the slow-roll condition: in words, to have a an inflating Universe it is required that the potential energy of the field driving inflation is much greater than its kinetic energy. In order for this to happen, the potential $V(\phi)$ must have a sufficiently flat shape at the value of ϕ related to the inflationary phase. As a consequence, we can also expect that the acceleration $\ddot{\phi}$ of the background inflaton field is negligible:

$$|\ddot{\phi}| \ll |3H\dot{\phi}|, |\partial_\phi V| \tag{3.18}$$

and the equation of motion simplifies to

$$3H\dot{\phi} = -\partial_\phi V \tag{3.19}$$

Assuming (3.17), the first Friedmann equation (2.9) becomes

$$H^2 \simeq \frac{8\pi G}{3} V(\phi) \tag{3.20}$$

The slow roll conditions can be parameterized by introducing the slow-roll parameters, functions of the Hubble constant, of the potential and its derivative with respect to ϕ

$$\begin{aligned} \epsilon &\equiv -\frac{\dot{H}}{H^2} \simeq \frac{1}{16\pi G}\left(\frac{\partial_\phi V}{V}\right)^2 \\ \eta &\equiv \frac{1}{3}\frac{\partial_\phi^2 V}{H^2} \simeq \frac{1}{8\pi G}\frac{\partial_\phi^2 V}{V} \\ \delta &\equiv \eta - \epsilon. \end{aligned} \tag{3.21}$$

The ϵ parameter quantifies the acceleration during inflation. In fact we have

$$\frac{\ddot{a}}{a} = \dot{H} + H^2 = (1-\epsilon)H^2, \tag{3.22}$$

as a consequence, inflation can happen as long as $\epsilon < 1$. In general, both ϵ and η are expected to be small $\epsilon, \eta \ll 1$ during the inflationary phase, in fact they are related respectively with the slow roll conditions (3.17) and (3.18).

Let's show this for η. Deriving the Friedmann equation with respect to t we have

$$3H\ddot{\phi} \simeq -\partial_\phi^2 V\dot{\phi} \Rightarrow \ddot{\phi} \simeq \frac{\partial_\phi^2 V\dot{\phi}}{3H}. \tag{3.23}$$

Using (3.18) we have

$$\frac{\partial_\phi^2 V\dot{\phi}}{3H} \ll 3H\dot{\phi} \Rightarrow \eta \ll 1 \tag{3.24}$$

3.1.3 Scalar perturbations from inflation

We have characterized the evolution of the uniform background inflaton field that drove inflation. We are now interested in the dynamics of the perturbation $\delta\phi(\mathbf{x}, t)$ which, in the inflationary paradigm, provides the seeds for the fluctuations observed in the late Universe.

In the inflationary phase the inflaton field dominates the energy budget of the Universe and its quantum fluctuations $\delta\phi$ are tightly coupled with the metric: perturbations of ϕ will perturb the stress energy tensor, affecting the metric through the Einstein equations, while in turn perturbation of the metric will affect the evolution of the field by perturbing the equation of motion (3.15)

$$\delta\phi \Leftrightarrow \delta T_{\mu\nu} \Leftrightarrow \delta g_{\mu\nu}. \tag{3.25}$$

This issue is connected to to the choice of a gauge. When dealing with a perturbed space-time, one must pay attention to the fact that a gauge choice, i.e. a particular choice of coordinates, might introduce unphysical perturbations, or hide real ones. In other words, matter perturbations might be traded for metric perturbations and vice versa. Therefore one to be careful when performing calculations in a fixed gauge, or use gauge invariant quantities in order to remove the issue of a gauge choice.

Since we are interested with scalar perturbations, we must introduce gauge invariant quantities that can be used to describe such fluctuations such the curvature perturbation on uniform-density hypersurfaces ζ

$$\zeta = \Psi + \frac{H}{\dot{\bar{\rho}}}\delta\rho \tag{3.26}$$

where Ψ is the Bardeen potential. ζ defined as the curvature perturbation on a spacetime slicing with $\delta\rho = 0$.

Another important gauge invariant perturbation is the comoving curvature perturbation $\mathcal{R}$

$$\mathcal{R} = \Psi - \frac{H}{\bar{\rho} + \bar{p}}\delta q. \tag{3.27}$$

which is the metric perturbation in the comoving spacetime slicing, i.e. as measured by observers which see the cosmic expansion as isotropic, i.e. for whom the $\delta\phi = 0$, as the inflaton field sets the "clock" for inflation. It can be shown that $\mathcal{R}$ and ζ are both gauge invariant, additionally, they are equal during slow roll inflation

$$\mathcal{R} = \zeta \simeq \Psi + \frac{H}{\dot{\phi}}\delta\phi\Big|_{\text{(slow roll)}} \tag{3.28}$$

and conserved on super horizon scales, which allows us to compute them on horizon exit in order to known their value when they re enter the horizon after inflation has ended.

The recipe is then to find the classical equation of motion for $\mathcal{R}$ pr ζ by expanding the action to the second order in those quantities [1]

$$S_{(2)} = \frac{1}{2}\int \mathrm{d}^4x a^3 \frac{\dot{\phi}^2}{H^2}\left[\dot{\mathcal{R}}^2 - a^{-2}\left(\partial_i\mathcal{R}\right)^2\right] \tag{3.29}$$

then, defining the Mukhanov variable $v \equiv z\mathcal{R}$, where

$$z^2 \equiv a^2\frac{\dot{\phi}^2}{H^2} = 2a^2\epsilon \tag{3.30}$$

we obtain the action

$$S_{(2)} = \frac{1}{2}\int \mathrm{d}\tau\mathrm{d}^3x\left[\left(v'\right)^2 + \left(\partial_i v\right)^2 + \frac{z''}{z}v^2\right]. \tag{3.31}$$

This is the action of an harmonic oscillator with a time varying frequency, which depends on the scale factor and its derivatives, as well as on the slow roll parameter ϵ. Its equation of motion is the Mukhanov-Sasaki equation

$$v_k'' + \omega_k^2(\tau)v_k = 0 \qquad \text{with} \qquad \omega_k^2(\tau) \equiv k^2 - \frac{z''}{z}. \tag{3.32}$$

Where we defined the time and mode dependent frequency $\omega_k^2(\tau)$. Equation (3.32) is in general difficult to solve due to the dependence of z on the background dynamics, and thus on the particular inflationary model taken into consideration. It can however be solved in particular cases, as we will see below. For now, we introduce the de Sitter limit $\epsilon \to 0$ ($H = const.$) of the Mukhanov-Sasaki equation

$$v_k'' + \left(k^2 - \frac{2}{\tau^2}\right)v_k = 0. \tag{3.33}$$

The next step is the quantization of the field v. In order to do that, v is promoted to a quantum operator, and expressed in terms of creation and annihilation operators

$$\hat{v} = \int \frac{\mathrm{d}\mathbf{k}^3}{(2\pi)^3}\left[v_k(\tau)\hat{a}_{\mathbf{k}}e^{i\mathbf{k}\cdot\mathbf{x}} + v_k^*(\tau)\hat{a}_{\mathbf{k}}^\dagger e^{-i\mathbf{k}\cdot\mathbf{x}}\right] \tag{3.34}$$

satisfying the canonical commutation relations

[1] See for example [18] for a complete derivation.

$$\left[\hat{a}_{\mathbf{k}}, \hat{a}^{\dagger}_{\mathbf{k}'}\right] = (2\pi)^3 \delta\left(\mathbf{k} - \mathbf{k}'\right). \tag{3.35}$$

For equation (3.35) to hold it is required that the mode functions v_k satisfy the normalization

$$\langle v_k, v_k \rangle \equiv \frac{i}{\hbar}\left(v_k^* v_k' - v_k^{*\prime} v_k\right) = 1, \tag{3.36}$$

which provides a boundary condition on the mode functions. The problem is then the choice of the vacuum state. While this isn't a issue in Minkowsky spacetime and can be done by picking the state that minimizes the Hamiltonian of the system, there is not a unique way to define a vacuum state in a time dependant, expanding spacetime. To uniquely define a vacuum state, one can note that at sufficient early times all comoving scale of interest are inside the Hubble horizon, $k \gg aH$, therefore equation (3.32) reduces to

$$v_k'' + k^2 v_k = 0, \tag{3.37}$$

the equation for a simple harmonic oscillator, for which a unique solution exists. Therefore we can impose the initial condition

$$\lim_{\tau \to -\infty} v_k(\tau) = \frac{1}{\sqrt{2k}} e^{-ik\tau} \tag{3.38}$$

which defines the Bunch-Davies vacuum.

We are now ready to solve the Mukhanov-Sasaki equation. It's useful to first consider the de Sitter limit, eq (3.33), which has the exact solution

$$v_k(\tau) = \alpha \frac{e^{-ik\tau}}{\sqrt{2k}}\left(1 - \frac{i}{k\tau}\right) + \beta \frac{e^{ik\tau}}{\sqrt{2k}}\left(1 + \frac{i}{k\tau}\right) \tag{3.39}$$

where α and β are free parameters. By imposing equation (3.38) we fix $\alpha = 1$ and $\beta = 0$. The mode functions are then uniquely determined

$$v_k(\tau) = \frac{e^{-ik\tau}}{\sqrt{2k}}\left(1 - \frac{i}{k\tau}\right). \tag{3.40}$$

The power spectrum of $\hat{v}$ is then given by the zero-point fluctuations of the field

$$\begin{aligned}
\langle \hat{v}_{\mathbf{k}} \hat{v}_{\mathbf{k}'} \rangle &= \langle 0 \left| \hat{v}_{\mathbf{k}} \hat{v}_{\mathbf{k}'} \right| 0 \rangle \\
&= \left\langle 0 \left| \left(a^-_{\mathbf{k}} v_k + a^+_{-\mathbf{k}} v_k^*\right)\left(a^-_{\mathbf{k}'} v_{k'} + a^+_{-\mathbf{k}'} v_{k'}^*\right) \right| 0 \right\rangle \\
&= v_k v_{k'}^* \left\langle 0 \left| a^-_{\mathbf{k}} a^+_{-\mathbf{k}'} \right| 0 \right\rangle \\
&= v_k v_{k'}^* \left\langle 0 \left| \left[a^-_{\mathbf{k}}, a^+_{-\mathbf{k}'}\right] \right| 0 \right\rangle \\
&= |v_k|^2 \, \delta\left(\mathbf{k} + \mathbf{k}'\right) \\
&\equiv P_v(k) \delta\left(\mathbf{k} + \mathbf{k}'\right)
\end{aligned} \tag{3.41}$$

On super horizon scales, this gives

$$P_v(k) = \frac{1}{2k^3}\frac{1}{\tau^2} = \frac{1}{2k^3}(aH)^2 \tag{3.42}$$

recalling the definition of $v = z\mathcal{R}$, with $z^2 = 2a^2\epsilon$ we can obtain the power spectrum of ζ (or $\mathcal{R}$)

$$P_\zeta = \frac{1}{z^2} P_v. \tag{3.43}$$

The de Sitter limit is however physically inconsistent as inflation never ends in this regime, and ζ is meaningless. We are instead interested in the quasi de Sitter limit, in which we obtain

$$P_\zeta = \frac{1}{4k^3}\frac{H^2}{\epsilon} = \frac{1}{2k^3}\frac{H^4}{\dot{\phi}^2}. \tag{3.44}$$

Recalling that ζ freezes when outside the horizon we can compute (3.44) at horizon crossing, i.e. $k = aH$. The dimensionless power spectrum $\mathcal{P}_\zeta \equiv \frac{k^3}{2\pi^2} P_\zeta$ is then

$$\mathcal{P}_\zeta(k) = \left.\frac{1}{8\pi^2}\frac{H^2}{\epsilon}\right|_{k=aH} \tag{3.45}$$

The primordial power spectrum therefore has a scale dependence determined by the fact that different scales cross the horizon at different times, and that H and the slow roll parameter ϵ are a function of time. This deviation is non existing in the exact de Sitter case, as can be seen by looking at equation (3.42), and small in the quasi de Sitter case, a function of the slow roll parameter ϵ.

The scale dependence of the power spectrum can be parameterized my means of a scale dependence of the spectral index $n_s(k)$

$$\mathcal{P}_\zeta(k) = A_s \left(\frac{k}{k_0}\right)^{n_s(k)-1} = A_s \left(\frac{k}{k_0}\right)^{n_s - 1 + \frac{1}{2}\alpha_s \ln(k/k_0) + \frac{1}{3!}\beta_s \ln^2(k/k_0) + \frac{1}{4!}\gamma_s \ln^3(k/k_0) + \mathcal{O}\left(\ln^4(k/k_0)\right)} \tag{3.46}$$

where k_0 is a reference scale, called pivot scale, A_s is the scalar amplitude and the coefficients n_s, α_s, β_s and γ_s are the running parameters, not dependent on k, obtained from a logarithmic Taylor expansion of the spectral index and we truncated the series at the third order in $\ln(k/k_0)$.

In the slow roll approximation $\mathcal{P}_\zeta(k)$ can be written as a function of the slow roll potential and its derivatives, and the scalar index and the running parameters can be obtained as a function of the slow roll parameters [19, 20, 18, 21]

$$\begin{aligned} 1 - n_s &= 2\eta - 6\epsilon \\ \alpha_s &= -2\xi^2 + 16\eta\epsilon - 24\epsilon^2 \\ \beta_s &= 2\sigma^3 + 2\xi^2(\eta - 12\epsilon) - 32\epsilon\left(\eta^2 - 6\eta\epsilon + 6\epsilon^2\right). \end{aligned} \tag{3.47}$$

3.2 Primordial Black Holes

Primordial black holes (PBH) are black holes that might have been formed in the early Universe, typically during the radiation domination era, through physical processes that are different from the usual astrophysical collapse of a dying star. Those formation mechanisms allow in general the formation of black holes with a vast range of masses, in principle from the Planck mass to millions of solar masses. However we note that any PBH with mass $M_{\rm PBH} \lesssim 14^{15}$ g has by now evaporated due to Hawking radiation.

Many mechanisms that have been proposed for the formation of PBHs, such as collapse of cosmic strings [22, 23] or domain walls [24], with the mainstream model given by the collapse of large (in amplitude) overdensities seeded by curvature perturbations during the inflationary phase when they reenter the horizon. The latter is particularly interesting to us, since the amplitude

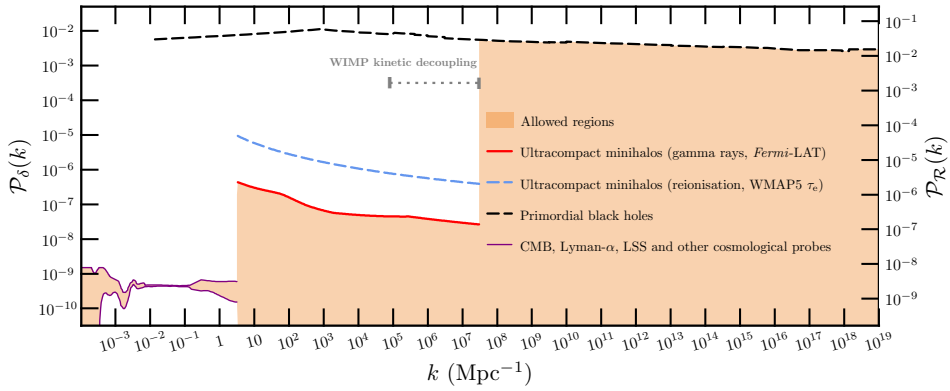

Figure 3.4: Constraints on the primordial curvature power spectrum $\mathcal{P}_\mathcal{R}(k)$. Taken from [26]

of perturbations at a certain comoving scale k is related with the primordial power spectrum $\mathcal{P}_\zeta(k)$. The PBH produced by this process are also called curvature primordial black holes (CPBH).

The motivations to be interested in PBHs are manifold: as they are relics of the early Universe, their characteristics, such as their mass function, spatial distribution and cross-correlation with other cosmological probes can tell us information about a time in which virtually no direct probe exist, in fact even their very existence would imply deviations from the standard history of the early Universe, independently on which is their formation mechanism. As PBHs interact only gravitationally they are also possible candidates to at least make up a fraction of the dark matter content of the universe [25]. Lastly, we mention that PBHs with masses $\gtrsim 10^2\ M_\odot$ could be the seeds of super massive black holes residing in the center of galaxies is also matter of investigation [7].

3.2.1 PBH formation and abundance

PBH formation has been extensively studied in recent years, especially after the beginning of gravitational wave observation era. Dynamics are highly nonlinear and have been expressed in various formalisms, such as peaks theory [27, 28], Press-Shechter collapse [29] and excursion set theory [30].

For an accurate study of PBH production and to link it with the primordial power spectrum, one should first compute in detail the nonlinear physical process that makes a primordial curvature perturbation collapse and produce a single CPBH, as a function of the shape and the profile of the perturbation. Then they should study the statistical properties of the cosmological curvature and density fields in nonlinear regime, to connect the previous result to the statistical observable, i.e. the power spectrum. This work is however outside the scope of this thesis, we refer to [27]

for a comprehensive study of CPBHs formation based on peaks theory.

The general rule is that a PBH forms when a perturbation characterized by a scale k and density contrast δ greater than a certain threshold δ_{th} re-enters the horizon.

We remind that, during inflation, quantum perturbations have been stretched to super horizon scales as the universe expanded by at least 60 e-folds. After inflation ended, the Hubble horizon started growing again, gradually encompassing larger and larger scales, which begun physically interacting.

A rough estimate of the relation between the the mass of a PBH and the scale of the perturbation that formed it can be obtained by relating the mass of the PBH to the horizon mass at the time of formation, when the scale of the perturbation re-enters the horizon [14].

$$\begin{aligned} M_{\rm PBH} = \gamma M_{\rm H}|_{\text{at formation}} &= \gamma \frac{4\pi}{3} \rho_{\rm form}\, H_{\rm form}^{-3} &&= \gamma \frac{4\pi}{3} \frac{3H_{\rm form}^2}{8\pi G} H_{\rm form}^{-3} \\ &&&= \gamma \frac{1}{2G} H_{\rm form}^{-1}\,. \end{aligned} \tag{3.48}$$

where we used the Friedmann equation and the γ parameter is a $\mathcal{O}(1)$ correction, related to the details of the gravitational collapse and can be found to be $\simeq 0.2$ during radiation domination [29].

Then, if we consider the formation of CPBHs, we have that the horizon scale is related with the scale of the perturbation by

$$aH|_{\text{at formation}} = k \tag{3.49}$$

which gives

$$M_{\rm PBH}(k) \simeq 30 M_\odot \left(\frac{\gamma}{0.2}\right) \left(\frac{g_{*,\,\rm form}}{10.75}\right)^{-1/6} \left(\frac{k}{2.9\times 10^5 {\rm Mpc}^{-1}}\right)^{-2} \tag{3.50}$$

this crude computation let us relate the PBH mass with the scale of the perturbation that generated it.

More accurate analytical calculations and physical simulations have confirmed that, when δ is close, but still greater than δ_{th}, $\delta - \delta_{th} \lesssim 10^{-2}$, the PBH formation process obeys the critical collapse scaling law [31, 32]

$$M_{\rm PBH} = k M_H (\delta - \delta_{th})^{\gamma_c} \tag{3.51}$$

where k^2, δ_{th} and γ_c are constants, depending on the nature of the fluid at horizon crossing, and γ_c in particular doesn't depend on the overdensity profile but only on the equation of state parameter w. While the exact values of those parameters can depend on the details of the methodology some common reference values are $\delta_{th} = 0.45$, $\gamma_c = 0.36$ and $k = 3.3$. Equation (3.51) has the effect of producing a tail in the distribution of $M_{\rm PBH}$ at small masses, even if the process that produces them is characterized by perturbations sharply peaked at a certain scale k.

[2] Not to be mistaken with the comoving scale defined with the sam symbol.

Collapse fraction

In order characterize the PBH population, an interesting quantity to define is the collapse fraction β, defined as the fraction of energy density of the Universe that collapses into a PBH at the time of formation

$$\beta \equiv \left.\frac{\rho_{\rm PBH}}{\rho_{\rm tot}}\right|_{\text{at formation}} = \left(\frac{H_0}{H_{form}}\right)^2 \left(\frac{a_{form}}{a_0}\right)^{-3} \Omega_{\rm CDM} f_{\rm PBH} \tag{3.52}$$

where we also introduced the density fraction of PBH that make up dark matter $f_{\rm PBH}$ measured at the present time

$$f_{\rm PBH} \equiv \frac{\Omega_{\rm PBH}}{\Omega_{\rm CDM}} \tag{3.53}$$

the collapse fraction can be computed as a function of $M_{\rm PBH}$ and reads [33]

$$\beta \simeq 3.7 \times 10^{-9} \left(\frac{\gamma}{0.2}\right)^{-1/2} \left(\frac{g_{*,\,\rm form}}{10.75}\right)^{1/4} \left(\frac{M_{\rm PBH}}{M_\odot}\right)^{1/2} f_{\rm PBH} \tag{3.54}$$

therefore, we can see that constraints on $f_{\rm PBH}$ translate on constraints on β.

The collapse fraction then can be linked to the statistical properties of the density perturbation, encoded in the power spectrum. In fact, the power spectrum, as long as the field is gaussian, uniquely determines the statistical properties of the field, and thus the probability $P(\delta)$ that a perturbation is over the threshold. Then the collapse fraction can be written as

$$\beta = \gamma \int_{\delta_{\rm th}}^{1} P(\delta) d\delta \tag{3.55}$$

which becomes, in the Press-Schechter formalism

$$\beta\left(M_{\rm PBH}\right) \approx \frac{\gamma}{\sqrt{2\pi}\nu_{\rm th}} \exp\left[-\frac{\nu_{\rm th}^2}{2}\right], \tag{3.56}$$

where we defined $\nu_{\rm th} \equiv \delta_{\rm th}/\sigma_{M_{\rm PBH}}$, as the normalized amplitude of the peak, and the variance $\sigma_{M_{\rm PBH}}$ of the power spectrum at the scale $R \simeq 1/a_{\rm form} H_{\rm form}$ is given by

$$\sigma^2_{M_{\rm PBH}} = \int d\ln k \mathcal{P}_\delta(k) W^2(kR) = \int d\ln k W^2(kR) \frac{16}{81} (kR)^4 \mathcal{P}_\zeta(k). \tag{3.57}$$

We stress that this result is approximate, but even in more refined calculations the final result is that the variance of the density field at a certain scale is related with the abundance of PBHs with a mass at roughly the corresponding horizon mass. Therefore, by applying constraints on $f_{\rm PBH}$ at a given mass scale, we can constrain $\mathcal{P}_\zeta(k)$ at the relevant scale [34, 27]. Vice-versa, if the power spectrum has a peak of at least $\mathcal{O}(10^{-2})$ at a given scale k, then we expect to find PBH at roughly the corresponding horizon mass. An example of the constraining power of PBHs on the power spectrum can be seen in figure 3.4, note the vast range of scales that PBHs can cover.

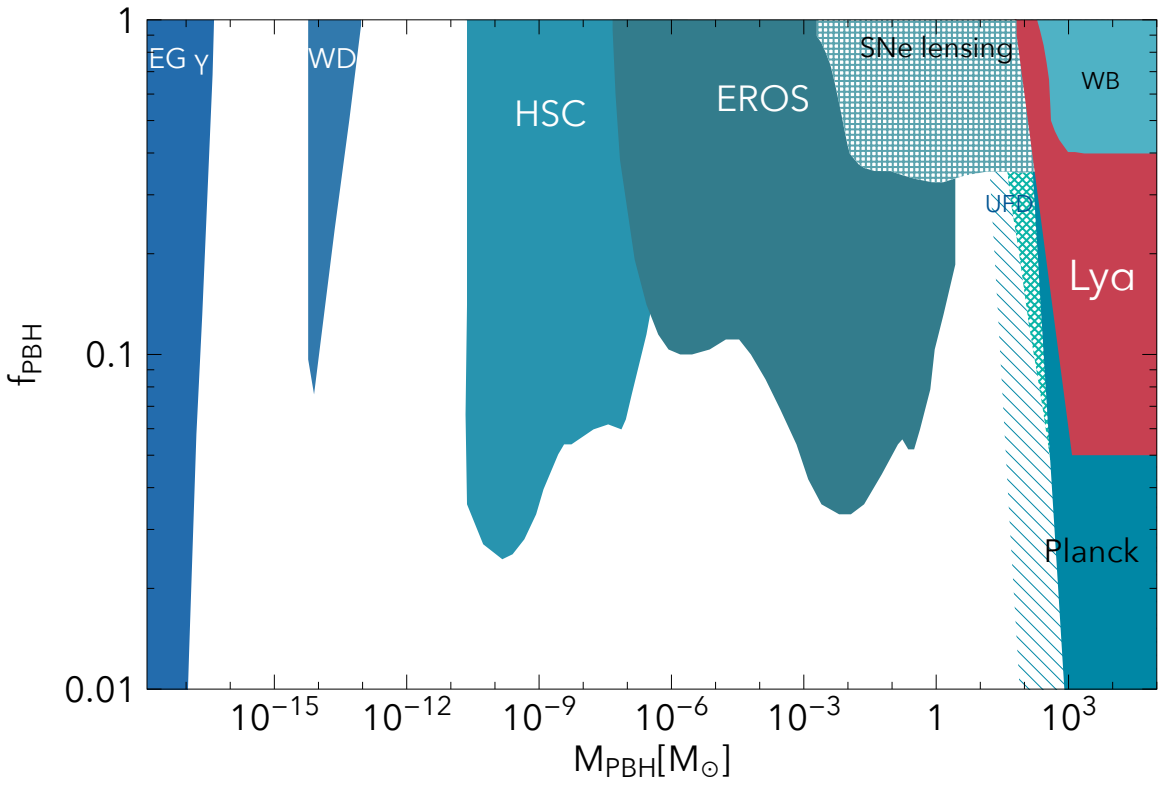

Figure 3.5: Current constraints on the PBH abundance $f_{\rm PBH}$, assuming a monochromatic mass distribution. Taken from [35].

3.2.2 PBH detection and constraints

While a detection of PBHs would be a groundbreaking physical discovery, at this time there are no confirmed observations. Of course, since all black holes differ one from each other only by their mass and angular momentum, telling apart PBHs and astrophysical black holes cannot in general be done with certainty. The only exception would be the discovery of sub solar mass BHs, as there is no viable astrophysical process that could produce them.

Sparked by LIGO detection of mergers of $\mathcal{O}(10M_\odot)$ black holes and by the ever increasing amount of data acquired by gravitational wave astronomy, much effort is being done to statistically discriminate populations of astrophysical BHs and PBHs from the data acquired from the mergers, for example by cross correlating them with other tracers [36, 37, 38], by measuring the eccentricities of the binaries [39], or by studying their mass functions [40].

Another way to operate is instead to constrain the PBH abundance $f_{\rm PBH}$ in a given mass range. In fact, if PBHs of a given mass would make up a fraction of the dark matter, they would produce measurable effects depending on the size of the black hole, and the lack of observations of those effects can be used to put upper bounds on their abundance. Some constraints that are currently being investigated are [34, 35]:

Gamma ray background (10^{15} g $\lesssim M_{\rm PBH} \lesssim 10^{17}$ g)**:** PBHs in this mass range are expected to be evaporating due to Hawking radiation, emitting high energy γ rays. The lack of a detection of this gamma ray background constrain the abundance of small mass black holes.

Microlensing (10^{26} g $\lesssim M_{\rm PBH} \lesssim 10^{34}$ g)**:** the lack of detection of microlensing by the EROS and MACHO surveys, designed to test the hypothesis of massive compact objects making up dark matter, has put an upper bound on the abundance of sub solar mass PBHs.

Lyman-α forest (10^{36} g $\lesssim M_{\rm PBH}$)**:** a statistical analysis of the Lyman-α forest, with the aid of

hydrodynamical simulations can put constraints on the abundance of $10^2 \sim 10^3 M_\odot$ PBHs.

a comprehensive visualization of constraints on $f_{\rm PBH}$ is shown in figure 3.5, for a monochromatic mass distribution, that is, all the PBHs are assumed to have the same mass. It should be noted that, in general, extended mass distributions suffer tighter constraints [41], because even if the peak of the distribution is in a constraint-free zone, the tail could touch a region where $f_{\rm PBH}$ is ruled out.

Chapter 4

Cosmological observables: 21 cm line

The observable on which our work focuses is the redshifted 21 cm signal, specifically its fluctuations encoded in the angular power spectrum C_ℓ^{21}. In order to extract information about the primordial universe from 21cm Intensity Mapping (IM) experiments we have to link the Primordial Power Spectrum (PPS) to such fluctuations. In this chapter we will review the physics of the 21 cm line, characterize the relevant quantities and the approximations and notation that will be used in our analysis.

More precisely, what is observed by 21cm experiments is the intensity of the redshifted 21cm radiation, either emitted or absorbed by the neutral hydrogen gas undergoing an hyperfine transition, with respect to the CMB. This quantity is encoded in the brightness temperature T_{21}, which is itself proportional to the contrast between the CMB temperature T_γ and the spin temperature T_s, determined from the number density of neutral hydrogen in the ground and excited state of the 21cm transition. In order to determine T_{21} and its fluctuations we have to understand how those quantities vary during the evolution of the Universe, both globally and locally.

4.1 Basic 21 cm physics

The 21 cm hydrogen line is due to the transition of neutral hydrogen in its ground state (HI) from triplet (parallel spins) to singlet (antiparallel spins). The transition has a rest frame frequency ν_0 of 1.4204 MHz, corresponding to a wavelenght of 21.106 cm. Since it's the most common atom in the universe, hydrogen makes a good tracer for the underline density field, and being able to map its density fluctuations would provide an enormous wealth of information.

As the light from the CMB passes through neutral hydrogen, its intensity at the frequency of

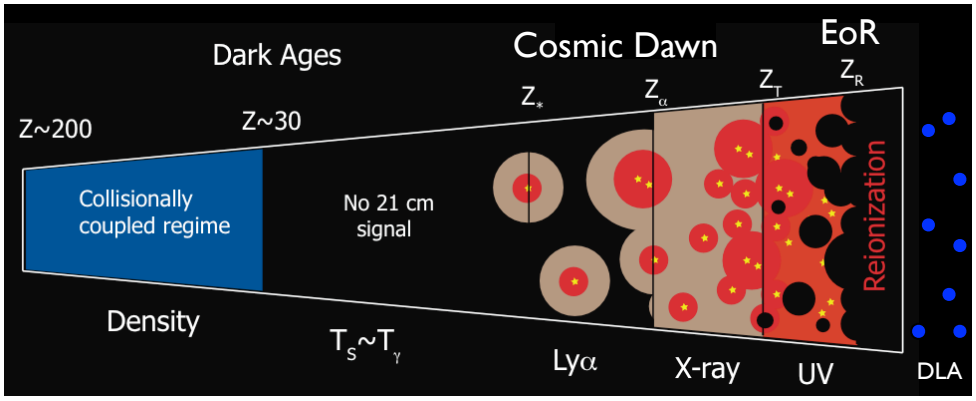

Figure 4.1: A schematic representation of the 21cm signal history. Taken from [42]

.

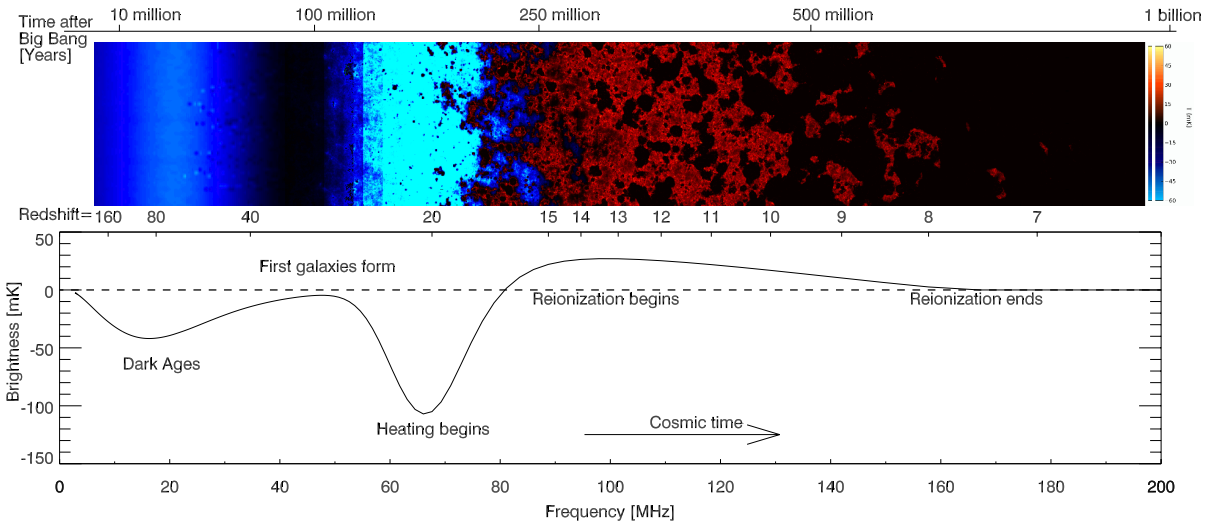

Figure 4.2: The expected history of 21cm signal, both fluctuations from a simulation (top) and sky averaged signal (bottom). Taken from [42]

.

the 21cm transition can get dimmed or enhanced depending on whether the spin temperature T_s, which is the excitation temperature of the of the gas with respect of the 21cm transition, is lower or greater than the temperature of the CMB T_γ. What we see then is a trough or a bump in the CMB blackbody spectrum, at a frequency corresponding to the redshifted 21cm frequency.

As we will see, the spin temperature is affected by three processes [42, 43]:

- absorption/emission of 21 cm photons from-to a background source, in our case the CMB
- collisions with other hydrogen atoms, with electrons and with protons
- resonant scattering of $Ly-\alpha$ photons that cause a spin flip via an intermediate excited state (Wouthuysen-Field effect [44, 45]) .

The first process will drive the spin temperature towards the CMB temperature T_γ, while the second will try to bring it towards the gas temperature T_k.

Therefore, T_s will be bounded between the two temperatures, and it is an essential requirement for the 21cm signal to be observed at a certain redshift that T_γ and T_k are different. This requirement sets the maximum redshift observable with 21cm experiments to about $z \sim 200$, before that the numerical density of free electrons in the cosmic medium was high enough to couple T_k and T_γ.

The cosmological region that can be probed by 21cm IM experiments is divided in qualitatively different stages depending on which processes come into play, affecting T_s. Here we give a qualitative summary of the various regimes:

Dark Ages ($30 \lesssim z \lesssim 200$) The first window for 21cm observations is the Dark Ages (DA), which happened between $z \sim 200$ and $z \sim 30$, when the free electrons in the cosmic medium ceased to efficiently couple the CMB radiation with the neutral hydrogen gas, which cooled adiabatically $T_k \propto (1+z)^2$, while $T_\gamma \propto 1+z$. Collisional coupling drove T_s towards $T_k < T_\gamma$, producing an absorption signal. Eventually the gas density dropped and radiative coupling prevailed over collisional coupling, setting $T_s \simeq T_\gamma$.

Cosmic Dawn ($12 \lesssim z \lesssim 25$) as the first stars light up they start emitting Ly-α photons and X-rays. Initially the emitted Lyman-α photons are not enough to significantly heat the gas and increase T_k, but are sufficient to couple T_s with T_k again, through the Wouthuysen-Field effect. Therefore another absorption signal that eventually might become an emission

signal is expected.

Epoch of Reionization ($6 \lesssim z \lesssim 11$) In this era the 21cm transition was again mediated by the Wouthuysen-Field effect. The radiation from the stars end up heating the gas and $T_k > T_\gamma$, giving an emission signal. Luminous objects eventually ionize the surrounding hydrogen, creating bubbles of darkness in the 21cm signal. Eventually all the IGM is ionized, thus marking the end of 21cm emission at $z \sim 6$, aside for small collapsed patches of neutral hydrogen (damped Lyα systems).

An example of the full history of 21cm signal is shown in figure 4.2.

While the Cosmic Dawn and the EoR are more accessible experimentally, their physics are strongly dependant of many assumptions of how reionization happened and how the first stars and galaxies evolved, and the dynamics are strongly nonlinear, making it much harder to model and thus extract cosmological information, since the (g)astrophysical and the cosmological physics are intertwined. Their treatment thus usually relies on simulations that aim to reproduce the evolution of the relevant quantities on hundred megaparsec wide comoving volumes using code such as 21cmFAST[1] [46, 47].

In this work we will then mainly focus on what information can be extracted the Dark Ages, where the dynamics are still well described by the linear approximation and much simpler physical modeling, not requiring to model the power spectrum induced by the ionized bubbles, allowing to more readily link the primordial fluctuations to the observed brightness fluctuations. Additionally, the scales over which 21cm fluctuations in the Dark Ages are damped is given by the Jeans scale $k_J \sim 300\,\mathrm{Mpc}^{-1}$, three orders of magnitude smaller than the Silk damping scale of $k_S \sim 0.2\,\mathrm{Mpc}^{-1}$ of CMB fluctuations.

4.1.1 Global evolution

Spin temperature

We first define the spin "temperature" T_s:

$$\frac{n_1}{n_0} = 3\exp\left(-\frac{T_\star}{T_s}\right) \approx 3\left(1 - \frac{T_\star}{T_s}\right) \tag{4.1}$$

which is the excitation temperature associated to the spin flip transition, quantifying the fraction of atoms in the excited (triplet) state and ground (singlet) state, respectively labeled as 1 and 0. The temperature $T_\star = h\nu_0/k_B = 0.068K$ is the transition energy in Kelvins, note that in all the astrophysical applications we have T_s, T_γ, $T_k\, T_\alpha \gg T_\star$, and we can take the appropriate limits.

The relative abundances n_0 and n_1 are related, at equilibrium, by the equation [48, 49]

$$n_0\left(C_{01} + R_{01} + L_{01}\right) = n_1\left(C_{10} + R_{10} + L_{10}\right) \quad \Rightarrow \quad 3\left(1 - \frac{T_\star}{T_s}\right) \approx \frac{C_{01} + R_{01} + L_{01}}{C_{10} + R_{10} + L_{10}} \tag{4.2}$$

where C_{ij}, L_{ij} and R_{ij} are, respectively, the collisional transition rates, the Lyman-α transition rates the radiative transition rates between the states i and j. This equation holds in the steady state approximation, i.e. when $C_{ij} + R_{ij} \gg H$, which is true at all times we are considering.

We then have to find expression for the transition rates, relating them with the thermodynamic quantities. The radiative transition rates are related by the equation

[1] `https://github.com/21cmfast/21cmFAST`

$$R_{01} = 3\exp\left(-\frac{T_\star}{T_\gamma}\right) R_{10} \approx 3\left(1 - \frac{T_\star}{T_\gamma}\right) R_{10} \tag{4.3}$$

in which R_{10} is given by

$$R_{10} = A_{10}\left(1 + \frac{1}{\mathrm{e}^{T_\star/T_\gamma} - 1}\right) \approx A_{10}\frac{T_\gamma}{T_\star} \tag{4.4}$$

with $A_{10} \simeq 2.85 \times 10^{-15} s^{-1}$ being the spontaneous decay rate of the 21cm transition.

The upward and downward transition rates are related by the equation

$$C_{01} = 3\exp\left(-\frac{T_\star}{T_k}\right) C_{10} \approx 3\left(1 - \frac{T_\star}{T_k}\right) C_{10} \tag{4.5}$$

an analogous equation holds for the Lyman-α transition, with the "light temperature" T_α whose details specified later:

$$L_{01} = 3\exp\left(-\frac{T_\star}{T_\alpha}\right) L_{10} \approx 3\left(1 - \frac{T_\star}{T_\alpha}\right) L_{10}. \tag{4.6}$$

Bringing equations (4.1), (4.2), (4.3), (4.5) and (4.4) together and solving for T_s we get the expression

$$\begin{aligned} T_s =& \frac{T_\star + T_\gamma(z) + y_k T_k(z) + y_\alpha T_\alpha}{1 + y_k + y_\alpha} \\ =& \frac{T_\star + T_\gamma(z) + y_k T_k(z)}{1 + y_k} \quad \text{(before star formation)} \end{aligned} \tag{4.7}$$

where y_k and y_α are the kinetic and Lyman-α coupling, respectively.

What equation (4.7) is saying is that the spin temperature is a weighted mean of the temperatures T_γ, T_k and T_α, and its value is determined by which coupling dominates at a given time.

The evolution of T_s during the Dark Ages, without any ionizing sources, obtained as an output of our code is shown in the top panel of figure 4.3. At higher redshifts the collisional term dominates and drives the spin temperature towards the gas temperature T_k, but as time passes, n_H decreases and the collisional coupling loses power with respect to the radiative coupling, and T_s is brought toward T_γ.

Optical depth and observed brightness temperature

The absorption or emission of 21cm photons by the neutral hydrogen clouds appear to us as a trough or a bump in the low frequency tail of the CMB blackbody spectrum.

We therefore have to quantify the variation in radiation intensity emitted at a certain redshift z with some quantity we can measure with our radio telescopes on Earth (or on the Moon) at $z = 0$.

As light passes through a medium, its intensity at a certain frequency ν along the line of sight is given by the radiative transfer equation for the specific intensity I_ν

$$\frac{\mathrm{d}I_\nu}{\mathrm{d}s} = -\alpha_\nu I_\nu + j_\nu \tag{4.8}$$

where the coefficients α_ν and j_ν represent absorption and emission, respectively.

Since the 21cm frequency is always much smaller than the peak of the CMB blackbody spectrum we can safely work in the Rayleigh-Jeans limit and relate such intensity with a characteristic temperature

$$I_\nu = 2k_B T\nu^2/c^2 \tag{4.9}$$

introducing the optical depth $\tau = \int \alpha(s)ds$ will allow us to rewrite equation (4.8) in a more convenient way, as the temperature observed after the light of a background source with temperature T_γ passes through a cloud with uniform excitation temperature, in our case T_s [42, 50]

$$T_b = T_s\left(1 - e^{-\tau_\nu}\right) + T_\gamma(\nu)e^{-\tau_\nu} \tag{4.10}$$

the variable that we will focus on, T_{21}, is conventionally defined as the *difference* of this quantity with respect to the source

$$T_{21} \equiv T_b - T_\gamma = (T_s - T_\gamma)\left(1 - e^{-\tau_\nu}\right) \tag{4.11}$$

the optical depth at the 21cm transition frequency is

$$\tau_\nu = \int \mathrm{d}s \left[1 - \exp\left(\frac{-T_\star}{T_s}\right)\right] \sigma_0\phi(\nu)n_0 \tag{4.12}$$

where $n_0 = n_H/4$, $\sigma_0\phi(\nu)$ denotes the 21cm cross section with $\sigma_0 = 3c^2A_{10}/8\pi\nu^2$ and $\int \phi(\nu)d\nu = 1$. This expression can be computed in the Sobolev approximation [51, 42], giving

$$\tau_{\nu_0} = \frac{3c^3\hbar A_{10}x_{HI}n_H}{16k_B T_s\nu_0^2}\frac{1}{H(z) + (1+z)\partial_r v_r} \tag{4.13}$$

where x_{HI} is the neutral fraction of hydrogen, $\partial_r v_r$ is the comoving peculiar velocity gradient along the line of sight. While this term is similar to a redshift space distortion (RSD) term, it has a different origin. RSDs are due to our inability to discriminate between the redshifting of incoming radiation due to the Hubble flow and the peculiar velocity of the emitting source: since we compute distances by measuring the redshift of incoming radiation a source with a peculiar velocity with a longitudinal component toward us would appear to be closer in redshift space than it is in real space, vice-versa, a source with an outward peculiar velocity would appear to be farther than it is in real space. In formulas, the redshift space coordinate s and the real space comoving coordinate **r** are related by:

$$\mathrm{s} = \mathrm{r} + \frac{(1+z_{\mathrm{obs}})}{H\left(z_{\mathrm{obs}}\right)}v_\parallel(t,\mathrm{r})\hat{r}. \tag{4.14}$$

This effect, combined with the physics of gravitational collapse, produces distortions in the shape of the large scale structures, such as the Kaiser effect, a squeezing along the line of sight at large scales, and the Finger of God, an elongation along the line of sight at smaller scales. RSDs also affect the 21cm three dimensional power spectrum, which becomes anisotropic, and can be decomposed in terms depending on powers of μ, the angle between the line of sight and the Fourier mode **k**. The μ-dependency of the power spectrum can be used to discriminate the purely cosmological component of the power spectrum [3, 43].

However, the $\partial_r v_r$ term in equation (4.13) does not, in principle, require any observer, and would arise even if RSDs would be taken into account [49, 52]. We will not consider RSDs in this work, however we will include the velocity gradient term.

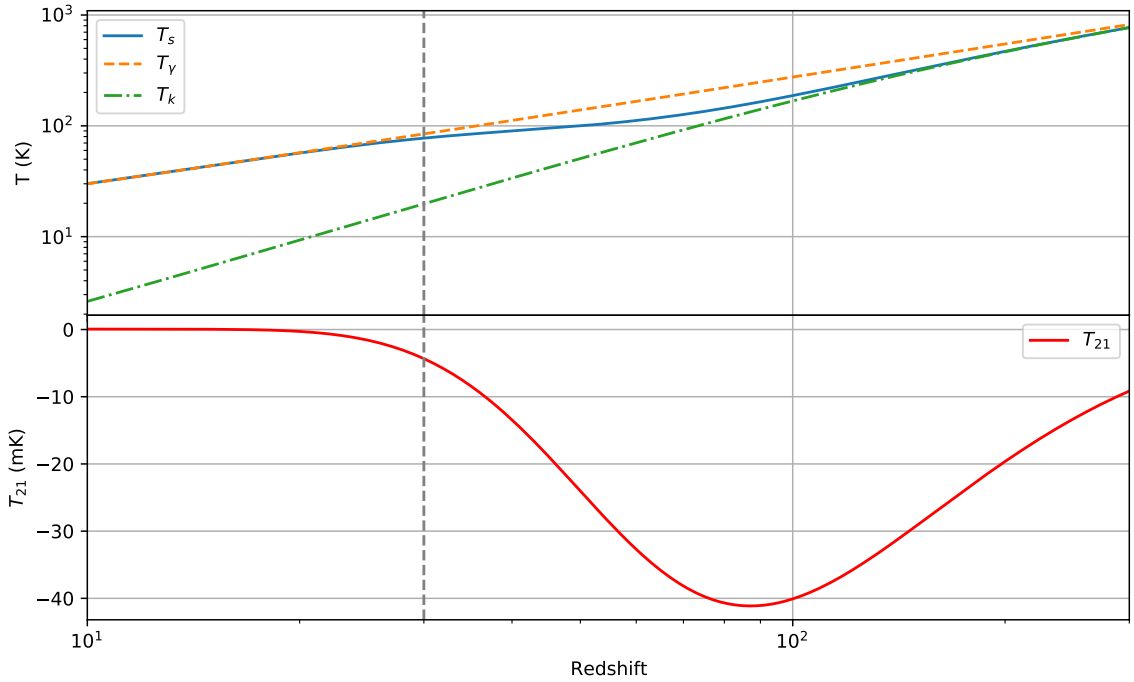

Figure 4.3: Global thermal history of the IGM without star formation. Top panel: evolution of T_γ, T_k and T_s. Bottom panel: mean brightness temperature. The grey dashed lines at $z = 30$ marks the approximate end of the Dark Ages.

The redshifted 21cm temperature observed at $z = 0$ is then, in the optically thin limit $\tau \ll 1$, which is always the case for 21cm photons [50, 42, 3]

$$\begin{aligned} T_{21}^{\text{obs}} &= \frac{T_{21}^{\text{loc}}}{1+z} = \frac{T_s(z) - T_\gamma(z)}{1+z}\left(1 - e^{-\tau_{\nu_0}}\right) \approx \frac{T_s(z) - T_\gamma(z)}{1+z}\tau_{\nu_0} \\ &= \frac{T_s(z) - T_\gamma(z)}{1+z}\frac{3c^3\hbar A_{10} x_{HI} n_H}{16 k_B T_s(z) \nu_0^2}\frac{1}{H(z) + (1+z)\partial_r v_r} \\ &= \frac{1}{1+z}\left(1 - \frac{T_\gamma}{T_s}\right)\frac{3c^3\hbar A_{10} x_{HI} n_H}{16 k_B \nu_0^2}\frac{1}{H(z) + (1+z)\partial_r v_r} \end{aligned} \tag{4.15}$$

recalling the expression that we found for T_s, equation (4.7), we get that the brightness temperature depends on the following variables:

- the CMB temperature T_γ
- the gas temperature T_k through the collisional coupling y_k
- the hydrogen fraction n_H both directly and through the coupling y_k
- the neutral hydrogen fraction x_{HI}
- the velocity gradient along the line of sight $\partial_r v_r$

while we omitted the spatial and redshift dependence for clarity, each of those variables varies in space and time and can potentially source fluctuations of T_{21}^{obs}. From now on we will drop the "obs" superscript and just refer to the brightness temperature observed as $z = 0$ as T_{21}.

The average brightness temperature $\overline{T}_{21}(z)$ is then taken by taking the spatial averages of all the local quantities

$$\overline{T}_{21}(z) = \frac{3c^3\hbar A_{10}\overline{x}_{HI}\overline{n}_H}{16 k_B \nu_0^2}\frac{1}{H(z)(1+z)}\left(1 - \frac{\overline{T}_\gamma(z)}{\overline{T}_s(z)}\right) \tag{4.16}$$

its value four our fiducial model is plotted in the bottom panel of figure 4.3.

We note that the 21cm global signal is also subject of study, and there have been claims of a detection by the experiment EDGES of an absorption feature at $z \sim 17$ [53], despite it being anomalous in shape and amplitude if compared to the theoretical predictions of the signal at that redshift. The absorption signal at that redshift is due to the Lyman-α coupling of the spin temperature with the gas temperature (Wouthuysen-Field effect) mediated by the photons of the first stars. We however do not treat that process as we focus on the Dark Ages, before star formation begins.

4.2 Phenomenology of the 21cm signal

A convenient way to write equation (4.15) is [42]

$$T_{21} \approx (27\text{mK})\,(1+\delta_b)\,x_{\text{HI}}\left(1-\frac{T_\gamma}{T_s}\right)\left(\frac{\Omega_b h^2}{0.023}\right)\left(\frac{1+z}{10}\frac{0.15}{\Omega_m h^2}\right)^{1/2}\frac{1}{1+\frac{(1+z)}{H(z)}\partial_r v_r} \tag{4.17}$$

4.2.1 Couplings

In the previous section we saw that the spin temperature is determined by which coupling dominated over the other during the various stage of the evolution of the IGM.

Collisional Coupling

The collisional coupling y_k brings the spin temperature toward the kinetic temperature of the HI gas. Its expression is

$$y_k = \frac{T_\star}{A_{10}T_k}\left(C_H + C_e + C_p\right) \tag{4.18}$$

where the coefficients C_i's are the de-excitation rates of the triplet state due to collisions with neutral hydrogen, free electrons and free protons, respectively. In the Dark Ages only relevant coefficient is C_H [54], whose value can be found in [55], as the other are proportional to $1 - x_H$ and thus suppressed by a factor 10^{-4}

$$C_H = 3.1 \cdot n_H \cdot 10^{-11} \cdot T_k^{0.357} \exp\left(\frac{-32}{T_k}\right) \text{cm}^3\ \text{s}^{-1} \tag{4.19}$$

Lyman-α coupling

The coupling with the Lyman-α photons is described by the Wouthusyen-Field effect: this process entails the transition from one hyperfine state of HI to the other, mediated by the excitation to a higher energy state, such as the $2p$ level

the coupling y_α is

$$y_\alpha = \frac{16\pi^2 T_\star e^2 f_{12}\tilde{J}_0}{27A_{10}T_k m_e c} \tag{4.20}$$

depending on the constant f_{12}, the Ly-α oscillator strength, and the Ly-α photon intensity $\tilde{J}_0$

$$\tilde{J}_0 = \frac{\phi_\alpha c}{4\pi H(z)\nu_\alpha} n_H x_H \int_{E_0}^{\infty} \sigma(E)\mathcal{N}(E)dE \tag{4.21}$$

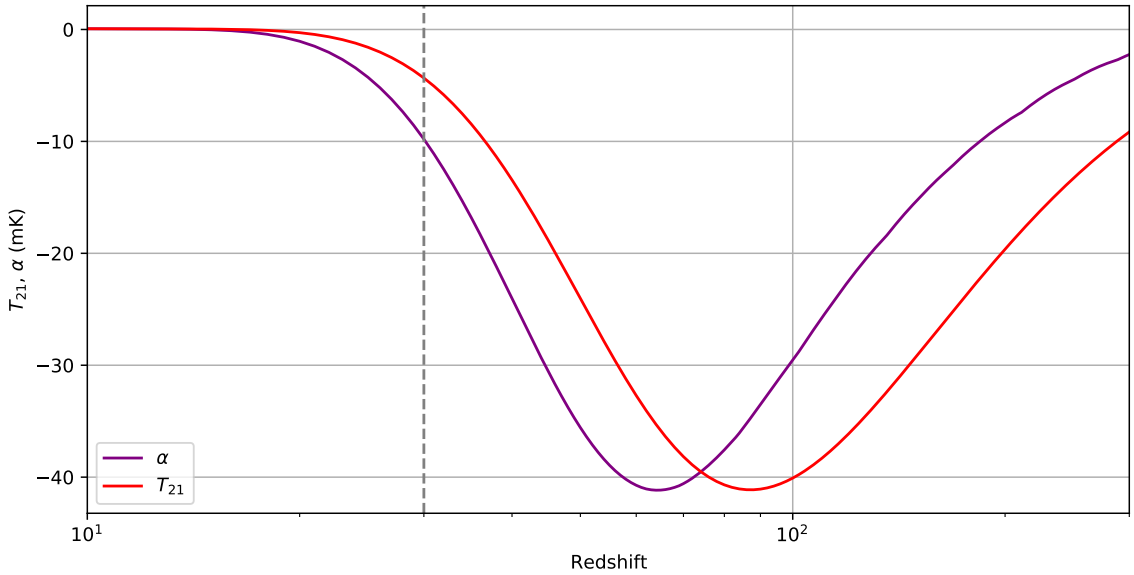

Figure 4.4: Average brightness temperature $\overline{T}_{21}$ and α parameter. The grey dashed line marks the end of the Dark Ages at $z = 30$.

as we anticipated this coupling is negligible in the Dark Ages since there isn't any object capable of producing energetic photons. However this may not be the case in non standard scenarios, for example if Primordial Black Holes have formed in the early universe and heated matter in their accretion disks [7] or in the case of dark matter annihilation [6].

4.3 Perturbative expansion of T_{21} fluctuations in the Dark Ages

In this section we will connect the 21cm fluctuations to the physical quantities we want to study i.e. the Primordial Power Spectrum.

Equation (4.15) shows that the brightness depends of many quantities that could spatially fluctuate, leading to fluctuations of the observed T_{21}.

The next step in order to perform our analysis is to relate those fluctuations with the matter power spectrum $P_m(k)$.

We note that while in the later dark ages, $z \leq 50$ non-linear corrections in the evolution of the perturbations become important [54], at all times during this cosmic eras the overdensity field is well below unity, allowing to compute the T_{21} power spectrum with a perturbative treatment.

We then can obtain a perturbative expansion of T_{21} in powers of the fluctuation of the relevant quantities. In our treatment we do not consider fluctuations of x_{HI} and T_γ, as they are negligible in the regime of interest to us, as the former therm is $1 - x_e$ with $x_e \simeq 10^{-4}$, while the latter is of a few μK compared to fluctuations of T_{21} in the mK range, a thousand times larger.

We then split T_k and n_H in a mean term and a spatial dependent fluctuation, as usual

$$T_k(z, \boldsymbol{x}) \equiv \overline{T}_k(z)(1 + \delta_{T_k}(z, \boldsymbol{x})) \tag{4.22}$$

$$n_H(z, \boldsymbol{x}) \equiv \overline{n}_H(z)(1 + \delta_H(z, \boldsymbol{x})) \tag{4.23}$$

we also define the dimensionless relative velocity fluctuation term as

$$\delta_v(z, \boldsymbol{x}) \equiv -(1+z)\frac{\partial_r v_r}{H(z)} \tag{4.24}$$

this procedure leads to the second order expansion of T_{21} in terms of the aforementioned fluctuations

$$\begin{aligned} T_{21} =& \overline{T}_{21}\left(1+\delta_v+\delta_v^2\right) + \left(\mathcal{T}_b\delta_b + \mathcal{T}_T\delta_{T_\mathrm{k}}\right)(1+\delta_v) \\ &+ \mathcal{T}_{bb}\delta_b^2 + \mathcal{T}_{bT}\delta_b\delta_{T_\mathrm{k}} + \mathcal{T}_{TT}\delta_{T_\mathrm{k}}^2 \end{aligned} \tag{4.25}$$

Where we have omitted the $\mathbf{x}$ dependence for clarity. Restricting ourselves only to linear fluctuations we have:

$$T_{21} = \overline{T}_{21}(1+\delta_v) + \mathcal{T}_b\delta_b + \mathcal{T}_T\delta_{T_\mathrm{k}} \tag{4.26}$$

where $\overline{T}_{21}$ and the $\mathcal{T}$ coefficient only depend on z and we took the approximation $\delta_b = \delta_H$, valid up to negligible corrections.

In order to find the evolution of the gas temperature we apply the first law of thermodynamics. Neglecting gravitational potentials we obtain

$$\dot{\delta}_{T_\mathrm{k}} - \frac{2}{3}\dot{\delta}_b\frac{1+\delta_{T_\mathrm{k}}}{1+\delta_b} = \Gamma_\mathrm{C}\left[\frac{\overline{T}_\mathrm{cmb}-\overline{T}_\mathrm{k}}{\overline{T}_\mathrm{k}}\delta_{x_e} - \left(\frac{\overline{T}_\mathrm{cmb}}{\overline{T}_\mathrm{k}}+\delta_{x_e}\right)\delta_{T_\mathrm{k}}\right] \tag{4.27}$$

where we have defined the rate Γ_C

$$\Gamma_\mathrm{C} \equiv \frac{8\sigma_\mathrm{T}a_r T_\mathrm{cmb}^4}{3\left(1+x_\mathrm{He}+x_e\right)m_e}\bar{x}_e \simeq \frac{8\sigma_\mathrm{T}a_r T_\mathrm{cmb}^4}{3m_e}\bar{x}_e. \tag{4.28}$$

Equation (4.27) should be coupled with an equation for δ_{x_e}, but to simplify the system the fluctuations in the free electron density can be neglected, giving an error of about 10%, as found in [4].

With those simplifying assumptions the equation for the gas temperature evolution at the linear order is

$$\dot{\delta}_{T_\mathrm{k}}^{(1)} + \frac{\overline{T}_\mathrm{cmb}}{\overline{T}_\mathrm{k}}\Gamma_\mathrm{C}\delta_{T_\mathrm{k}}^{(1)} = \frac{2}{3}\dot{\delta}_b^{(1)}. \tag{4.29}$$

This equation can be solved assuming $\delta_b^{(1)}(\boldsymbol{x}, z) \propto a$ and with the aid of a recombination code such as HYREC [56, 57], to find a coefficient $C_1(z)$ such that

$$\delta_{T_\mathrm{k}}(\boldsymbol{x}, z) = C_1(z)\delta_b(\boldsymbol{x}, z). \tag{4.30}$$

Plugging this relation back in (4.26) we get the first order expansion of the spatial fluctuations of T_{21} during the Dark Ages in terms of δ_b and δ_v:

$$\delta T_{21}(\boldsymbol{x}) = \alpha(z)\delta_b(\boldsymbol{x}) + \overline{T}_{21}(z)\delta_v(\boldsymbol{x}) \tag{4.31}$$

with $\alpha(z) = \mathcal{T}_b(z) + C_1(z)\mathcal{T}_T(z)$ a parameter depending only on z. The average brightness temperature and the parameter $\alpha(z)$ are shown in figure 4.4.

Angular power spectrum

When observing the sky at a given redshift z with a telescope we are effectively looking a portion of a spherical shell of a 3-dimensional volume, projected along the line of sight. That is, while the information of the fluctuations of a random field describing some physical quantity is encoded in the n-point correlation functions $\xi^{(n)}(\boldsymbol{x_1}...\boldsymbol{x_n})$ or alternatively the related Fourier transforms i.e. the power spectrum $P(k)$, the bispectrum etc, the data we gather is more conveniently described by the angular fluctuations of the field.

This is especially the case for the CMB, since recombination happened in a very short time compared to cosmological scales and the CMB radiation that we see is all emitted at around $z = 1100$. However the same formalism can be adapted for the 21cm line. In this case we are able to probe a much greater volume and divide it in concentric spherical shells, effectively performing a tomography of the observable region.

We first recall the expression for the spherical harmonics decomposition of a generic field $\Phi(\hat{n})$ defined on a spherical surface

$$\Phi(\hat{n}) = \sum_{\ell=0}^{\infty} \sum_{m=-\ell}^{\ell} a_{\ell m} Y_{\ell m}(\hat{n}) \tag{4.32}$$

where the $a_{\ell m}$ are the coefficients of the expansion, analogous to the Fourier transform of a field defined in 3D space, and $Y_{\ell m}$ are the spherical harmonics, forming an orthonormal basis. The ℓ index determines the angular scale $\theta \sim \ell^{-1}$, while the m index specifies the directional dependence.

The angular power spectrum C_ℓ is then defined as the variance of the $a_{\ell m}$ coefficients

$$\langle a_{\ell m} a^*_{\ell' m'} \rangle = \delta_{\ell \ell'} \delta_{m m'} C_\ell \tag{4.33}$$

or, alternatively

$$C_\ell = \frac{1}{2\ell + 1} \sum_{m=-\ell}^{\ell} |a_{\ell m}|^2 \tag{4.34}$$

In order to compute the angular power spectrum of 21cm fluctuations we switch to Fourier space. Under the assumption of matter domination and that baryons follow the DM distribution we have the relation

$$\delta_v(\mathbf{k}, z) = (\hat{k} \cdot \hat{n})^2 \delta_b(\mathbf{k}, z) \tag{4.35}$$

we can therefore define the 21cm transfer function $\mathcal{T}_\ell(k, \nu)$

$$\mathcal{T}_\ell(k, \nu) = \int_0^\infty dx W_\nu(x) \left[\alpha(z) j_\ell(kx) + \overline{T}_{21}(z) J_\ell(kx) \right] \tag{4.36}$$

where $j_\ell(kx)$ are spherical Bessel functions and we defined the term $J_\ell(kx)$ which can be written as a combination of spherical Bessel functions [58]

$$\begin{aligned} J_\ell(kx) &\equiv -\partial^2 j_\ell(kx)/(\partial kx)^2 \\ &= \left[-\frac{\ell(\ell-1)}{4\ell^2 - 1} j_{\ell-2}(kx) + \frac{2\left(3\ell^2 + 3\ell - 2\right)}{4\ell^2 + 4\ell - 3} j_\ell(kx) - \frac{(\ell+2)(\ell+1)}{(2l+1)(2\ell+3)} j_{\ell+2}(kx) \right]. \end{aligned} \tag{4.37}$$

$W_\nu(x)$ is a window function centered on the comoving distance from which the incoming radiation is redshifted to the frequency ν, depending on the details of the experiment. It is due to the finite bandwidth of the experimental apparatus. We give more details about this in chapter 5.

Finally, the angular power spectrum C_ℓ^{21} of 21cm fluctuations in term of the matter power spectrum can be written as

$$C_\ell^{21}(\nu) = \frac{2}{\pi}\int_0^\infty k^2 dk P_m(k, z(\nu))\mathcal{T}_\ell^2(k,\nu). \tag{4.38}$$

We stress that the only dependency on the primordial parameters is in the matter power spectrum $P_m(k)$, which itself is dependant on the primordial power spectrum $\mathcal{P}_\zeta(k)$.

Chapter 5

Intensity mapping

We have now characterized the angular power spectrum of the fluctuations of the 21 cm signal that we expect to measure.

We remind that this radiation is emitted by the IGM as the neutral hydrogen atoms undergo a spin flip transition. 21 cm radiation from high redshift is therefore a faint and diffuse source of radio waves, and measuring its distribution in the sky in order to compute the angular power spectrum is a challenging task task. This is particularly true in the case of the 21cm radiation emitted in the Dark Ages, as its frequency is such that it's mostly shielded by the Earth atmosphere, and in order to detect it it might be necessary to move on the far side of the Moon.

This is the kind of task that the field of Intensity Mapping (IM) is trying to tackle. IM is a new and rapidly expanding field that consists in surveying the sky by mapping the integrated emission of light of a specific spectral line of a certain element from diffuse and unresolved sources, instead of detecting point-like resolved sources, as in galaxy surveys. While most of the effort in this field has been directed toward the detection of 21 cm emission from the IGM, there are also experiments in development that aim to study different spectral lines [2], such as the CO rotational transitions, the CII fine structure line and the Ly-α line. Effort is also being made towards the possibility of cross correlating the information from various lines [59], as well as with different cosmological probes, such as gravitational waves observations [38].

In order to compute the 21 cm power spectrum we need to be able to resolve the scales that characterize the fluctuations in T_{21}. Due to diffraction, the smallest angular scale than an optical system can resolve is given by $\theta \approx \lambda/D$, where D is the aperture of the system and λ is the wavelength of the electromagnetic radiation. This gives the requirement of a 42 km aperture for a resolution of 1 arcsecond with $\lambda = 21$ cm, far too big for a single telescope.

However, it is possible to use an array of multiple radio telescopes in order to create an instrument capable of reaching far smaller angular resolutions: this technique is called radio interferometry.

In this chapter we will introduce the topic of radio interferometry, which is the tool that will let us perform the tomographic analysis of the 21 cm signal in the future, in order compute its power spectrum, and we will characterize the specifications of the instruments that are relevant in order to gauge the detectability of the signal.

5.1 Interferometry basics

A radio interferometer is an array of multiple radio antennas, set to operate as a unique instrument, in order to obtain images of the sky with high angular resolution. It does so by measuring the interference pattern of the signal emitted by sources far away, which arrives with different phases to different antennas.

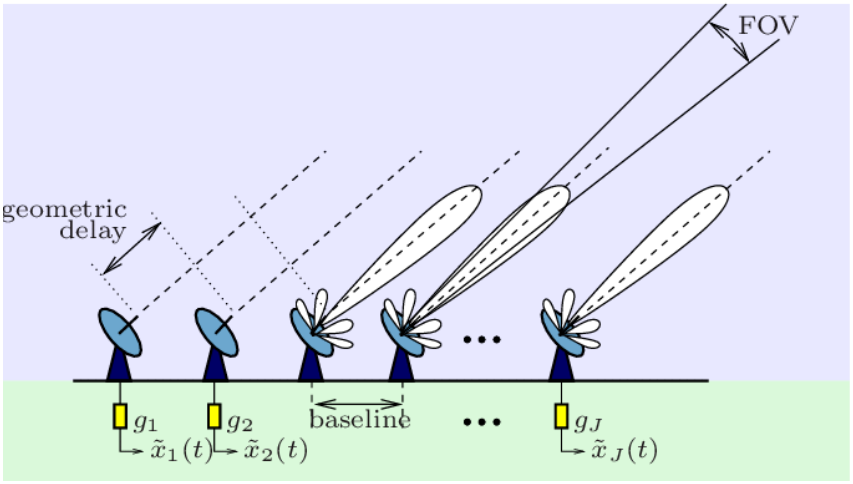

Figure 5.1: Schematic representation of a radio interferometer. Taken from [60].

The antennas can have various design, from dishes as in SKAO-MID to electric dipoles as in SKAO-LOW, LOFAR and the proposed Fast Fourier Transform Telescope [61].

The vector between a pair of each of the antennas that make up the apparatus is called a baseline and is indicated with $\mathbf{b}$. In an interferometer, each antenna samples the EM field coming from the sky from a given direction $\hat{\mathbf{n}}$.

The electric field induces a time varying voltage in the antenna, proportional to field itself. For each baseline, i.e. each couple of antennas, the signal is then multiplied and time averaged in a correlator order to extract a response R_c dependent of the signal intensity E^2 and the phase difference $\Delta\phi$ due to the geometric delay, given by

$$R_c \approx E^2 \cos(\Delta\phi) \tag{5.1}$$

with

$$\Delta\phi = 2\pi \frac{\mathbf{b}\cdot\hat{\mathbf{n}}}{\lambda} = 2\pi \mathbf{u}\cdot\hat{\mathbf{n}} \tag{5.2}$$

where we have introduced the vector $\mathbf{u} = (u, v)$, which is the baseline in units of the wavelength of the incoming radiation. This is actually only the even part of the contribution to the fringe pattern from the sky brightness at a given direction indicated by $\hat{\mathbf{n}}$. The odd, sin-like contribution can be obtained from the same procedure, but after adding a $\pi/2$ phase shift to the waves of one of the antennas constituting the baseline.

By integrating over the solid angular size spanned by the source we obtain the response of an interferometric apparatus to the signal coming from the sky, described by the visibility function $V(\mathbf{u})$, which is related to the sky brightness through the Van Cittert–Zernike theorem

$$V(\mathbf{u}) = \int e^{2i\pi(ul+vm)} \overline{T}(l,m) \mathrm{d}l\mathrm{d}m \tag{5.3}$$

where $\overline{T}(l,m)$ describes the sky brightness distribution as a function of the coordinates (l,m) of the plane tangent to the sky, filtered by the antenna primary beam response $A(l,m)$: $\overline{T}(l,m) = T(l,m)A(l,m)$. We can see that the visibility function is essentially the 2-dimensional Fourier transform of the sky brightness, at least for a small field of view where the flat sky approximation holds, with a single visibility being roughly a given Fourier mode of the sky brightness. In other

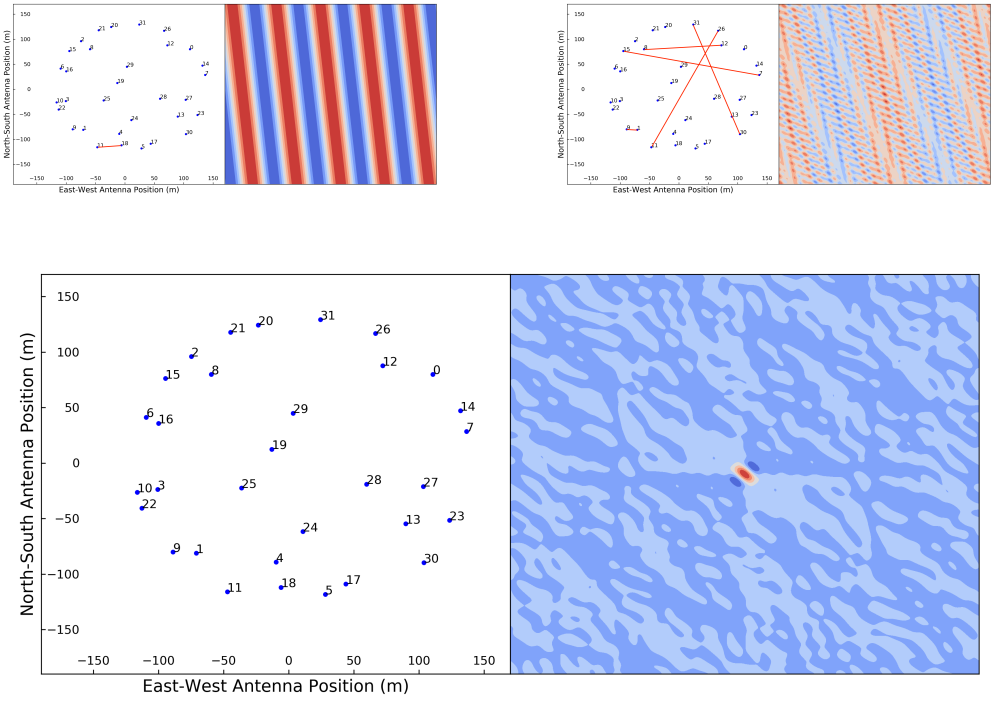

Figure 5.2: Example of the PSF of an interferometric array. Top left: the PSF of a single baseline is a sinusoidal pattern. Top right: as more baselines are added, the PSF shows a more complex fringe pattern. Bottom: with all the baselines the PSF acquires a more defined shape, peaked at the center. Taken from [63].

words, interferometers directly probe the power spectrum (the amplitude of the Fourier modes) of an astronomical patch they are pointed to.

Since we have only a finite number N of antennas, we can only have a finite number of baselines $N(N-1)/2$, meaning we can only sample $V(\mathbf{u})$ for a finite number of vectors $\mathbf{u}$, resulting in an incomplete coverage of the sky in Fourier space. In order to increase the coverage in the Fourier plane the antennas can be moved, and the rotation of the Earth is exploited as well [62].

By combining the measurements of the visibilities obtained from all the antennas constituting the apparatus and the rotation of the Earth one can then invert the relation (5.3) in order to obtain the sky brightness

$$\overline{I}_D(l,m) = \int S(u,v)V(u,v)e^{2\pi i(ul+vm)}dudv \tag{5.4}$$

where the function $S(u,v)$ describes the incomplete Fourier coverage in the (u,v) plane. The subscript D in $\overline{I}_D$ indicates that the resulting sky brightness obtained with this procedure is not a faithful representation of the sky brightness, but it's a "dirty image", i.e. it's the actual sky brightness convolved with the Point Spread Function of the instrument, which is the response of the interferometric array to a point source:

$$\overline{I}_D(l,m) = \tilde{SV} = PSF(l,m) * \overline{I}(l,m). \tag{5.5}$$

The PSF is a sinusoidal pattern if only one baseline is present, and it approaches a gaussian shape as multiple baselines are added, and the Earth rotation is exploited in order to obtain multiple baselines from the same configuration of the interferometer. An example of the evolution of the PSF as more baselines are added is shown in figure 5.2.

The above formalism describes the angular dependence of the sky brightness in a spherical shell of fixed z, equivalent to observing the 21 cm radiation at a given frequency ν. However, the strength of 21 cm IM is that it allows to probe the entire three dimensional cosmological volume in which the 21 cm brightness temperature is different from 0, allowing also to probe fluctuations along the line of sight by looking at the brightness also as a function of frequency. Therefore, when characterizing an interferometer, it is useful to consider the characteristic scales that an interferometer apparatus can resolve, both in the plane perpendicular to the line of sight and in the direction parallel to it, denoted respectively by the comoving wavenumber $k_\perp$ and $k_\parallel$. The wavenumbers are related to the specifications of the instruments and the cosmological parameters [64]:

$$\mathrm{k}_\perp = \frac{2\pi\nu_0 \mathbf{b}}{cD_c}; \quad k_\parallel = \frac{2\pi\nu_{21}H_0E(z)}{c(1+z)^2}\eta \tag{5.6}$$

where η is the Fourier dual of ν and D_c is the comoving radial distance

$$D_c \equiv \frac{c}{H_0}\int_0^z \frac{dz'}{E\,(z')}; \quad E(z) \equiv \sqrt{\Omega_m(1+z)^3+\Omega_\Lambda}. \tag{5.7}$$

Here we summarize some basic specifications of an interferometer:

Angular resolution: it's the smallest angular scale that can be resolved by the instrument. It's given by the maximum baseline of the instrument as

$$\theta_{min} = \lambda/D_{max} = \lambda_0(1+z)/D_{max} \tag{5.8}$$

with λ being the wavelength of the observed signal and $\lambda_0 = 0.21$ m in the case of the redshifted 21 cm signal. Alternatively, we are interested in the maximum multipole observable in the spherical harmonics decomposition of the sky, which is $\ell_{\max}(\lambda) = 2\pi D_{\max}/\lambda$.

Bandwidth $\Delta\nu$: the frequency range at which the observation is performed. This corresponds to observing a spherical shell of the IGM of finite depth.

Spectral resolution: the resolution in frequency of the instrument, determining the smallest scale that can be resolved along the line of sight.

Sensitivity: the thermal noise experienced by the instrument:

$$S_{rms} \approx \frac{SEFD}{\sqrt{N(N-1)t_{int}\Delta\nu}} \tag{5.9}$$

where $SEFD$ is the system equivalent flux density measured in janskys (Jy), proportional to the system temperature $T_{\rm sys}$ and inversely proportional to the effective area of the instrument A_{eff}, t_{int} is the total integration time.

Field of view: the solid angle of the sky covered by the instrument. It's given by the size of the beam of a single antenna.

5.2 21 cm interferometric experiments

Due to the enormous experimental challenges in mapping 21 cm fluctuations, currently no measurement of the 21 cm power spectrum has been made. The main problems are the foregrounds, which in the case of 21 cm radiation are 5 orders of magnitude or greater [64] compared to the signal, and the instrumental noise, limiting the sensitivity of the experiments. Additionally, while 21 cm radiation from the Epoch of Reionization can be detected by ground based experiments, the Earth ionosphere shields low frequency radiation, preventing us from seeing 21

cm radiation coming from the Dark Ages. A review of the state of the art of 21 cm intensity mapping experiments and techniques is given in [64].

5.2.1 Foregrounds

Foregrounds are due to the contamination of the 21 cm spectrum by astrophysical sources. The main source of foregrounds is the galactic synchrotron emission produced by the Milky Way, emitted by cosmic ray electrons propagating in interstellar magnetic fields. This emission has a temperature of hundreds of kelvins, and swamps the 21 cm signal we aim to observe. Additionally, it becomes brighter at lower frequencies, making it increasingly difficult to measure the 21 cm signal at lower redshifts:

$$T_{\text{sync}} = 180 \text{ K} \times \left(\frac{\nu}{180\text{MHz}}\right)^{-2.8} \tag{5.10}$$

There are also other sources of foreground contamination, such as free-free emission, bright radio point sources, and unresolved point sources. While those sources are dimmer than the galactic synchrotron emission, they still can dwarf the 21 cm signal and must be dealt with in order to achieve the observation of the cosmological signal.

One could in principle model the foreground contaminants and subtract them from the measured signal, but this approach in made prohibitive by the $\gtrsim 5$ orders of magnitude difference in foreground brightness compared to the 21 cm signal: even a small error in foreground estimation would bias the measured signal. However, unlike global signal measurements, experiments which measure spatial fluctuations can exploit the different spectral properties of foregrounds and cosmological signal in order to separate the contaminants and it can also be possible to avoid them altogether.

Foregrounds are in fact expected to have a relatively smooth spectrum in the frequency domain, and it can be shown that they lie in a wedge in the $(k_\perp, k_\parallel)$, as shown in figure 5.3. Further effects due to the imperfect experimental setup, such as calibration errors, can induce a leakage in the foregrounds Fourier modes outside the wedge, and to contrast this the Fourier space dedicated to the cosmological measurements is further reduced by introducing a buffer region.

Alternatively, one can exploit the fact that changing the observation frequency ν effectively samples different, uncorrelated volumes of the 21 cm three dimensional field, and exploit the cross frequency power spectrum to isolate the foreground components which are instead correlated, as shown in [17].

5.2.2 Instrumental sensitivity

The sensitivity of an interferometer determines its ability to detect the signal over the noise, mainly due to the thermal fluctuations in the electronics of the apparatus, to which can be associated an effective temperature, approximately equal to the sky brightness temperature T_{sky} in the case of 21 cm interferometry [66]. Mathematically the sensitivity describes the variance associated to the estimation of the visibilities, an places unavoidable constraints on how accurate our measurement can be. The 21 cm signal is extremely faint, and thus high sensitivities are required for an accurate reconstruction of the 21 cm radiation field.

In the following we derive an expression of the angular power spectrum of the noise induced by the thermal fluctuations in the interferometer, compatible with the C_ℓ formalism that we will employ in our analysis.

The measured flux in a visibility in a 21 cm experiment in the Rayleigh-Jeans limit, is [17]

$$V(\mathbf{u}) = \frac{2k_B}{\lambda^2} \int \mathrm{d}^2 n \delta T_{21}(\hat{\mathbf{n}}) A(\hat{\mathbf{n}}) e^{2\pi i \mathbf{u}\cdot\hat{\mathbf{n}}} \tag{5.11}$$

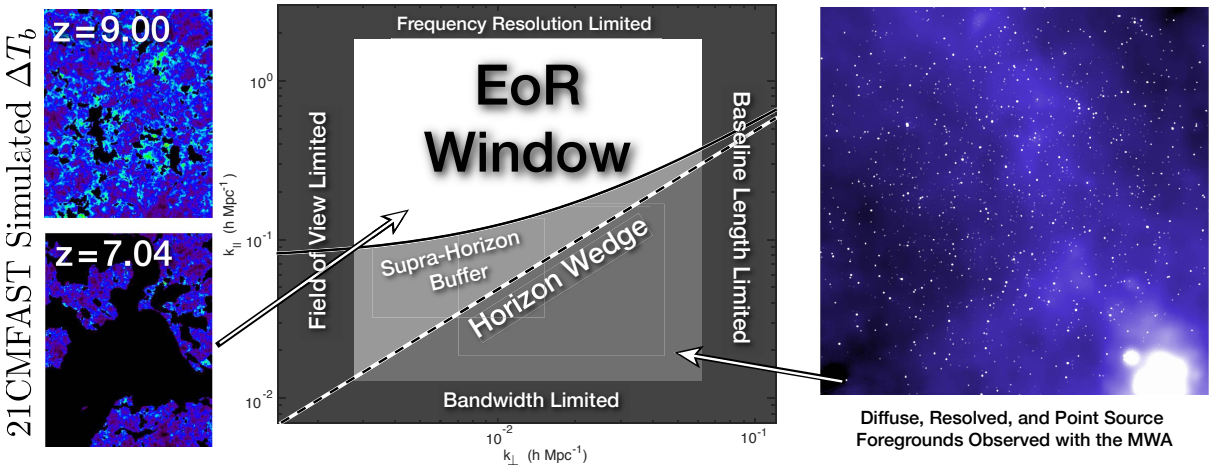

Figure 5.3: Schematic representation of the $(k_\perp, k_\parallel)$ Fourier space covered by an interferometric array, including the limitations due to the instrument and the foreground wedge, for the HERA interferometer targeted to the Epoch of Reionization. Taken from [65].

where $A(\hat{\mathbf{n}})$ is a window function describing the primary beam of the interferometer. Introducing the Fourier transforms of $A(\hat{\mathbf{n}})$ and $T_{21}(\hat{\mathbf{n}})$ we can write the average value of the squared visibilities in term of the angular power spectrum C_ℓ

$$\begin{aligned}\left\langle |V(\mathbf{u})|^2 \right\rangle &= \left(\frac{\partial B_\nu}{\partial T}\right)^2 \int d^2u' \left|\tilde{A}\left(\mathbf{u}-\mathbf{u}'\right)\right|^2 C_{\ell=2\pi u'} \\ &\approx C_{\ell=2\pi u}\left(\frac{2k_B}{\lambda^2}\right)^2 \int d^2u' \left|\tilde{A}\left(\mathbf{u}-\mathbf{u}'\right)\right|^2\end{aligned} \tag{5.12}$$

Where the C_ℓ are defined as

$$\left\langle \widetilde{\delta T_b}\left(\mathbf{u}_1\right) \widetilde{\delta T_b}\left(\mathbf{u}_2\right)\right\rangle = \delta^D\left(\mathbf{u}_1+\mathbf{u}_2\right) C_{\ell=2\pi u_1}. \tag{5.13}$$

The relation $\ell = 2\pi u$ links the Fourier space coordinate u with the angular scale ℓ. We then need to quantify the power spectrum induced by the thermal fluctuations in the instrument. If a visibility is observed for a time t_u the average noise squared is given by [67]

$$\left\langle |N(\mathbf{u})|^2 \right\rangle = \left(\frac{2k_B T_{sys}}{A_{\mathrm{e}}}\right)^2 \frac{1}{\Delta\nu t_u} \tag{5.14}$$

where A_e is the effective area of a single antenna. Using this relation we can define the angular power spectrum of the instrumental noise C_ℓ^N, analogously to the angular power spectrum C_ℓ, such that

$$\left\langle |N(\mathbf{u})|^2 \right\rangle \equiv C_\ell^N \int d^2u' |\tilde{A}\left(\mathbf{u}-\mathbf{u}'\right)|^2 \tag{5.15}$$

which gives:

$$C_\ell^N = \left(\frac{\lambda^2 T_{\mathrm{sys}}}{A_{\mathrm{e}}}\right)^2 \frac{1}{\Delta\nu t_\nu \int d^2u' |\tilde{A}\left(\mathbf{u}-\mathbf{u}'\right)|^2} \tag{5.16}$$

where T_{sys} is the system temperature, dominated by the galactic synchrotron radiation, given by eq (5.10) in the regime we work.

Using the fact that $\tilde{A}(\mathbf{u})$ has to integrate to 1 and is different from zero in an area $\delta^2 u$ we can estimate the beam integral $\int d^2u' |\tilde{A}(\mathbf{u}-\mathbf{u}')|^2 \sim 1/\delta^2 u \sim A_e/\lambda^2$. The noise power spectrum then simplifies to

$$C_\ell^N = \frac{T_{sys}^2}{\Delta\nu t_\nu \delta^2 u} \tag{5.17}$$

The reason of this relation can be understood intuitively considering the fact that the RMS of the noise for visibility corresponding to a Fourier space pixel after an observation of time t_u is $\sigma_N^2 = T_{\rm sys}^2/\Delta\nu t_u$. The noise power spectrum is then given by the variance per Fourier pixel $C_\ell^N = \sigma_N^2/\delta^2 u$.

We then need to estimate t_u, i.e. the time that each visibility is observed. Given the size of interferometric arrays, the whole instrument cannot be rotated and each visibility is only observed for a fraction of the total observation time t_o. Introducing $\ell_{\rm max}$, the maximum ℓ that can be observed with a given interferometer, determined by its largest baseline, the total area in the Fourier plane that will be covered by the observation due to the Earth rotation will be $\pi^2\ell_{\rm max}$. However, at any given instant only an area $N_{\rm pairs}\delta^2\ell = N_{\rm pairs}(2\pi)^2\delta^2 u$ is being observed. Each visibility is then observed for a time t_u

$$t_u \simeq t_o \frac{N_{\rm pairs}\delta^2\ell}{\pi l_{\rm max}^2} \simeq t_o \frac{N_{\rm ant}^2\delta^2\ell}{2\pi\ell_{\rm max}^2} \tag{5.18}$$

Where we approximated the number of pairs as $N_{\rm ant}^2$, valid for large $N_{\rm ant}$, and assumed a uniform coverage across the Fourier plane. Plugging this relation in (5.17) we obtain

$$\frac{\ell^2 C_\ell^N}{2\pi} = \frac{T_{\rm sys}^2\,(2\pi)^2}{\Delta\nu t_o}\left(\frac{\ell_{\rm max}^2}{N_{\rm ant}\delta^2\ell}\right)^2\left(\frac{\ell}{\ell_{\rm max}}\right)^2 \tag{5.19}$$

Introducing the variable $f_{\rm cover}$, defining the fraction of the total area covered by antennae,

$$f_{\rm cover} \equiv N_{\rm ant}A_e/A_{\rm total} = \frac{N_{\rm ant}\delta^2\ell}{\ell_{\rm max}}, \tag{5.20}$$

our final expression for the instrumental noise is then [17]

$$C_\ell^N = \frac{(2\pi)^3 T_{\rm sys}^2(\nu)}{\Delta\nu t_o f_{\rm cover}^2}\left(\frac{1}{\ell_{\rm max}(\nu)}\right)^2. \tag{5.21}$$

The power spectrum induced by thermal noise is thus dependent on the redshift due to the z dependence of both $T_{\rm sys}$ and $\ell_{\rm max}$.

Chapter 6

Methodology and data analysis

In the previous chapters we examined how perturbations produced during inflation evolve due to gravitational interaction and eventually determine the clustering of matter that can be observed in cosmological probes such as galaxy surveys, IM experiments and lensing surveys. We connected the power spectrum of 21 cm fluctuations with the primordial power spectrum through the dependence of the former from the matter power spectrum. We also described the instrumental apparatus that is used to capture those fluctuations, and characterized it. In this chapter we will analyze how 21cm IM experiments will be able to constrain the PPS, in particular placing constraints in the running parameters describing the deviation from scale invariance.

In the first section we will analyze whether it will be possible to measure the running parameters produced by SFSR inflation, while in the second section we will consider whether future experiments will be able to detect running parameters that will imply PBH production on small scales.

In our analysis we will always assume for simplicity that the already mentioned large astrophysical foregrounds have been already subtracted, and therefore the only signal coming into the detector will be the 21 cm radiation of cosmological origin. The power spectrum therefore will have two contributions, from the signal itself and from the noise, which we modeled.

Spec	SKAO	aSKA	LRA1	LRA2	LRA3
D_{base} (km)	6	100	30	100	300
f_{cover}	0.02	0.2	0.1	0.5	0.75
t_{obs} (years)	5	10	5	5	5
$\ell_{\text{max}}\frac{1+z}{31}$	5790	96515	28954	96515	289547
f_{sky}	0.75	0.75	0.75	0.75	0.75
Bandwidth (MHz)	1	1	1	1	1
Maximum z	30	33	200	200	200

Table 6.1: Instrument specifications for the SKAO, an advanced ground-based SKAO-like experiment (aSKA), and three realisations of a futuristic lunar radio array (LRA).

6.1 Fisher matrix formalism

Our main objective in this work is to gauge the ability of an intensity mapping experiment to constrain the primordial power spectrum by measuring the 21 cm angular power spectrum, and determine if those constraints will be tight enough to check the validity of the single field slow roll inflationary dynamics.

In order to do this, we employ the Fisher matrix approach [68, 69]. The Fisher matrix is a statistical tool that let us compute the best estimate of how much information the measurement

of a random variable that depends on a set of parameters will give us on those parameters. Therefore, the Fisher matrix lets us forecast the uncertainties on cosmological parameters of an upcoming cosmological experiment. The Fisher matrix is defined as

$$\mathcal{F}_{\alpha\beta} = \left\langle -\frac{\partial^2 \ln \mathcal{L}(\theta)}{\partial\theta_\alpha \partial\theta_\beta} \right\rangle \tag{6.1}$$

where $\mathcal{L}$ is the likelihood, depending on a set of parameters θ, describing the probability of measuring some data, in our case the data being the C_ℓs, given a set of parameters the data depends on.

The inverse of the Fisher matrix is related to the covariance matrix by the Kramer-Rao inequality:

$$\text{Cov} \geq \mathcal{F}^{-1}, \tag{6.2}$$

where the "=" holds if the likelihood is gaussian. That is, inverting the Fisher matrix gives the best possible estimate of the covariance matrix for a certain experiment. It's important to note that the uncertainties on each parameter obtained by inverting the Fisher matrix are already marginalized over the remaining parameters, assuming that all the parameters are estimated simultaneously from the experimental data.

Additionally, the Fisher matrices of different, independent measurements can be added to provide the uncertainties of the combined experiments. This also means that one can easily introduce prior knowledge on parameters of a Fisher forecast from other, already performed experiments.

Assuming the C_ℓs are gaussian distributed, the Fisher matrix can be computed as [70]

$$\mathcal{F}_{\alpha\beta}^{21\text{ cm}} = \sum_\ell \frac{\partial C_\ell}{\partial\theta_\alpha} \frac{\partial C_\ell}{\partial\theta_\beta} \sigma_{C_{\ell\ell'}}^{-2} \tag{6.3}$$

where $\sigma_{C_{\ell\ell'}}$ is the variance of the C_ℓs

$$\sigma_{C_{\ell\ell'}} = \sqrt{\frac{2\left(C_\ell + C_{\ell\ell'}^N\right)^2}{f_{\text{sky}}(2\ell+1)}} \delta_{\ell\ell'}^K \tag{6.4}$$

Where f_{sky} is the sky fraction covered by the instrument and C_ℓ^N is the noise power spectrum (5.21). This result can be intuitively thought as the following: the more our observable (the C_ℓs) depend on the parameters, the bigger the derivatives $\partial C_\ell/\partial\theta_\alpha$ will be, and thus the relevant entry of $\mathcal{F}$ will be bigger, implying a smaller covariance matrix. Additionally, the greater the ℓ, the more coefficients can be sampled, reducing the variance. The noise, instead, acts as a suppression factor, reducing the constraining power of the experiment. A an example, we show the total power spectrum, the 21 cm power spectrum and the noise power spectrum in figure 6.1.

6.2 21 cm PPS constraints

Currently the simplest model to describe inflation is the Single field Slow Roll (SFSR) model, in which the running parameters are related to the potential of the inflaton field and its derivatives through the slow roll parameters. In order for SFSR inflation to happen, those parameters must be small, and each running is suppressed with respect to the lower order one. However, each running affects the power spectrum more the more we move away from the pivot scale, conventionally set at $k = 0.05\,\text{Mpc}^{-1}$, where current observations like CMB experiments and

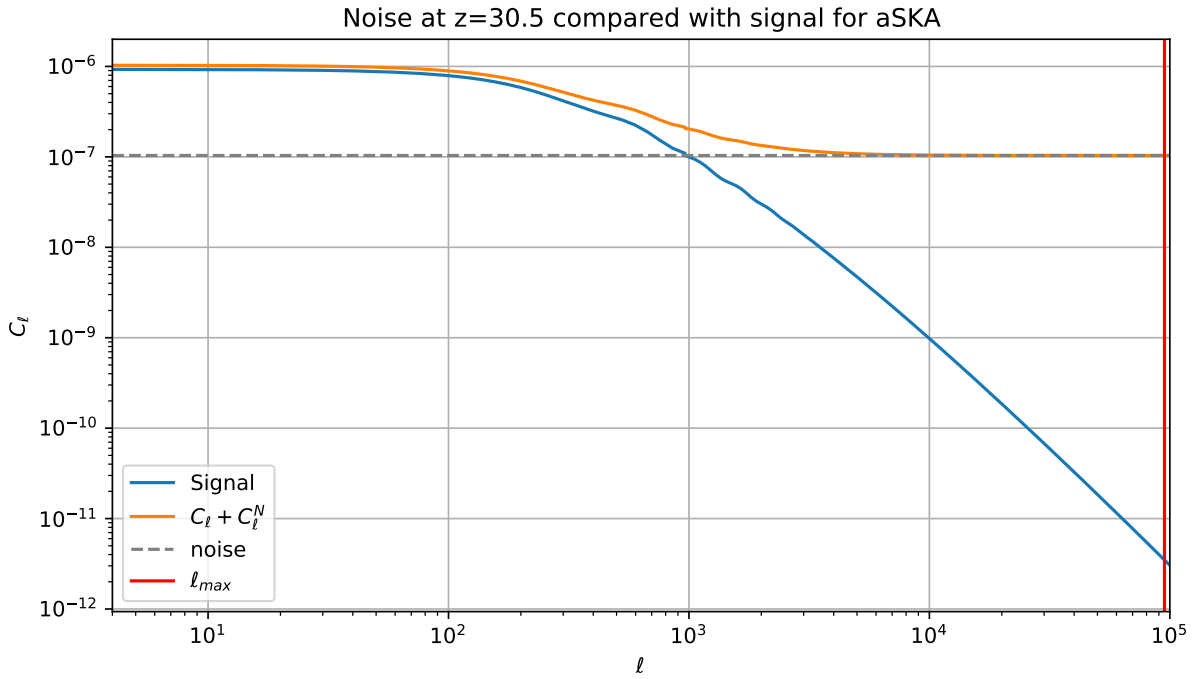

Figure 6.1: Angular power spectrum of the 21 cm line computed with a bandwidth of 1 MHz. In blue we show the C_ℓ of the signal. The grey line represent the noise, constant in ℓ, and the orange line the sum of the two. The red line is the maximum $\ell_{\rm max}$ reachable by the given experimental apparatus at the given redshift.

clustering surveys tightly constrain the power spectrum. In this picture, 21 cm IM experiments could theoretically provide stronger constraining power due to their ability to reach much smaller scales, as well as probing a much greater number of modes than the CMB due to an enormously larger observable volume.

We include, as well as the primordial parameters in the parameterization of $\mathcal{P}_\zeta(k)$ shown in equation 3.46, also the parameters $\omega_{\rm CDM}$, $\omega_{\rm b}$ and h. Our parameter space is therefore

$$P = \{A_s,\ n_s,\ \alpha_s,\ \beta_s,\ \gamma_s,\ \omega_{\rm CDM},\ \omega_{\rm b},\ h\}\,. \tag{6.5}$$

We also consider a reduced parameter space in which the third running parameter γ_s is not included.

We assume the values obtained from Planck 2018 TT,TE,EE+lowE [1] as our fiducial cosmology.

We then compute the numerical derivatives of the C_ℓs with respect to each parameters. In order to do this we use an internal code, adapted to take as input the matter power spectrum from CLASS [71] which itself depends on the primordial power spectrum, our target observable. In order to speed up the code, for $\ell \geq 1000$ the Limber approximation is used [72].

Figure 6.1 shows an example of the output of our code, showing the maximum ℓ that can be measured by the instrument, the power spectrum of the cosmological signal computed with a 1 MHz window function, and the total power spectrum as the sum of the signal and the noise power spectrum. In figure 6.2 we instead show the numerical derivatives obtained in order to compute the Fisher matrix. Due to numerical instabilities in the code, we computed the derivatives for the Ω parameters instead of $\omega \equiv h^2\Omega$, we then performed a variable change in the Fisher matrix according to the prescriptions in [73].

In our analysis we consider five experimental setups: the SKAO interferometric array currently in construction, another ground based larger interferometric experiment dubbed "aSKAO" and

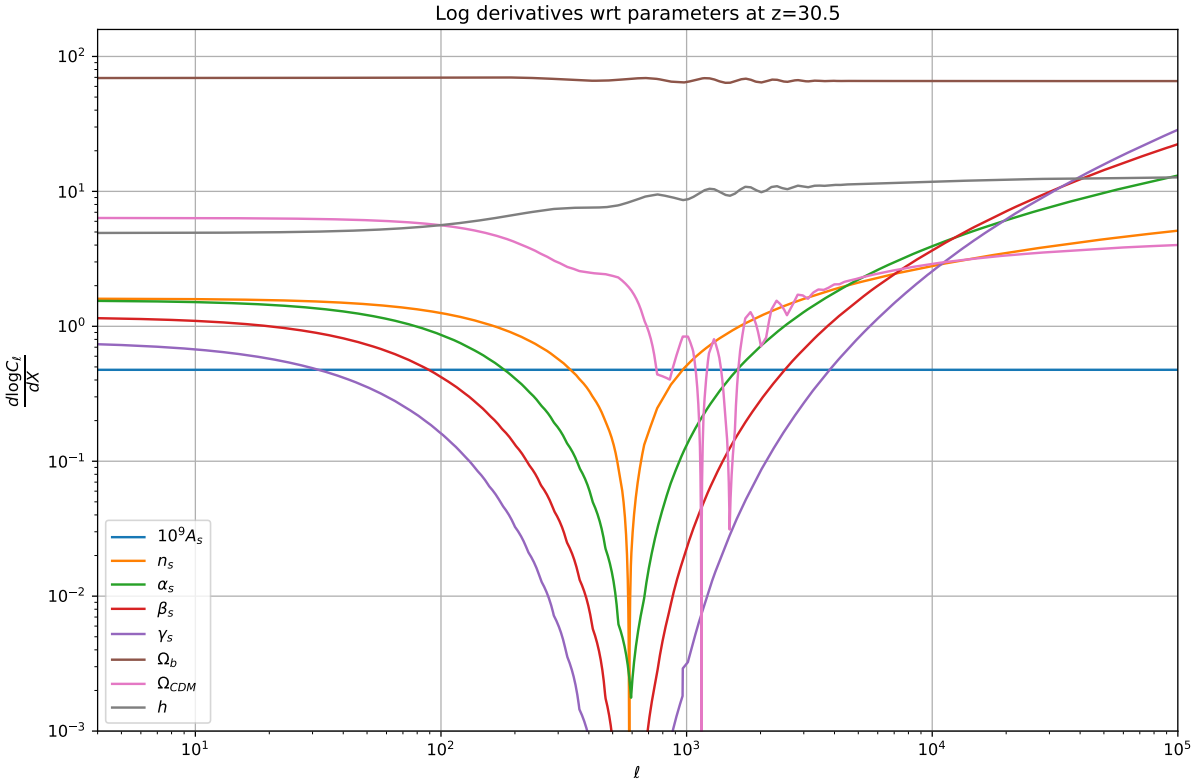

Figure 6.2: Logarithmic derivatives of the angular power spectrum with respect to the parameters we considered in our analysis.

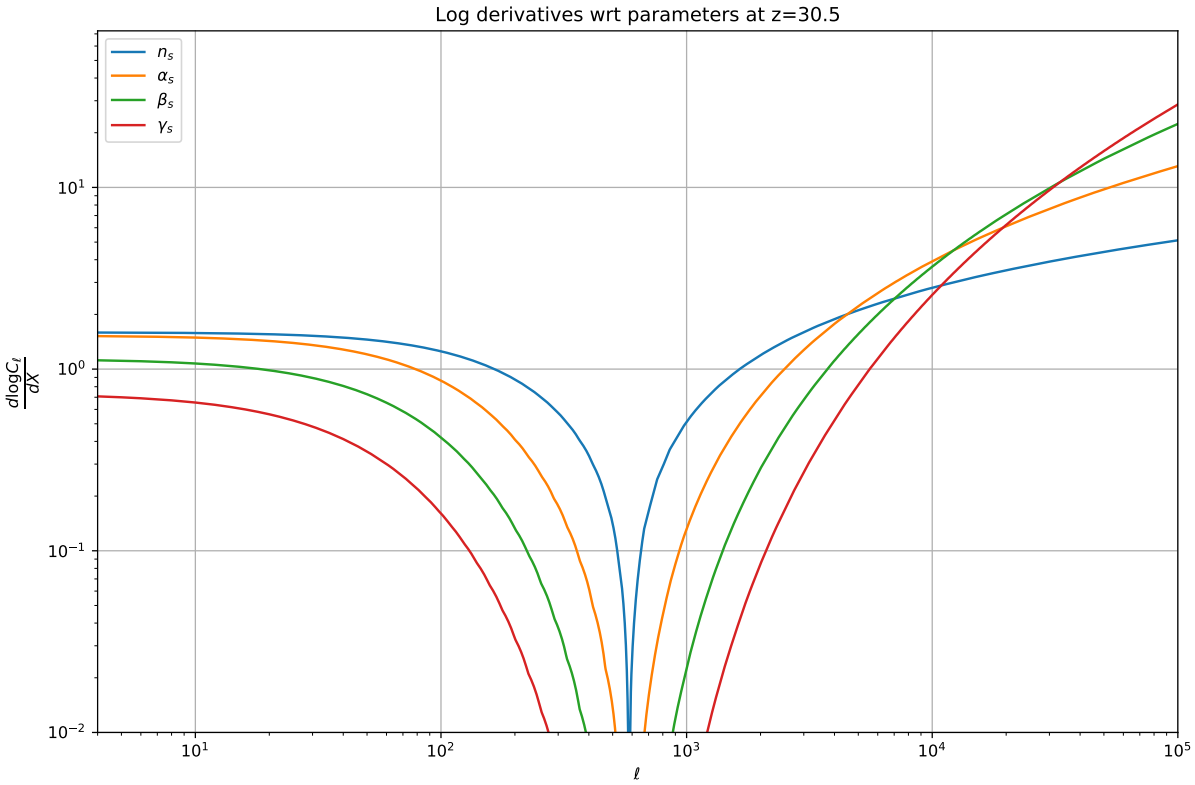

Figure 6.3: Logarithmic derivatives of the angular power spectrum with respect to the primordial parameters.

three different versions of lunar interferometers. The relevant specifications of the experiments are listed in table 6.1. For all the experiments we consider a sky fraction $f_{\rm sky} = 0.75$ and a bandwidth $\Delta\nu = 1$ MHz. The lunar based experiments can reach up to redshift 200, while SKAO will only be able to observe the very last moments of the Dark Ages at $z = 30$. For the futuristic aSKAO we instead consider a slightly increased redshift range, up to $z = 33$, theoretically still reachable within the Earth atmosphere.

In order to better exploit the large volume of space available for 21 cm intensity mapping we consider a tomographic analysis. That is, instead of measuring the C_ℓs in only one redshift slice as in the CMB, the volume can be divided in concentric slice, each providing data for the experiment. This is possible as long as the redshift slices are uncorrelated. In [21] it was found that redshift slices can be safely considered uncorrelated if separated by more than 1 MHz in frequency space, which is also our choice for the bandwidth of the experiment, therefore we divide our redshift range from $z = 30$ to $z = 200$ in up to 39 redshift slices, and add the Fisher matrices for each slice together.

Our final choice of redshift bins in order to maintain a separation of 1 MHz in frequency is then:

$$\begin{aligned} z_{\rm bins} = \{&30.5,\ 31.3,\ 32.,\ 32.8,\ 33.6,\ 34.5,\ 35.4,\ 36.3,\ 37.3,\ 38.4,\ 39.5,\ 40.7,\ 42.,\\ &43.3,\ 44.7,\ 46.3,\ 47.9,\ 49.6,\ 51.5,\ 53.5,\ 55.7,\ 58.,\ 60.6,\ 63.4,\ 66.5,\ 69.8,\ 73.5,\\ &77.6,\ 82.3,\ 87.4,\ 93.3,\ 100.,\ 107.7,\ 116.7,\ 127.4,\ 140.1,\ 155.7,\ 175.1,\ 200.\} \end{aligned} \tag{6.6}$$

The total Fisher matrix is then the sum of the Fisher matrices for every uncorrelated slice:

$$\mathcal{F}^{21\ \rm cm}_{\alpha\beta} = f_{\rm sky} \sum_z \sum_\ell^{\ell_{\rm max}} \frac{2\ell+1}{2(C_\ell + C_\ell^N)^2} \frac{\partial C_\ell}{\partial\theta_\alpha} \frac{\partial C_\ell}{\partial\theta_\beta}. \tag{6.7}$$

6.2.1 Results

We therefore provide the forecasts of the constraining power of the previously discussed 21 cm IM experiments on the primordial parameters. Table 6.2 lists the constraints from IM experiments without assuming any prior knowledge on the cosmological parameters we included in our model, compared with Planck 2018 results. Instead, table 6.3 and table 6.4 also include priors on $\omega_{\rm CDM}$, ω_b, h, A_s from the Planck collaboration [1].

The first thing to be noticed is the poor constraining power of both SKAO and LRA1, both being unable to provide any meaningful constraint on the parameters of interest, even with the priors from Planck 2018 on the nuisance parameters and despite the increased redshift range of the latter. This is mainly due to the low baseline of the instruments, that doesn't allow to reach high enough ℓ's where the effect of the running parameters on the C_ℓs is bigger (see figure 6.3), as well as increasing the noise through the dependence $C_\ell^N \propto \ell_{\rm max}^{-2}$. It should be noted that SKAO is not designed to observe the Dark Ages, so its poor performance in this regime is to be expected. In the rest of the analysis we will focus on the remaining three experiments: aSKAO, LRA2 and LRA3, whose forecasted confidence ellipses for the primordial parameters are shown in figure 6.6 and 6.7, respectively without and with the Planck 2018 priors included in the analysis. As expected, instruments with larger baselines and increased survey volume perform better and are also less affected by the inclusion of Planck priors due to they already extremely good accuracy in parameter estimation.

Comparing table 6.3 and 6.4 we can also appreciate the effect of adding the third running parameter in our model. Unsurprisingly, the uncertainties become overall worse if the parameter space is augmented, as the primordial parameters are correlated. The parameter whose uncertainties are most affected by the addition of the third running γ_s in the model is the second running β_s,

which is due to the correlation between the two parameters, as can be seen for example in figure 6.4, comparing the confidence ellipses forecasted for aSKAO for the 2- and 3-runnings models.

The effect of introducing Planck 2018 priors for $\omega_{\rm CDM}$, ω_b, h, A_s is shown in figure 6.5 for the aSKAO experiment. The primordial parameters more greatly affected by introducing Planck priors are A_s and n_s, while the running parameters don't show an appreciable improvement in the error bars.

It's also worth to point out the decrease of uncertainties of higher order runnings compared to the lower order ones in certain regimes, for example the uncertainty in γ_s for LRA3 is half the uncertainty in β_s and α_s, which are about the same. As this effect is more noticeable with the increase in baseline, we attribute this to the experiment being able to probe higher ℓ's, and thus regimes in which the power spectrum is more sensitive to higher order runnings, as shown in figure 6.3. As ℓ increases, the logarithmic derivatives of higher order runnings grow more than lower order, eventually overtaking them. Additionally, higher ℓ weigh more in the Fisher information matrix due to each ℓ contributing $2\ell+1$ components and thus being multiplied by the factor $2\ell+1$ in the Fisher matrix (6.7).

Lastly, we discuss the possibility of the experiments detecting the running parameters predicted by the SFSR model. Those parameters are expected to be of order [21]

$$\alpha_s \simeq \mathcal{O}[(n_s-1)^2] \simeq 10^{-3} \qquad \beta_s \simeq \mathcal{O}[(n_s-1)^3] \simeq 10^{-5} \qquad \gamma_s \simeq \mathcal{O}[(n_s-1)^4] \simeq 10^{-6}. \quad (6.8)$$

We note that no experiment is sensitive enough to detect either β_s or γ_s, as they are respectively one and two orders of magnitude too small even for the best performing experiment. LRA2 and LRA3 instead could be able to detect α_s, while for aSKAO the possibility of a detection is less certain.

Experiment	$\sigma(10^9 A_s)$	$\sigma(n_s)$	$\sigma(\alpha_s)$	$\sigma(\beta_s)$	$\sigma(\gamma_s)$
SKAO	3.1e+03	2.1e+02	1.5e+02	1.3e+02	4.2e+02
aSKAO	0.12	0.01	0.0046	0.0078	0.0081
LRA1	3.1	0.23	0.13	0.12	0.26
LRA2	0.03	0.0035	0.0016	0.0027	0.0025
LRA3	0.0074	0.0015	0.00085	0.00089	0.00049
Planck 2018	0.030	0.0042	0.010	0.013	N/A

Table 6.2: Marginalized uncertainties on PPS parameters without Planck priors, compared with Planck 2018 uncertainties.

6.3 PBH formation from curvature perturbations

PBH are black holes that are supposed to have formed in the early Universe due to the collapse of large (in amplitude) perturbations in the density field. There are many possible mechanisms that

Experiment	$\sigma(10^9 A_s)$	$\sigma(n_s)$	$\sigma(\alpha_s)$	$\sigma(\beta_s)$	$\sigma(\gamma_s)$
SKAO	0.034	4.5e+01	8.6e+01	1.3e+02	3.5e+02
aSKAO	0.028	0.005	0.0034	0.0077	0.0081
LRA1	0.032	0.047	0.087	0.12	0.24
LRA2	0.017	0.0028	0.0014	0.0027	0.0025
LRA3	0.0064	0.0014	0.00082	0.00088	0.00049

Table 6.3: Marginalized uncertainties on PPS with Planck priors on $\omega_{\rm CDM}$, ω_b, h, A_s.

Experiment	$\sigma(10^9 A_s)$	$\sigma(n_s)$	$\sigma(\alpha_s)$	$\sigma(\beta_s)$
SKAO	0.034	4.3e+01	3.7e+01	1.2e+02
aSKAO	0.028	0.0046	0.0034	0.0035
LRA1	0.031	0.045	0.046	0.10
LRA2	0.017	0.0027	0.0014	0.0011
LRA3	0.0064	0.0014	0.00065	0.00024

Table 6.4: Marginalized uncertainties on PPS with Planck priors on $\omega_{\rm CDM}$, ω_b, h, A_s, parameterization with 2 runnings.

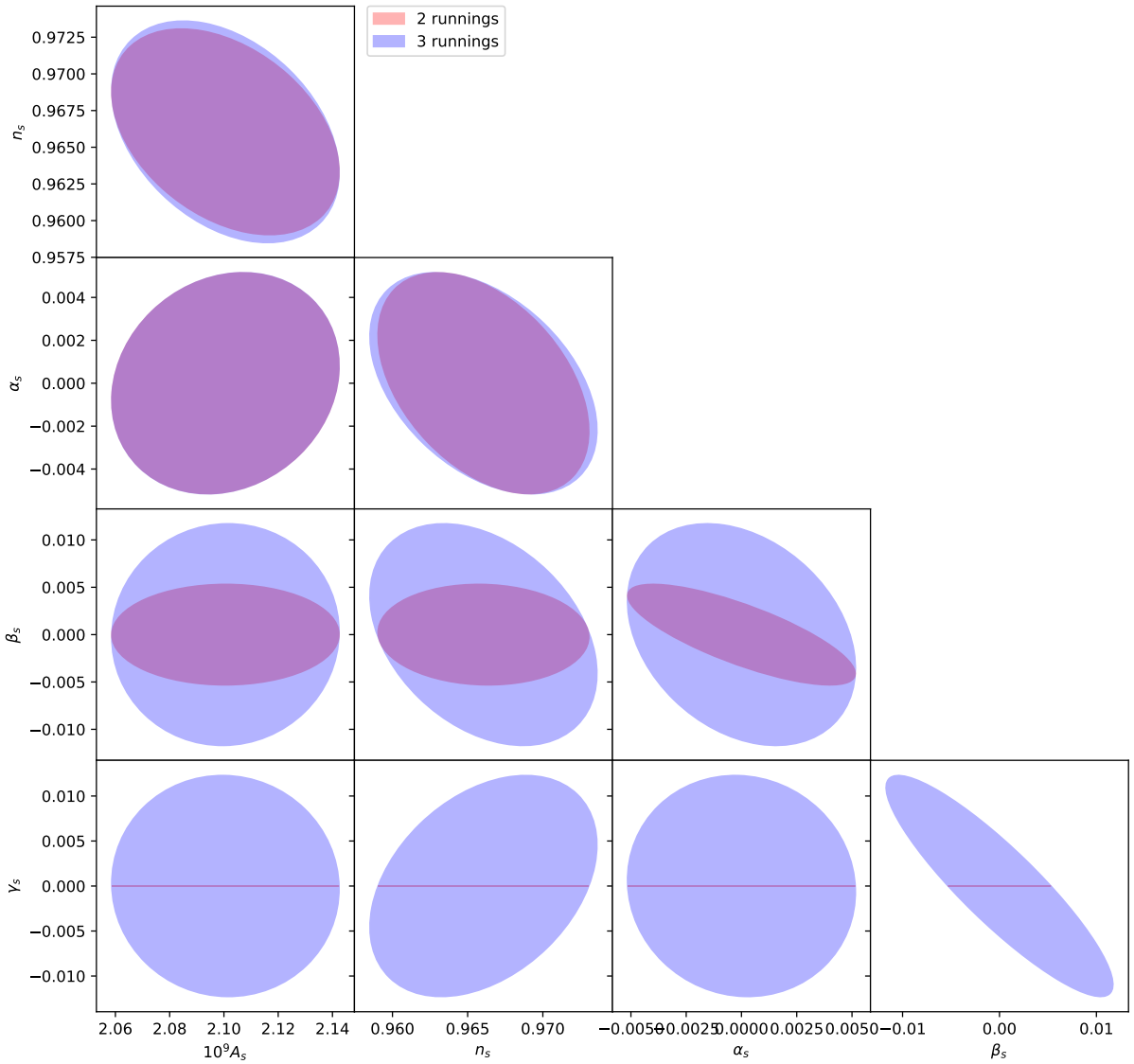

Figure 6.4: 68% CL ellipses for PPS parameters with aSKAO obtained by modeling the PPS with 2 and 3 spectral runnings. The γ_s parameter is set to 0 in the "2 runnings" case, therefore the related confidence ellipses are shown as lines.

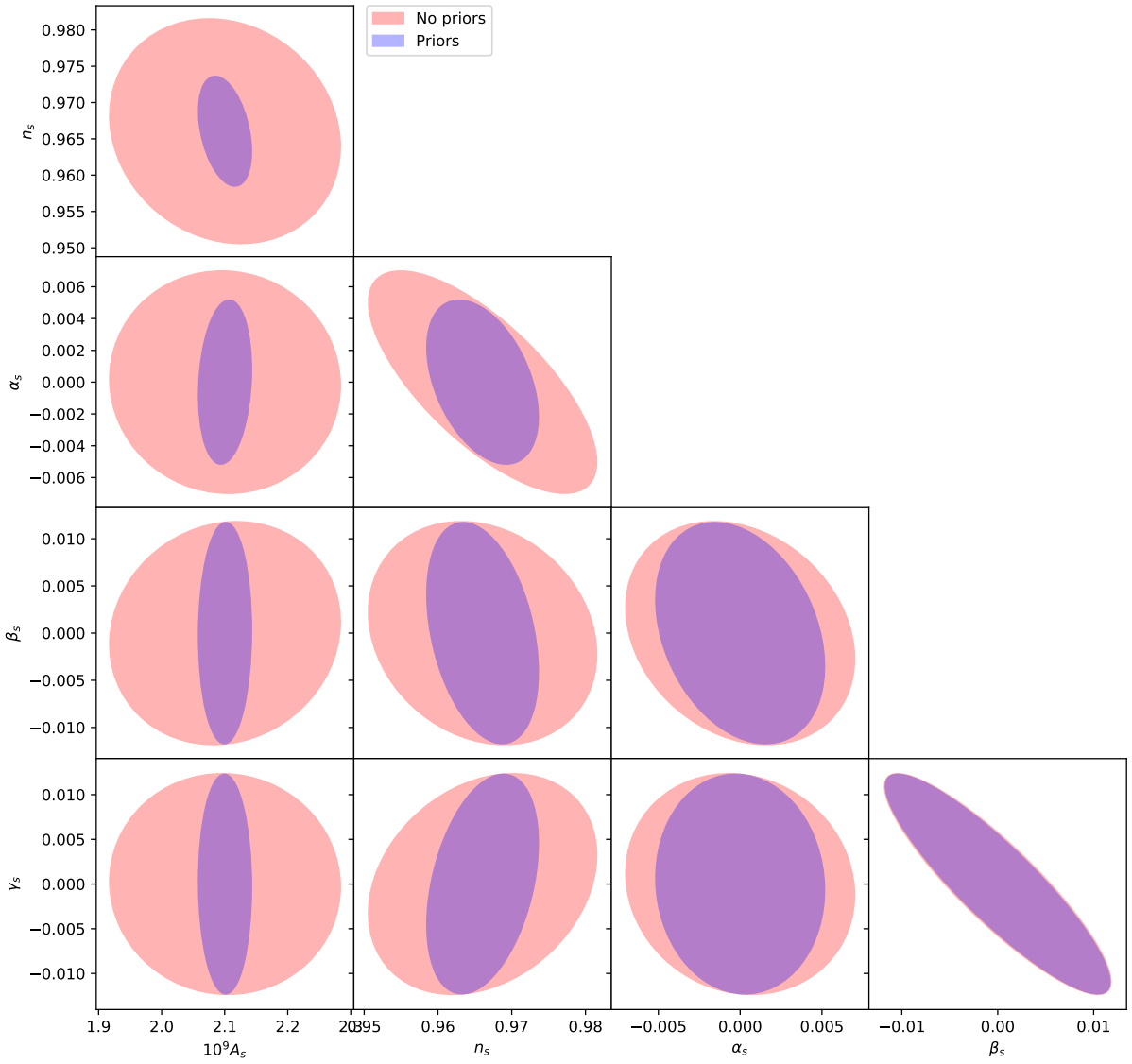

Figure 6.5: 68% CL ellipses before and after including Planck 2108 priors priors on $\omega_{\rm CDM}$, ω_b, h, A_s for aSKAO.

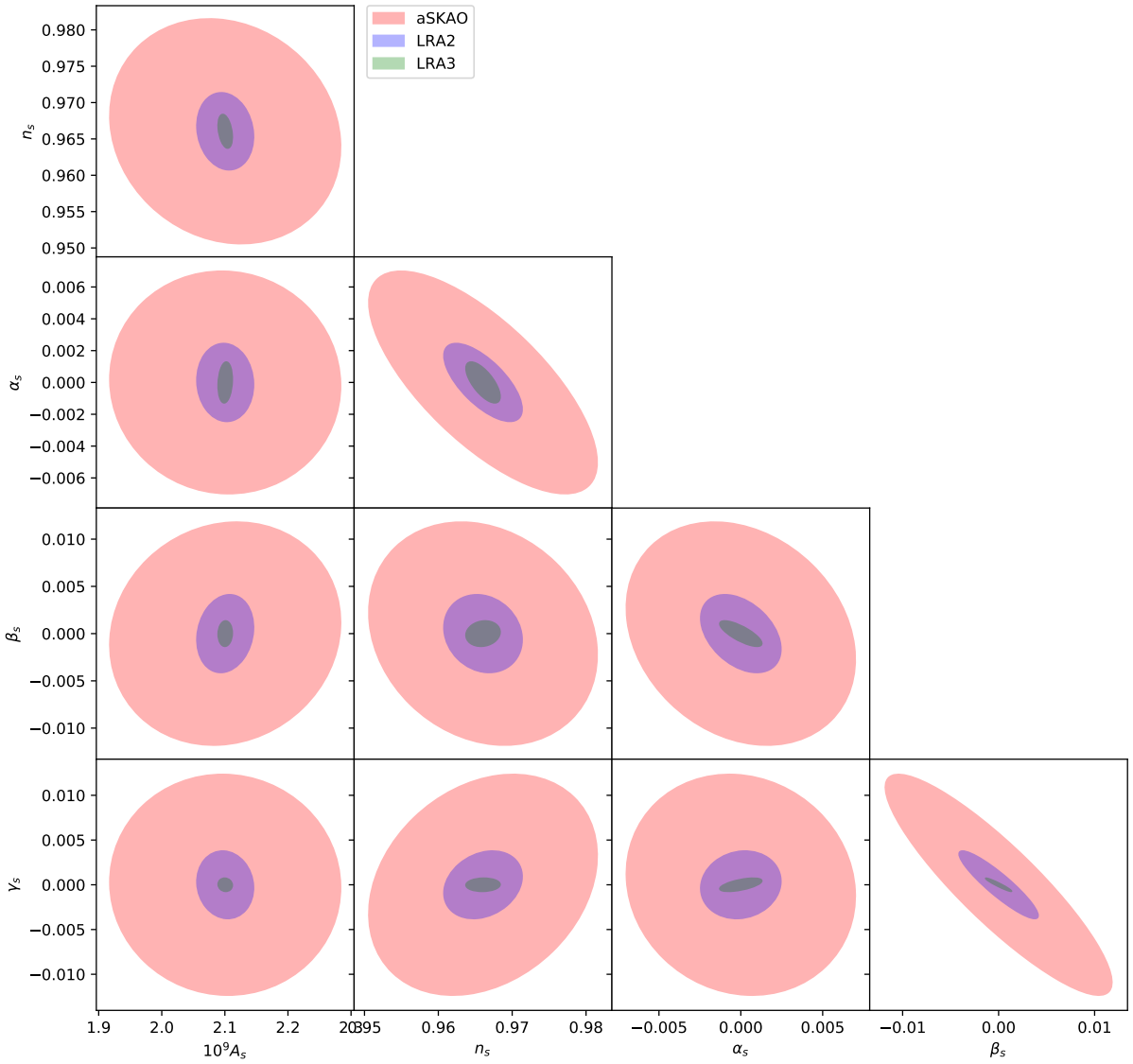

Figure 6.6: Comparison between 68% CL ellipses for aSKAO, LRA2 and LRA3 without Planck priors.

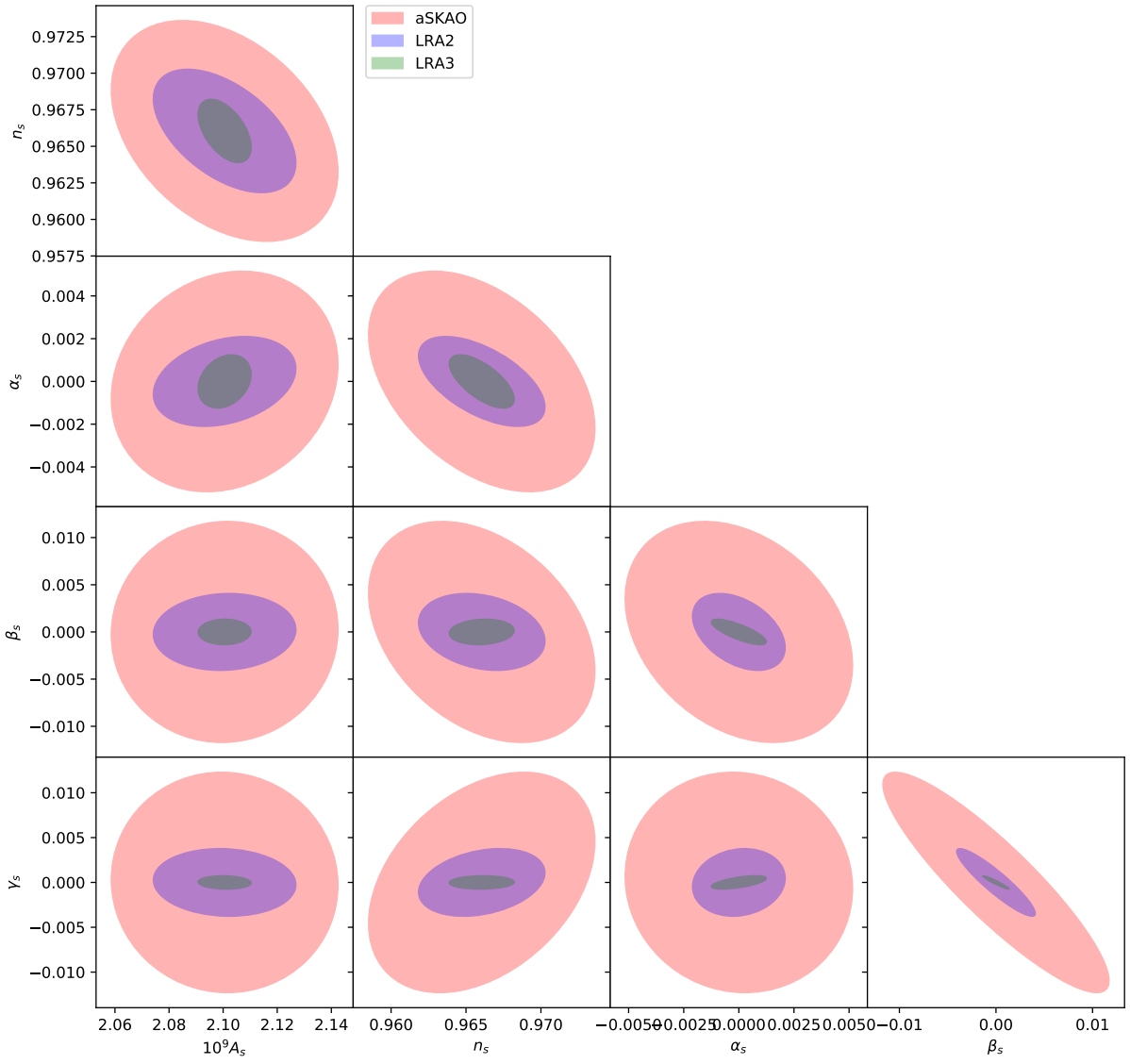

Figure 6.7: Comparison between 68% CL ellipses for aSKAO, LRA2 and LRA3, with Planck 2018 priors

allow the production of such overdensities, we are particularly interested in the PBH produced by the collapse of curvature perturbations generated during inflation (CPBH). The standard SFSR inflation is expected to not generate any CPBH as it doesn't produce curvature perturbations large enough due to being characterized by almost scale invariant primordial power spectrum, measured to be $\mathcal{O}(10^{-9})$ at CMB scales. However, other inflationary models, such as models including multiple fields or ultra slow roll phases, can instead produce sizable departures from a scale invariant PPS, which could reach sufficient amplitudes at small scales so that CPBH can form.

We previously examined the constraining power of 21 cm experiments on the running parameters given a baseline model with $\alpha = \beta = \gamma = 0$, i.e. an almost scale invariant PPS, as predicted by the SFSR model, in order to test whether upcoming 21cm IM experiments targeted at the Dark Ages will be able to effectively tell departures from it. In the following, we will consider only a 2-running parameter space, i.e. we will fix $\gamma_s = 0$, in order to simplify the analysis.

Now we ask whether 21 cm experiments will be able to tell us something about PBH formation mechanisms. As we saw, IM experiments will place constraint in the (α_s, β_s) parameter space, therefore even if we can't directly probe the power spectrum at the scale of PBH formation, we can detect the departure from scale invariance as the PPS starts to grow in order to reach the required amplitude.

In our model we assume that the parameterization in equation (3.46) is valid up to the scale of PBH formation. We also take into account the findings in [74], where it was found that in single field inflation the power spectrum can't grow faster than k^4. In order to be consistent, we consider two scenarios: a "no runnings" scenario in which $\alpha_s = \beta_s = 0$ in which we do not expect to observe PBHs, and a scenario in which PBH form, where we assume a fiducial model as in the previous section, but set $\beta_s = 0.01$, a value consistent with the Planck 2018 TT,TE,EE+lowE+lensing analysis [75][1]. Note that in general. in order to avoid overproduction of PBH, higher order negative runnings are required, but for simplicity we ignore this aspect and just consider the parameter space that lets the PPS reach the required threshold.

Let's assume that PBH of a certain mass $M_{\rm PBH}$ are observed. If the PBH are formed from curvature perturbations, and our model is right, then we expect the runnings to be somewhere in the corresponding parameter region. The power of 21 cm experiment then comes to placing constraints in the same parameter space in the form of confidence ellipses, restricting the value that α_s and β_s can take with a certain confidence level, and allowing us to differentiate whether out PBH formation model is right (α_s and β_s are in the PBH region) or the model is wrong and PBH originated in a different way i.e. α_s and β_s are not in the PBH formation region.

In our analysis, in light of the constraints illustrated in figure 3.5, we consider the formation of PBH of $\mathcal{O}(10^{-10})M_\odot$ and $\mathcal{O}(10^{1})M_\odot$, corresponding respectively to a formation scale $k_{\rm PBH}$ of $10^{12}\,{\rm Mpc}^{-1}$ and $10^{6}\,{\rm Mpc}^{-1}$. Motivated by the uncertainties in the physical modeling of PBH formation we also consider, for each $k_{\rm PBH}$, two different formation thresholds: whether the PBH form when the PPS reaches values δ_c^2 of 1 and 10^{-2}.

6.3.1 Results

The results are illustrated in figures 6.8 and 6.10. The solid lines represent the threshold value of (α_s, β_s) that allow the PPS to reach the amplitude allowing PBH production. Since smaller PBH form from perturbations characterized by higher wavenumbers, the PPS has more room to grow and requires smaller running parameters in order to reach the required amplitude, therefore they are produced in a bigger region of the parameter space. Instead, bigger PBH would require a much stronger deviation from the scale invariant PPS in order to form, and it would be much easier for an interferometric experiment to measure the (lack of) running parameters producing

[1]While the Planck collaboration found a second running β_s=0.01, its value is still compatible with 0 at 68% confidence level, and it decreased since the previous analyses of Planck satellite data.

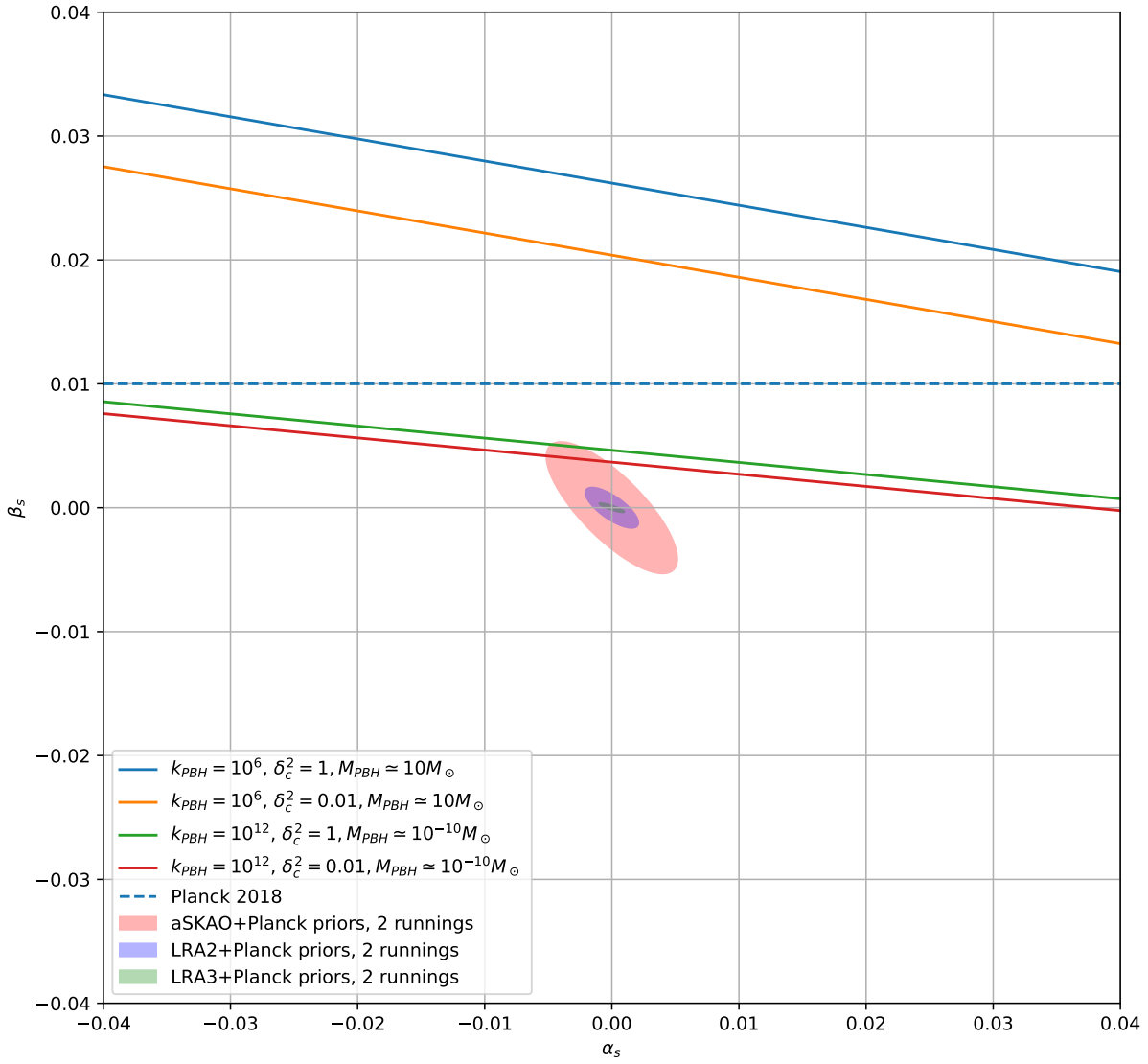

Figure 6.8: Constraints on running parameters and PBH formation thresholds, $(\alpha_s, \beta_s)_{fid} = (0, 0)$. The solid lines denote the threshold in the (α_s, β_s) parameter space above which the PPS acquires enough power at the relevant scales to form PBHs, as indicated in the legend. The confidence ellipses show the $1 - \sigma$ confidence regions for aSKAO, LRA2 and LRA3.

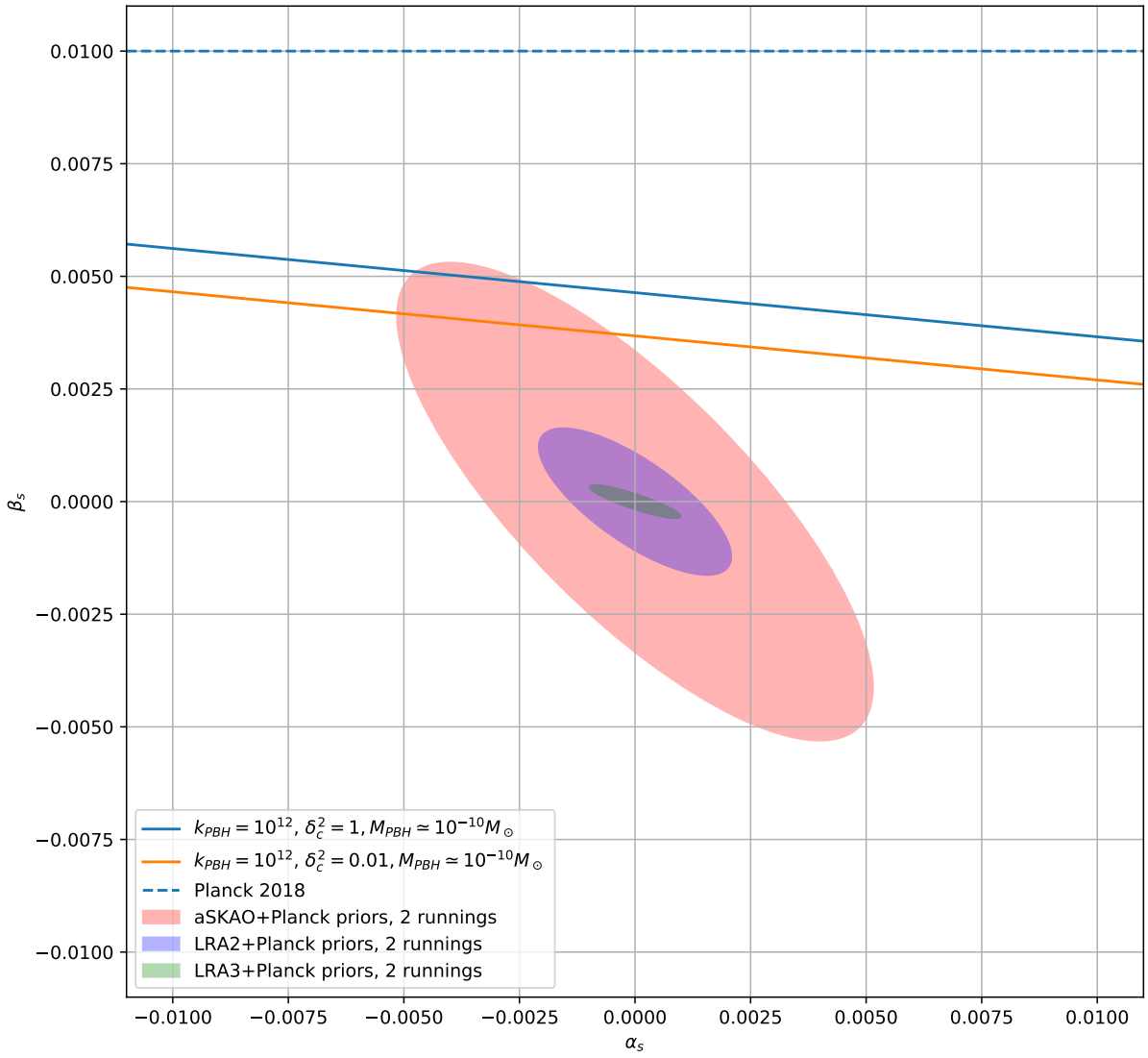

Figure 6.9: Same as figure 6.8, but zoomed in the fiducial $(\alpha_s, \beta_s)_{fid} = (0, 0)$.

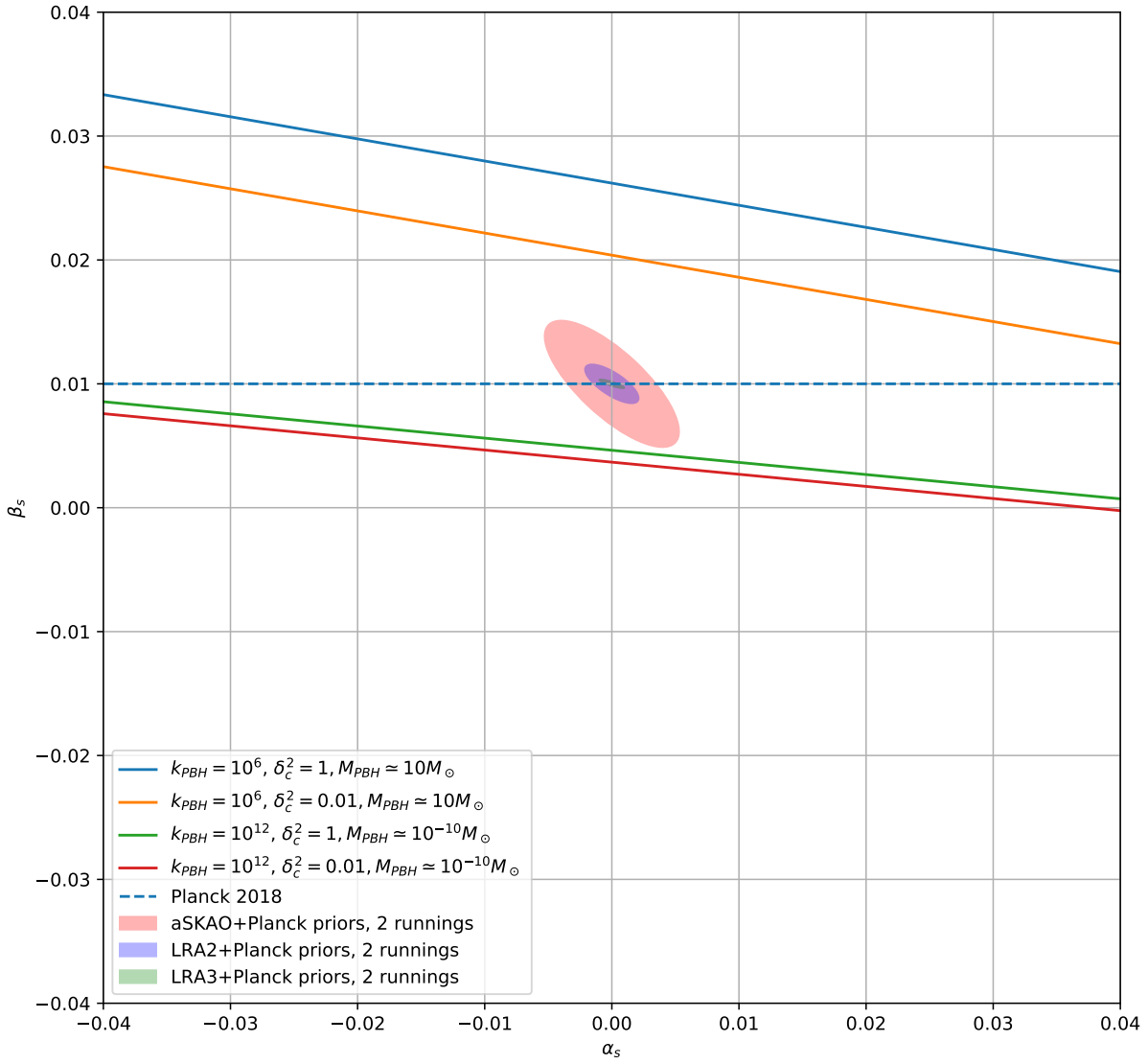

Figure 6.10: Constraints on running parameters and PBH formation thresholds, $(\alpha_s, \beta_s)_{fid} = (0, 0.01)$. The solid lines denote the threshold in the (α_s, β_s) parameter space above which the PPS acquires enough power at the relevant scales to form PBHs, as indicated in the legend. The confidence ellipses show the $1 - \sigma$ confidence regions for aSKAO, LRA2 and LRA3.

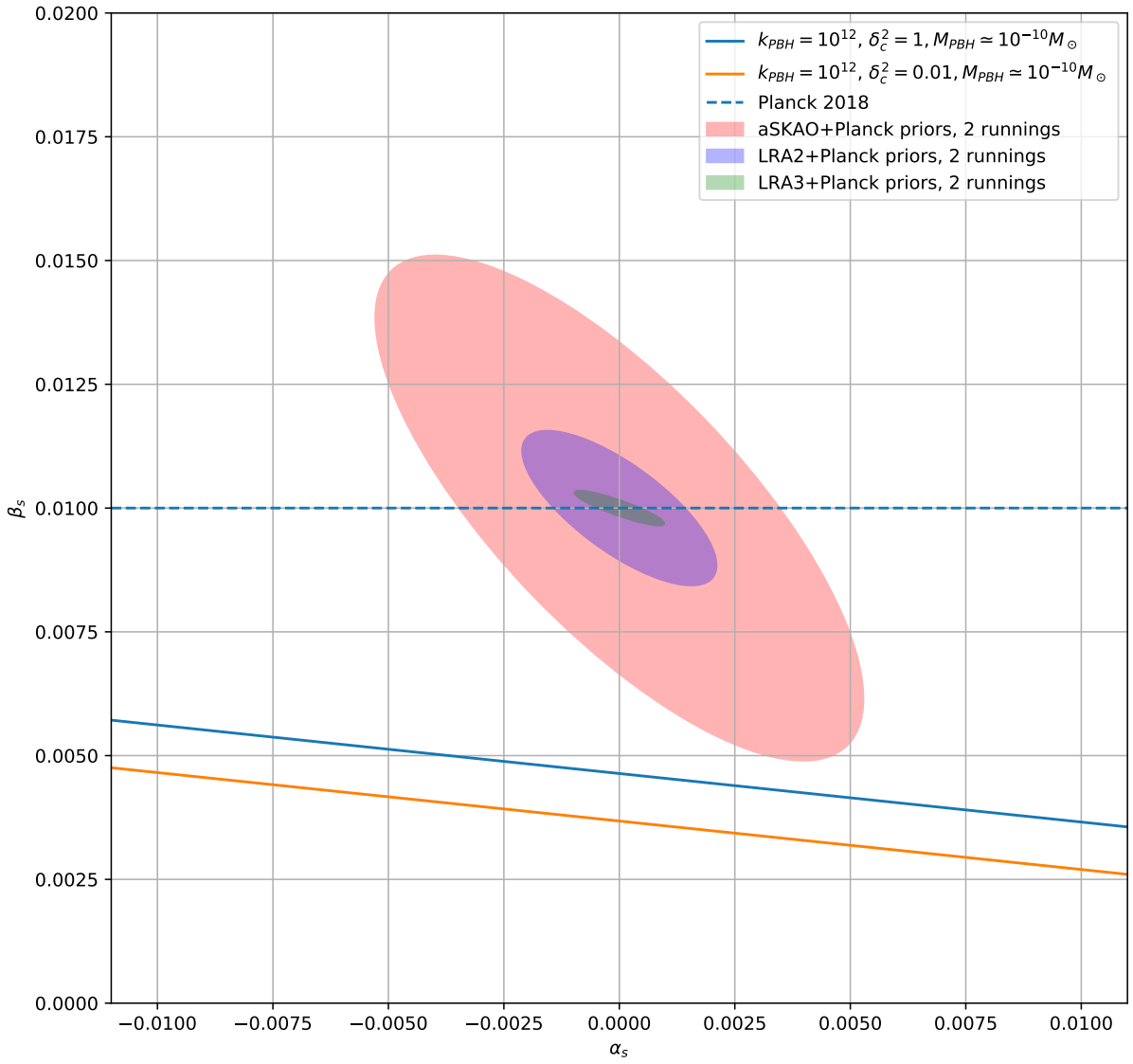

Figure 6.11: Same as figure 6.10, but zoomed in the fiducial $(\alpha_s, \beta_s)_{fid} = (0, 0.01)$.

such a stark blue tilt in the primordial power spectrum. This is evidenced in figure 6.8 by the fact that the confidence ellipses centered in $(0, 0)$ do not intersect the region in which PBH with $M_{\rm PBH} = \mathcal{O}(10)M_\odot$ form.

Instead, lowering the threshold of the PPS amplitude for PBH formation by as much as two orders of magnitude does not affect much the constraints on the (α_s, β_s) parameter space, due to the exponential growth in equation (3.46).

In the case where the Planck value of $\beta_s = 0.01$ is confirmed, all three interferometric experiments considered allow to exclude the $(\alpha_s, \beta_s) = (0, 0)$ value, i.e. the flat PPS, at σ confidence level, as well as rule out the parameter space implying the formation of $\mathcal{O}(10)M_\odot$ PBHs.

Chapter 7

Conclusions

With the development of 21 cm intensity mapping techniques and new interferometric experiments being constructed and proposed, the possibility of exploiting the enormous wealth of information given by the mapping the density field of neutral hydrogen throughout the Universe in order to increase our understanding in cosmology becomes every day more realistic.

In this work we examined in particular the possibility of using those observations focused in the Dark Ages to constrain the parameter space characterizing the primordial perturbations that imprinted the fluctuations seeding the formation of the structures characterizing our Universe.

We started from reviewing the physics of the early Universe introducing the physics of inflation, which is thought to produce the primordial fluctuations. We also considered the possibility of primordial black holes to form in the early Universe due to the collapse of large overdensities. We then introduced the physics of the 21 cm emission from neutral hydrogen at high redshifts, quantifying the global sky averaged signal and the power spectrum. Lastly, we reviewed the experimental apparatus by which intensity mapping will be made possible, radio interferometers, in particular quantifying the experimental noise affecting the observations.

Bringing this information together we employed a code in order to model the angular power spectrum of the 21 cm radiation in the Dark Ages, as observed by an interferometric array. This allowed us to perform a Fisher analysis in order to estimate the confidence regions in which the primordial parameters from which the 21 cm power spectrum depends are expected to be.

We found out that a large, futuristic Earth based array could already give us precious information pertaining the formation of Primordial Black Holes, allowing us to test models of PBH formation, while in order to measure the expected parameters predicted by SFSR inflation we will need a large, Moon based array.

As future improvements of this work we can list the inclusion of baryon-dark matter relative velocities, found to be important in the Dark Ages in [49] and a more accurate modeling of interferometric arrays.

This work can be employed in conjunction with more concrete models of the early Universe, such as multi field inflation models, in order to gauge whether future interfermoetric arrays will be able to apply constraints on them.

Bibliography

[1] N. Aghanim et al. "Planck 2018 results". In: *Astronomy & Astrophysics* 641 (Sept. 2020), A6. ISSN: 1432-0746. DOI: 10.1051/0004-6361/201833910. URL: http://dx.doi.org/10.1051/0004-6361/201833910.

[2] Ely D. Kovetz et al. *Line-Intensity Mapping: 2017 Status Report*. 2017. arXiv: 1709.09066 [astro-ph.CO].

[3] Yi Mao et al. "How accurately can 21 cm tomography constrain cosmology?" In: *Physical Review D* 78.2 (July 2008). ISSN: 1550-2368. DOI: 10.1103/physrevd.78.023529. URL: http://dx.doi.org/10.1103/PhysRevD.78.023529.

[4] Julian B. Muñoz, Yacine Ali-Haïmoud, and Marc Kamionkowski. "Primordial non-gaussianity from the bispectrum of 21-cm fluctuations in the dark ages". In: *Physical Review D* 92.8 (Oct. 2015). ISSN: 1550-2368. DOI: 10.1103/physrevd.92.083508. URL: http://dx.doi.org/10.1103/PhysRevD.92.083508.

[5] Maresuke Shiraishi et al. "Violation of statistical isotropy and homogeneity in the 21-cm power spectrum". In: *Physical Review D* 93.10 (May 2016). ISSN: 2470-0029. DOI: 10.1103/physrevd.93.103506. URL: http://dx.doi.org/10.1103/PhysRevD.93.103506.

[6] Katie Short et al. "Enlightening the dark ages with dark matter". In: *Journal of Cosmology and Astroparticle Physics* 2020.07 (July 2020), 020–020. ISSN: 1475-7516. DOI: 10.1088/1475-7516/2020/07/020. URL: http://dx.doi.org/10.1088/1475-7516/2020/07/020.

[7] José Luis Bernal et al. "Signatures of primordial black holes as seeds of supermassive black holes". In: *Journal of Cosmology and Astroparticle Physics* 2018.05 (May 2018), 017–017. ISSN: 1475-7516. DOI: 10.1088/1475-7516/2018/05/017. URL: http://dx.doi.org/10.1088/1475-7516/2018/05/017.

[8] Robert J. Nemiroff and Bijunath Patla. "Adventures in Friedmann cosmology: A detailed expansion of the cosmological Friedmann equations". In: *American Journal of Physics* 76.3 (Mar. 2008), 265–276. ISSN: 1943-2909. DOI: 10.1119/1.2830536. URL: http://dx.doi.org/10.1119/1.2830536.

[9] Ya. B. Zel'dovich and I. D. Novikov. "The Hypothesis of Cores Retarded during Expansion and the Hot Cosmological Model". In: *Soviet Astronomy* 10 (Feb. 1967), p. 602.

[10] Stephen Hawking. "Gravitationally Collapsed Objects of Very Low Mass". In: *Monthly Notices of the Royal Astronomical Society* 152.1 (Apr. 1971), pp. 75–78. ISSN: 0035-8711. DOI: 10.1093/mnras/152.1.75. eprint: https://academic.oup.com/mnras/article-pdf/152/1/75/9360899/mnras152-0075.pdf. URL: https://doi.org/10.1093/mnras/152.1.75.

[11] B. P. Abbott et al. "Observation of Gravitational Waves from a Binary Black Hole Merger". In: *Phys. Rev. Lett.* 116 (6 2016), p. 061102. DOI: 10.1103/PhysRevLett.116.061102. URL: https://link.aps.org/doi/10.1103/PhysRevLett.116.061102.

[12] Simeon Bird et al. "Did LIGO Detect Dark Matter?" In: *Physical Review Letters* 116.20 (May 2016). ISSN: 1079-7114. DOI: 10.1103/physrevlett.116.201301. URL: http://dx.doi.org/10.1103/PhysRevLett.116.201301.

[13] Anne M Green and Bradley J Kavanagh. "Primordial black holes as a dark matter candidate". In: *Journal of Physics G: Nuclear and Particle Physics* 48.4 (Feb. 2021), p. 043001. ISSN: 1361-6471. DOI: 10.1088/1361-6471/abc534. URL: http://dx.doi.org/10.1088/1361-6471/abc534.

[14] Misao Sasaki et al. "Primordial black holes—perspectives in gravitational wave astronomy". In: *Classical and Quantum Gravity* 35.6 (Feb. 2018), p. 063001. ISSN: 1361-6382. DOI: 10.1088/1361-6382/aaa7b4. URL: http://dx.doi.org/10.1088/1361-6382/aaa7b4.

[15] Eleonora Di Valentino et al. "In the realm of the Hubble tension—a review of solutions *". In: *Classical and Quantum Gravity* 38.15 (July 2021), p. 153001. ISSN: 1361-6382. DOI: 10.1088/1361-6382/ac086d. URL: http://dx.doi.org/10.1088/1361-6382/ac086d.

[16] Antonio Riotto. "Inflation and the theory of cosmological perturbations". In: *ICTP Lect. Notes Ser.* 14 (2003). Ed. by G. Dvali et al., pp. 317–413. arXiv: hep-ph/0210162.

[17] Matias Zaldarriaga, Steven R. Furlanetto, and Lars Hernquist. "21 Centimeter Fluctuations from Cosmic Gas at High Redshifts". In: *The Astrophysical Journal* 608.2 (June 2004), 622–635. ISSN: 1538-4357. DOI: 10.1086/386327. URL: http://dx.doi.org/10.1086/386327.

[18] Daniel Baumann. *TASI Lectures on Inflation*. 2012. arXiv: 0907.5424 [hep-th].

[19] Ewan D. Stewart and David H. Lyth. "A more accurate analytic calculation of the spectrum of cosmological perturbations produced during inflation". In: *Physics Letters B* 302.2-3 (Mar. 1993), 171–175. ISSN: 0370-2693. DOI: 10.1016/0370-2693(93)90379-v. URL: http://dx.doi.org/10.1016/0370-2693(93)90379-V.

[20] Kazunori Kohri et al. "Precise measurements of primordial power spectrum with 21 cm fluctuations". In: *Journal of Cosmology and Astroparticle Physics* 2013.10 (Oct. 2013), 065–065. ISSN: 1475-7516. DOI: 10.1088/1475-7516/2013/10/065. URL: http://dx.doi.org/10.1088/1475-7516/2013/10/065.

[21] Julian B. Muñoz et al. "Towards a measurement of the spectral runnings". In: *Journal of Cosmology and Astroparticle Physics* 2017.05 (May 2017), 032–032. ISSN: 1475-7516. DOI: 10.1088/1475-7516/2017/05/032. URL: http://dx.doi.org/10.1088/1475-7516/2017/05/032.

[22] Jaume Garriga and Maria Sakellariadou. "Effects of friction on cosmic strings". In: *Physical Review D* 48.6 (Sept. 1993), 2502–2515. ISSN: 0556-2821. DOI: 10.1103/physrevd.48.2502. URL: http://dx.doi.org/10.1103/PhysRevD.48.2502.

[23] S.W. Hawking. "Black holes from cosmic strings". In: *Physics Letters B* 231.3 (1989), pp. 237–239. ISSN: 0370-2693. DOI: https://doi.org/10.1016/0370-2693(89)90206-2. URL: https://www.sciencedirect.com/science/article/pii/0370269389902062.

[24] R. R. Caldwell, H. A. Chamblin, and G. W. Gibbons. "Pair creation of black holes by domain walls". In: *Physical Review D* 53.12 (June 1996), 7103–7114. ISSN: 1089-4918. DOI: 10.1103/physrevd.53.7103. URL: http://dx.doi.org/10.1103/PhysRevD.53.7103.

[25] Bernard Carr and Florian Kuhnel. *Primordial Black Holes as Dark Matter Candidates*. 2021. arXiv: 2110.02821 [astro-ph.CO].

[26] Torsten Bringmann, Pat Scott, and Yashar Akrami. "Improved constraints on the primordial power spectrum at small scales from ultracompact minihalos". In: *Physical Review D* 85.12 (June 2012). ISSN: 1550-2368. DOI: 10.1103/physrevd.85.125027. URL: http://dx.doi.org/10.1103/PhysRevD.85.125027.

[27] Alba Kalaja et al. "From primordial black holes abundance to primordial curvature power spectrum (and back)". In: *Journal of Cosmology and Astroparticle Physics* 2019.10 (Oct. 2019), 031–031. ISSN: 1475-7516. DOI: 10.1088/1475-7516/2019/10/031. URL: http://dx.doi.org/10.1088/1475-7516/2019/10/031.

[28] J. M. Bardeen et al. "The Statistics of Peaks of Gaussian Random Fields". In: *Astrophysical Journal* 304 (May 1986), p. 15. DOI: 10.1086/164143.

[29] B. J. Carr. "The primordial black hole mass spectrum." In: *Astrophysical Journal* 201 (Oct. 1975), pp. 1–19. DOI: 10.1086/153853.

[30] Anne M. Green and Andrew R. Liddle. "Critical collapse and the primordial black hole initial mass function". In: *Physical Review D* 60.6 (Aug. 1999). ISSN: 1089-4918. DOI: 10.1103/physrevd.60.063509. URL: http://dx.doi.org/10.1103/PhysRevD.60.063509.

[31] J. C. Niemeyer and K. Jedamzik. "Near-Critical Gravitational Collapse and the Initial Mass Function of Primordial Black Holes". In: *Physical Review Letters* 80.25 (June 1998),

5481–5484. ISSN: 1079-7114. DOI: 10.1103/physrevlett.80.5481. URL: http://dx.doi.org/10.1103/PhysRevLett.80.5481.

[32] Ilia Musco, John C Miller, and Alexander G Polnarev. "Primordial black hole formation in the radiative era: investigation of the critical nature of the collapse". In: *Classical and Quantum Gravity* 26.23 (Oct. 2009), p. 235001. ISSN: 1361-6382. DOI: 10.1088/0264-9381/26/23/235001. URL: http://dx.doi.org/10.1088/0264-9381/26/23/235001.

[33] B. J. Carr et al. "New cosmological constraints on primordial black holes". In: *Physical Review D* 81.10 (May 2010). ISSN: 1550-2368. DOI: 10.1103/physrevd.81.104019. URL: http://dx.doi.org/10.1103/PhysRevD.81.104019.

[34] Gabriela Sato-Polito, Ely D. Kovetz, and Marc Kamionkowski. "Constraints on the primordial curvature power spectrum from primordial black holes". In: *Physical Review D* 100.6 (Sept. 2019). ISSN: 2470-0029. DOI: 10.1103/physrevd.100.063521. URL: http://dx.doi.org/10.1103/PhysRevD.100.063521.

[35] Riccardo Murgia et al. "Lyman-α Forest Constraints on Primordial Black Holes as Dark Matter". In: *Physical Review Letters* 123.7 (Aug. 2019). ISSN: 1079-7114. DOI: 10.1103/physrevlett.123.071102. URL: http://dx.doi.org/10.1103/PhysRevLett.123.071102.

[36] Alvise Raccanelli et al. "Determining the progenitors of merging black-hole binaries". In: *Physical Review D* 94.2 (July 2016). ISSN: 2470-0029. DOI: 10.1103/physrevd.94.023516. URL: http://dx.doi.org/10.1103/PhysRevD.94.023516.

[37] Giulio Scelfo et al. "GW×LSS: chasing the progenitors of merging binary black holes". In: *Journal of Cosmology and Astroparticle Physics* 2018.09 (Sept. 2018), 039–039. ISSN: 1475-7516. DOI: 10.1088/1475-7516/2018/09/039. URL: http://dx.doi.org/10.1088/1475-7516/2018/09/039.

[38] Giulio Scelfo et al. *Gravitational waves × HI intensity mapping: cosmological and astrophysical applications*. 2021. arXiv: 2106.09786 [astro-ph.CO].

[39] Ilias Cholis et al. "Orbital eccentricities in primordial black hole binaries". In: *Physical Review D* 94.8 (Oct. 2016). ISSN: 2470-0029. DOI: 10.1103/physrevd.94.084013. URL: http://dx.doi.org/10.1103/PhysRevD.94.084013.

[40] Ely D. Kovetz. "Probing Primordial Black Hole Dark Matter with Gravitational Waves". In: *Physical Review Letters* 119.13 (Sept. 2017). ISSN: 1079-7114. DOI: 10.1103/physrevlett.119.131301. URL: http://dx.doi.org/10.1103/PhysRevLett.119.131301.

[41] Nicola Bellomo et al. "Primordial black holes as dark matter: converting constraints from monochromatic to extended mass distributions". In: *Journal of Cosmology and Astroparticle Physics* 2018.01 (Jan. 2018), 004–004. ISSN: 1475-7516. DOI: 10.1088/1475-7516/2018/01/004. URL: http://dx.doi.org/10.1088/1475-7516/2018/01/004.

[42] Jonathan R Pritchard and Abraham Loeb. "21 cm cosmology in the 21st century". In: *Reports on Progress in Physics* 75.8 (July 2012), p. 086901. ISSN: 1361-6633. DOI: 10.1088/0034-4885/75/8/086901. URL: http://dx.doi.org/10.1088/0034-4885/75/8/086901.

[43] Jonathan R. Pritchard and Abraham Loeb. "Evolution of the 21 cm signal throughout cosmic history". In: *Physical Review D* 78.10 (Nov. 2008). ISSN: 1550-2368. DOI: 10.1103/physrevd.78.103511. URL: http://dx.doi.org/10.1103/PhysRevD.78.103511.

[44] S. A. Wouthuysen. "On the excitation mechanism of the 21-cm (radio-frequency) interstellar hydrogen emission line." In: *Astronomical Journal* 57 (Jan. 1952), pp. 31–32. DOI: 10.1086/106661.

[45] George B. Field. "The Spin Temperature of Intergalactic Neutral Hydrogen." In: *Astrophysical Journal* 129 (May 1959), p. 536. DOI: 10.1086/146653.

[46] Steven G. Murray et al. "21cmFAST v3: A Python-integrated C code for generating 3D realizations of the cosmic 21cm signal." In: *Journal of Open Source Software* 5.54 (2020), p. 2582. DOI: 10.21105/joss.02582. URL: https://doi.org/10.21105/joss.02582.

[47] Andrei Mesinger, Steven Furlanetto, and Renyue Cen. "21cmfast: a fast, seminumerical simulation of the high-redshift 21-cm signal". In: *Monthly Notices of the Royal Astronomical Society* 411.2 (Feb. 2011), pp. 955–972. ISSN: 0035-8711. DOI: 10.1111/j.1365-

2966.2010.17731.x. eprint: https://academic.oup.com/mnras/article-pdf/411/2/955/4099991/mnras0411-0955.pdf. URL: https://doi.org/10.1111/j.1365-2966.2010.17731.x.

[48] George B. Field. "An Attempt to Observe Neutral Hydrogen Between the Galaxies." In: *Astrophysical Journal* 129 (May 1959), p. 525. DOI: 10.1086/146652.

[49] Yacine Ali-Haïmoud, P. Daniel Meerburg, and Sihan Yuan. "New light on 21 cm intensity fluctuations from the dark ages". In: *Physical Review D* 89.8 (Apr. 2014). ISSN: 1550-2368. DOI: 10.1103/physrevd.89.083506. URL: http://dx.doi.org/10.1103/PhysRevD.89.083506.

[50] Steven R. Furlanetto, S. Peng Oh, and Frank H. Briggs. "Cosmology at low frequencies: The 21cm transition and the high-redshift Universe". In: *Physics Reports* 433.4-6 (Oct. 2006), 181–301. ISSN: 0370-1573. DOI: 10.1016/j.physrep.2006.08.002. URL: http://dx.doi.org/10.1016/j.physrep.2006.08.002.

[51] V. V. Sobolev. "The Diffusion of Lα Radiation in Nebulae and Stellar Envelopes." In: *Soviet Astronomy* 1 (Oct. 1957), p. 678.

[52] Yi Mao et al. "Redshift-space distortion of the 21-cm background from the epoch of reionization - I. Methodology re-examined". In: *Monthly Notices of the Royal Astronomical Society* 422.2 (Apr. 2012), 926–954. ISSN: 0035-8711. DOI: 10.1111/j.1365-2966.2012.20471.x. URL: http://dx.doi.org/10.1111/j.1365-2966.2012.20471.x.

[53] Judd D. Bowman et al. "An absorption profile centred at 78 megahertz in the sky-averaged spectrum". In: *Nature* 555.7694 (Mar. 2018), 67–70. ISSN: 1476-4687. DOI: 10.1038/nature25792. URL: http://dx.doi.org/10.1038/nature25792.

[54] Antony Lewis and Anthony Challinor. "21 cm angular-power spectrum from the dark ages". In: *Physical Review D* 76.8 (Oct. 2007). ISSN: 1550-2368. DOI: 10.1103/physrevd.76.083005. URL: http://dx.doi.org/10.1103/PhysRevD.76.083005.

[55] Michael Kuhlen, Piero Madau, and Ryan Montgomery. "The Spin Temperature and 21 cm Brightness of the Intergalactic Medium in the Pre-Reionization era". In: *The Astrophysical Journal* 637.1 (Jan. 2006), L1–L4. ISSN: 1538-4357. DOI: 10.1086/500548. URL: http://dx.doi.org/10.1086/500548.

[56] Yacine Ali-Haïmoud and Christopher M. Hirata. "Ultrafast effective multilevel atom method for primordial hydrogen recombination". In: *Physical Review D* 82.6 (Sept. 2010). ISSN: 1550-2368. DOI: 10.1103/physrevd.82.063521. URL: http://dx.doi.org/10.1103/PhysRevD.82.063521.

[57] Yacine Ali-Haïmoud and Christopher M. Hirata. "HyRec: A fast and highly accurate primordial hydrogen and helium recombination code". In: *Physical Review D* 83.4 (Feb. 2011). ISSN: 1550-2368. DOI: 10.1103/physrevd.83.043513. URL: http://dx.doi.org/10.1103/PhysRevD.83.043513.

[58] Somnath Bharadwaj and Sk. Saiyad Ali. "The cosmic microwave background radiation fluctuations from HI perturbations prior to reionization". In: *Monthly Notices of the Royal Astronomical Society* 352.1 (July 2004), 142–146. ISSN: 1365-2966. DOI: 10.1111/j.1365-2966.2004.07907.x. URL: http://dx.doi.org/10.1111/j.1365-2966.2004.07907.x.

[59] Emmanuel Schaan and Martin White. "Multi-tracer intensity mapping: cross-correlations, line noise & decorrelation". In: *Journal of Cosmology and Astroparticle Physics* 2021.05 (May 2021), p. 068. ISSN: 1475-7516. DOI: 10.1088/1475-7516/2021/05/068. URL: http://dx.doi.org/10.1088/1475-7516/2021/05/068.

[60] Alle-Jan Veen and Stefan Wijnholds. "Signal Processing Tools for Radio Astronomy". In: May 2013, pp. 421–463. ISBN: 978-1-4614-6858-5. DOI: 10.1007/978-1-4614-6859-2_14.

[61] Max Tegmark and Matias Zaldarriaga. "Fast Fourier transform telescope". In: *Physical Review D* 79.8 (Apr. 2009). ISSN: 1550-2368. DOI: 10.1103/physrevd.79.083530. URL: http://dx.doi.org/10.1103/PhysRevD.79.083530.

[62] M. Ryle and A. Hewish. "The Synthesis of Large Radio Telescopes". In: *Monthly Notices of the Royal Astronomical Society* 120.3 (Mar. 1960), pp. 220–230. ISSN: 0035-8711. DOI: 10.1093/mnras/120.3.220. eprint: https://academic.oup.com/mnras/article-

pdf/120/3/220/8074735/mnras120-0220.pdf. URL: https://doi.org/10.1093/mnras/120.3.220.

[63] G. Bernardi. *21 cm observations: calibration, strategies, observables*. 2019. arXiv: 1909.11938 [astro-ph.IM].

[64] Adrian Liu and J. Richard Shaw. "Data Analysis for Precision 21 cm Cosmology". In: *Publications of the Astronomical Society of the Pacific* 132.1012 (Apr. 2020), p. 062001. ISSN: 1538-3873. DOI: 10.1088/1538-3873/ab5bfd. URL: http://dx.doi.org/10.1088/1538-3873/ab5bfd.

[65] David R. DeBoer et al. "Hydrogen Epoch of Reionization Array (HERA)". In: *Publications of the Astronomical Society of the Pacific* 129.974 (Mar. 2017), p. 045001. ISSN: 1538-3873. DOI: 10.1088/1538-3873/129/974/045001. URL: http://dx.doi.org/10.1088/1538-3873/129/974/045001.

[66] Aaron Parsons et al. "A SENSITIVITY AND ARRAY-CONFIGURATION STUDY FOR MEASURING THE POWER SPECTRUM OF 21 cm EMISSION FROM REIONIZATION". In: *The Astrophysical Journal* 753.1 (June 2012), p. 81. ISSN: 1538-4357. DOI: 10.1088/0004-637x/753/1/81. URL: http://dx.doi.org/10.1088/0004-637X/753/1/81.

[67] K. Rohlfs and T. L. Wilson. *Tools of radio astronomy*. 2000.

[68] Max Tegmark, Andy N. Taylor, and Alan F. Heavens. "Karhunen-Loeve Eigenvalue Problems in Cosmology: How Should We Tackle Large Data Sets?" In: *The Astrophysical Journal* 480.1 (May 1997), 22–35. ISSN: 1538-4357. DOI: 10.1086/303939. URL: http://dx.doi.org/10.1086/303939.

[69] R. A. Fisher. "The Logic of Inductive Inference". In: *Journal of the Royal Statistical Society* 98.1 (1935), pp. 39–82. ISSN: 09528385. URL: http://www.jstor.org/stable/2342435.

[70] L. Verde. "Statistical Methods in Cosmology". In: *Lecture Notes in Physics* (2010), 147–177. ISSN: 1616-6361. DOI: 10.1007/978-3-642-10598-2_4. URL: http://dx.doi.org/10.1007/978-3-642-10598-2_4.

[71] Diego Blas, Julien Lesgourgues, and Thomas Tram. "The Cosmic Linear Anisotropy Solving System (CLASS). Part II: Approximation schemes". In: *Journal of Cosmology and Astroparticle Physics* 2011.07 (July 2011), 034–034. ISSN: 1475-7516. DOI: 10.1088/1475-7516/2011/07/034. URL: http://dx.doi.org/10.1088/1475-7516/2011/07/034.

[72] Marilena LoVerde and Niayesh Afshordi. "Extended Limber approximation". In: *Physical Review D* 78.12 (Dec. 2008). ISSN: 1550-2368. DOI: 10.1103/physrevd.78.123506. URL: http://dx.doi.org/10.1103/PhysRevD.78.123506.

[73] Dan Coe. *Fisher Matrices and Confidence Ellipses: A Quick-Start Guide and Software*. 2009. arXiv: 0906.4123 [astro-ph.IM].

[74] Christian T. Byrnes, Philippa S. Cole, and Subodh P. Patil. "Steepest growth of the power spectrum and primordial black holes". In: *Journal of Cosmology and Astroparticle Physics* 2019.06 (June 2019), 028–028. ISSN: 1475-7516. DOI: 10.1088/1475-7516/2019/06/028. URL: http://dx.doi.org/10.1088/1475-7516/2019/06/028.

[75] Y. Akrami et al. "Planck2018 results". In: *Astronomy & Astrophysics* 641 (Sept. 2020), A10. ISSN: 1432-0746. DOI: 10.1051/0004-6361/201833887. URL: http://dx.doi.org/10.1051/0004-6361/201833887.

Acknowledgements

I would like to thanks everyone who supported me in the endeavour that led to complete this thesis. I would like to thank my supervisor, Prof. Alvise Raccanelli, and my co-supervisor, Prof. Sabino Matarrese. I would like to thank Alvise in particular for the encouragement and advice given while I was working on this thesis, as well as for helping me finding future PhD openings and being available for writing me reference letters.

I would also like to thank my parents and my relatives for being loving, supportive and patient and for taking interest in my work.

Last but not least I would like to thank all my friends for always making me feel welcome. A big thank you in particular to Anna, Filippo and Rio for always bringing a smile to my face, even in the most stressful moments.